UNIVERSITY OF NAPLES FEDERICO II

Polytechnic and Basic Sciences School

Ph. D. School in Chemical Sciences

CHEMICAL BIOLOGY APPROACCHES TO DISCLOSE TREM2 FUNCTIONS

Mario Dell'Isola

Supervisor

Prof. Marina Della Greca

Co-supervisor

Dott. Carmela Gallo

Examiner

Prof. Maria Monti

XXXVIII cycle

Coordinator: Prof. Alessandra Napolitano

To Mom, Dad, and Dolly,

And to Grandma, who's watching from above…

Chapter 3

Chapter 4

Section III: Materials and methods

Chapter 5

Abstract

Currently, TREM2 is recognized as one of the most promising therapeutic targets for neurodegenerative diseases. Nevertheless, substantial gaps persist in elucidating its mechanism of action, largely due to the limited identification and characterization of its putative agonists, hence its classification as an "orphan receptor." The main goal of this PhD project is to develop innovative tools to advance the mechanistic understanding of TREM2 through the identification of novel endogenous ligands. Building upon prior evidence from the synthetic sulfolipid Sulfavant A (SULF A), the first synthetic reported TREM2 ligand, a search for structurally related endogenous molecules had been conducted in the brains of young mice, where TREM2 is predominantly expressed by microglial cells (brain resident macrophage-like cells). Comprehensive mass spectrometry analyses, supported by MZmine-assisted deconvolution of raw LC-MS/MS data, enabled the identification of three sulfated lipid classes, including sulfatides, seminolipids, and SGDG. Functional assays, including TREM2-reporter and phagocytosis tests, pointed out the seminolipids as candidate TREM2 ligand, eliciting cellular responses comparable to SULF-A. This project investigated also the development of biochemical tools to elucidate the TREM2 signalling. In this context, the inhibitory peptide IA9 was examined as a biochemical probe and experimental findings revealed that its biological activity is strongly influenced by the nature of the associated counterion, which modulates its structural conformation and functional properties. Taken together, this work represents a pioneering effort to unravel the molecular mechanisms governing TREM2 activation and signalling. It establishes a conceptual and methodological framework for future studies aimed at exploring TREM2-mediated pathways and therapeutic strategies. Seminolipids emerge as valuable molecular tools for dissecting TREM2 function and its role in neuroinflammatory contexts, both *in vitro* and *in vivo*. Conversely, the IA9-K peptide will require further refinement to define the optimal conditions for its application as a selective TREM2 inhibitor in functional studies.

Riassunto

Attualmente, TREM2 è riconosciuto come uno dei bersagli terapeutici più promettenti per le malattie neurodegenerative. Tuttavia, permangono notevoli lacune nella comprensione del suo preciso meccanismo d'azione, dovute principalmente alla limitata identificazione e caratterizzazione dei suoi potenziali agonisti, motivo per cui è classificato come "recettore orfano". L'obiettivo principale di questo progetto di dottorato è stato lo sviluppo di strumenti innovativi per approfondire la comprensione dei meccanismi molecolari alla base dell'attivazione di TREM2, attraverso l'identificazione di nuovi ligandi endogeni. Partendo dalle evidenze precedenti sul sulfolipide sintetico Sulfavant A (SULF A), il primo ligando sintetico di TREM2 riportato in letteratura, è stata avviata una ricerca di molecole endogene strutturalmente affini nei cervelli di topi giovani, in cui TREM2 è espresso prevalentemente dalle cellule microgliali (macrofagi residenti del cervello). Analisi di spettrometria di massa ad alta risoluzione, supportate dalla deconvoluzione dei dati grezzi di LC–MS/MS tramite il software MZmine, hanno permesso l'identificazione di tre classi di lipidi solfatati: sulfatidi, seminolipidi e SGDG. I saggi funzionali, inclusi test su cellule reporter per TREM2 e saggi di fagocitosi, hanno dimostrato che i seminolipidi inducono risposte cellulari paragonabili a quelle osservate con SULF-A, posizionandoli così come candidati credibili per l'interazione con TREM2. Il progetto ha inoltre esplorato lo sviluppo di strumenti biochimici per studiare il signaling mediato da TREM2. In questo contesto, il peptide inibitore IA9 è stato analizzato come sonda biochimica, e i risultati sperimentali hanno evidenziato che la sua attività biologica è fortemente influenzata dalla natura del controione associato, che ne modula la conformazione strutturale e le proprietà funzionali. Complessivamente, questo lavoro rappresenta un approccio pionieristico nello studio dei meccanismi molecolari che regolano l'attivazione e la segnalazione di TREM2. Esso fornisce un quadro concettuale e metodologico per futuri studi volti ad approfondire i percorsi di segnalazione mediati da TREM2 e le relative strategie terapeutiche. I seminolipidi emergono come strumenti molecolari di grande valore per lo studio della funzione di TREM2 e del suo ruolo nei contesti neuroinfiammatori, sia *in vitro* che *in vivo*. Al contrario, il peptide IA9-K richiederà ulteriori ottimizzazioni per definire le condizioni ideali per il suo impiego come inibitore selettivo di TREM2 negli studi meccanicistici e funzionali.

Section I: Introduction

Chapter 1

Biochemical and biological relevance of TREM2

1.1 Biochemical properties of TREM2

The Triggering Receptor Expressed on Myeloid cells 2 (TREM2) is a cell-surface receptor broadly expressed in the myeloid compartment, including macrophages, dendritic cells and osteoclasts where it modulates immune signalling and metabolic fitness [1]. In the central nervous system, TREM2 is highly expressed in microglia, the resident immune cells of the brain, and governs transcriptional and functional programs essential for neural homeostasis [2]. By coordinating phagocytosis, lipid processing, and inflammatory responses, TREM2 enables microglia to clear cellular debris, limit detrimental inflammation, and support tissue regeneration [3]. Impaired TREM2 signalling disrupts these adaptive mechanisms, which leads to persistent neuroinflammation and progressive neuronal damage [4]. TREM2 is a 230-amino-acid type-I transmembrane receptor characterized by an extracellular V-type immunoglobulin–like domain, a short connecting stalk, a single transmembrane helix, and a compact cytoplasmic tail [5] (**Figure 1A**). The protein carries two conserved N-linked glycosylation sites, N20 and N79, whose modification is essential for proper folding, stability, and delivery to the cell surface. Notably, glycosylation at N79 is critical for efficient plasma-membrane trafficking, and both sites contribute to robust signalling capacity [6] . Mutations in TREM2, including R47H and T66M, have been associated with Alzheimer's disease and related neurodegenerative disorders, highlighting its critical role in maintaining brain immune homeostasis [7]. The extracellular Ig-like domain detects molecular signals, while the stalk provides flexibility, linking the Ig-like domain to the TM helix [8]. The TM helix mediates association with the adaptor protein DAP12 (TYROBP), which contains an immunoreceptor tyrosine-based activation motif (ITAM) (**Figure 1B**) [9]. DAP12 forms homodimers through disulfide bonds between cysteine residues in its extracellular domain, which is essential for its adaptor function in immune signalling [10]. TM-DAP12 interaction initiates intracellular signalling cascades, enabling microglia to sense and respond to changes in their extracellular environment [11]. The TREM2 TM domain undergoes proteolytic cleavage by ADAM-family metalloproteases, including

ADAM10 and ADAM17, at a site within the stalk region, generating the soluble fragment sTREM2. This shedding is tightly regulated and influences TREM2-mediated signalling and microglial activity [12]. Variants near the cleavage site, such as H157Y, modify sTREM2 levels, potentially altering receptor function and downstream cellular responses [13].

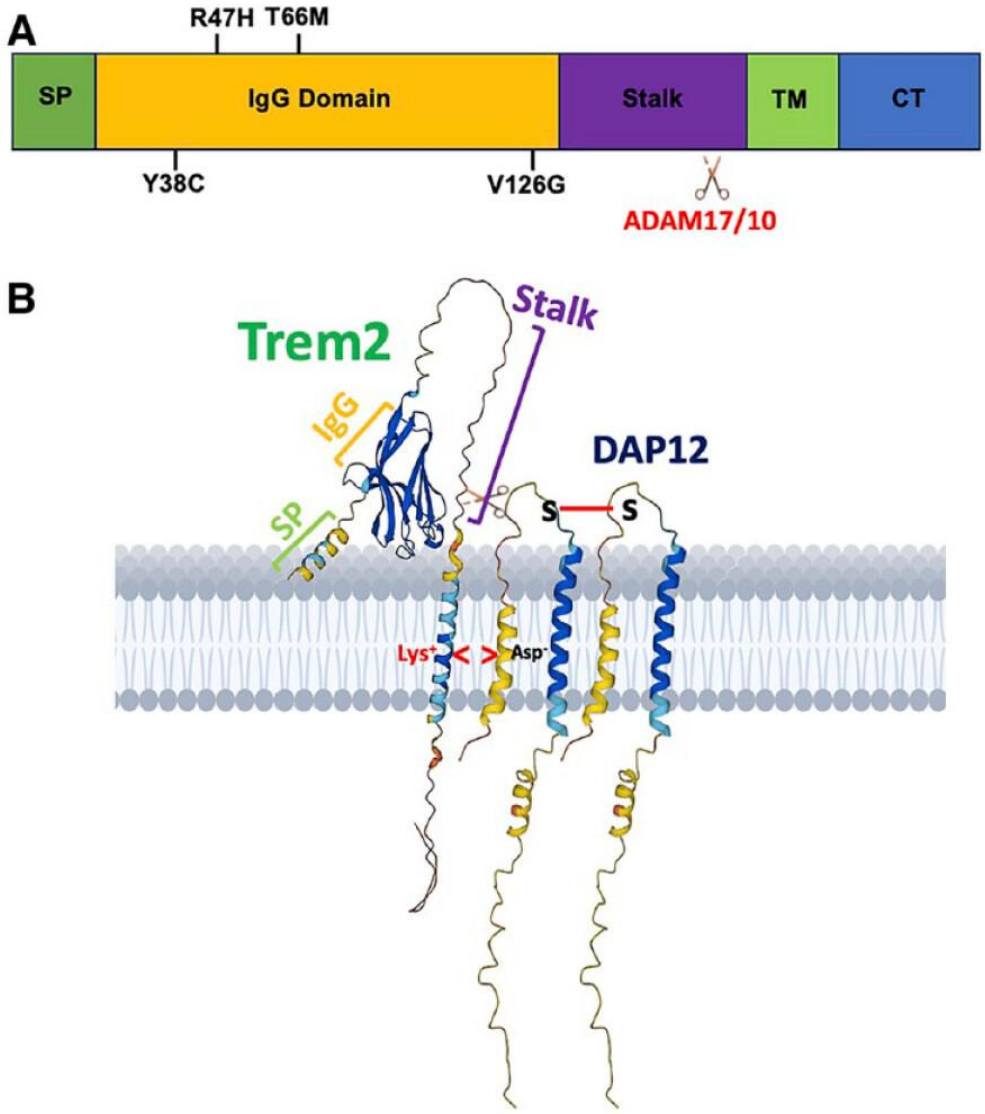

Figure 1 - Domain structure of TREM2 and relevance to Alzheimer's disease. (A) Schematic representation of human TREM2, showing the signal peptide (SP), transmembrane domain (TM), and C-terminal tail (CT), with key AD-associated variants and the cleavage sites for ADAM10/17 indicated. (B) 3D structure of the membrane-anchored TREM2-DAP12 complex (AlphaFold IDs: Q9NZC2, O43914), highlighting the transmembrane anchoring of TREM2, its interactions with DAP12, and the disulfide-mediated dimerization of DAP12, which contributes to the structural stability and signalling function of the complex**.** (Qian Shi et al., 2024)

The extracellular domain (ECD) of TREM2 consists of a single Ig-like fold, which is essential for ligand recognition. Structurally, this domain adopts a β-sandwich architecture characteristic of the Ig superfamily and harbours two functionally distinct ligand-binding regions [14]. The first, a hydrophobic site located within the complementarity-determining regions (CDRs) of the Ig domain, engages lipid-associated molecules such as apolipoprotein E (ApoE) and amyloid-β (Aβ) peptides [3]. Site-directed mutagenesis (**Figure 2**) shows that substitutions at key residues, including W44, L69, and L71, significantly diminish ligand binding, highlighting the critical role of this hydrophobic pocket. These residues stabilize interactions with lipid-rich ligands and contribute to ligand specificity. Disruption of this pocket impairs downstream signalling, including microglial activation and phagocytosis, and provides a potential explanation for the effects of disease-associated variants [15]. The second site is an electropositive patch positioned near the midsection of the Ig domain, which mediates interactions with negatively charged ligands, including phosphatidylserine (PS) and heparan sulfate (HS). Specific sulfation patterns on HS, especially 6-O-sulfation, are essential for effective recognition, emphasizing the importance of electrostatic complementarity in determining ligand specificity [16].

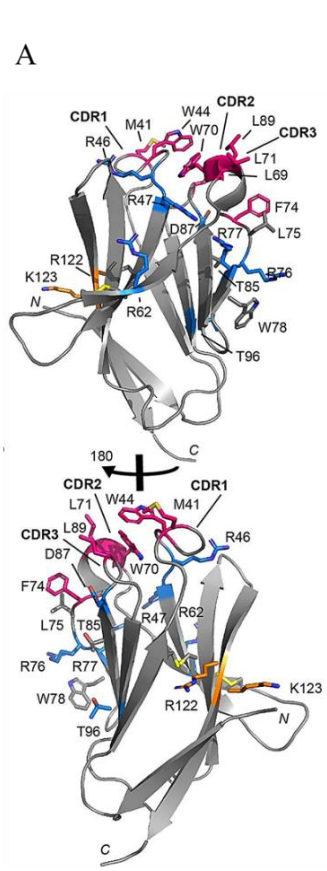

B

TREM2 variant	site
M41D	hydrophobic
W44D	hydrophobic
L69D	hydrophobic
W70D	hydrophobic
L71D	hydrophobic
F74D	hydrophobic
L89D	hydrophobic
L69D/L71D	hydrophobic
W44D/L69D/L71D	hydrophobic
R47H	basic
R62H	basic
D87N	basic
T96K	basic
R76D	basic
R77D	basic
R47H/R62H	basic
R46A	basic
R46D	basic
R46A/R47A	basic
R46D/R47D	basic
R47D/R62D	basic
L75D	basic adjacent
W78D	basic adjacent
T85D	basic adjacent
R122E	site 2
K123E	site 2
K123D	site 2
R122D/K123D	site 2

Figure 2 - TREM2 variants designed to probe ligand interactions. (A) Ribbon diagram showing mutated residues (red: hydrophobic; blue: basic; gray: adjacent to basic; orange: site 2). (B) Table listing all TREM2 variants generated. (Greven et al., 2025)

There is only one *in silico* study of the wild-type TREM2 ECD that reported the molecular basis for its interaction with one of the reported putative ligands, PS. In the TREM2-PS complex, the phosphate headgroups of PS interact with a positively charged patch on the Ig-like V-domain, involving residues such as Arg47, Arg62, His67, and Arg77, stabilizing the ligand-receptor interface. This interaction enables TREM2 to recognize PS-exposing membranes, such as those of apoptotic cells or synapses, and facilitates downstream signalling events, including microglial engagement and clearance of apoptotic material. In the structural model, the TREM2 ECD forms a trimer (**Figure 3**), which may enhance avidity for multivalent ligands such as PS-enriched membranes and provides a mechanistic basis for cooperative ligand recognition [17].

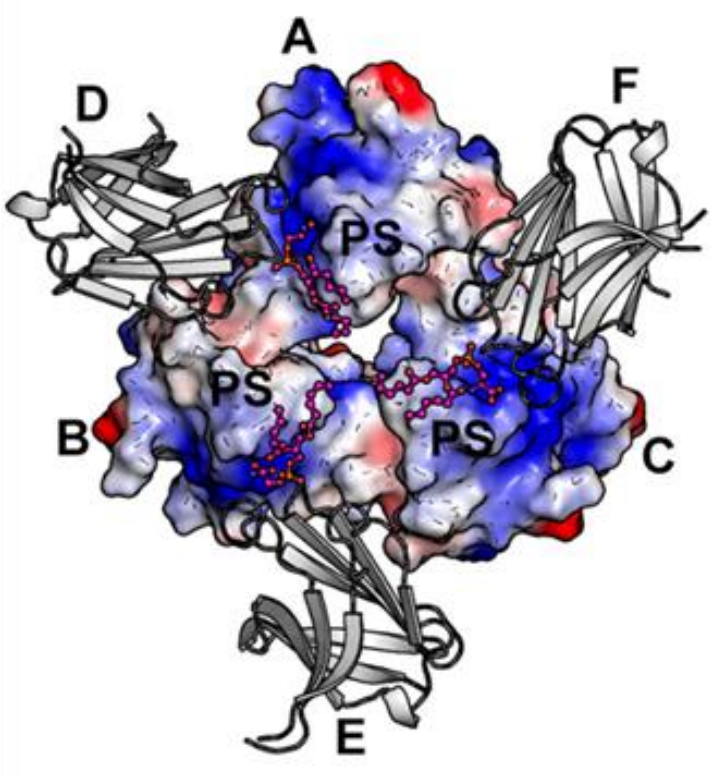

Figure 3 - PS-bound WT TREM2 model structure. This model depicts the electrostatic surface of the trimeric core, the surrounding TREM2 protomers that constitute the higher-order assembly (gray cartoon), and the bound PS molecule (fuchsia sticks) (Sudom et al., 2018).

Despite substantial progress in elucidating the structural and functional properties of TREM2, current understanding is constrained by the heavy reliance on in silico models, which cannot fully capture the receptor conformational flexibility or dynamic ligand interactions, and by the lack of a complete crystal structure of the full-length protein, limiting insight into how the extracellular domain communicates with the transmembrane and intracellular regions (18,17). Comprehensive characterization of endogenous ligands, including their affinities, binding kinetics, and potential competition *in vivo*,

remains incomplete, as most studies have focused on ApoE, Aβ, and PS (19,15). The functional consequences of these interactions, particularly in the context of Alzheimer's disease, are still poorly understood, and the impact of disease-associated variants, such as R47H and T66M, on ligand recognition and receptor function has not been fully elucidated [15]. Finally, the mechanisms by which ligand-induced conformational changes in the Ig domain propagate to intracellular signalling cascades, and how these modulate key microglial functions, remain largely unresolved (14,3).

The intracellular signalling is provided by the α-helix TM domain of TREM2, which directly associates with the adaptor protein DAP12, whose cytoplasmic tail contains an ITAM motif. [20]. In a recent proposed model TREM2 binds the DAP12 dimer mainly through a salt bridge between K26 (TREM2) and D16 (DAP12), with additional stabilization from hydrophobic contacts and minor hydrogen bonds (e.g., K26/T20, W34/T20) (**Figure 4**). Simulations show that TREM2 undergoes a conformational change: the unbound "kinked" state interacts with one DAP12 chain, while the bound "unkinked" state allows stable interactions with both chains via K26–D16 hydrogen bonds and supporting hydrophobic contacts the correct alignment of the helices. These interactions are essential for linking extracellular ligand binding to intracellular signalling in microglia. [21]

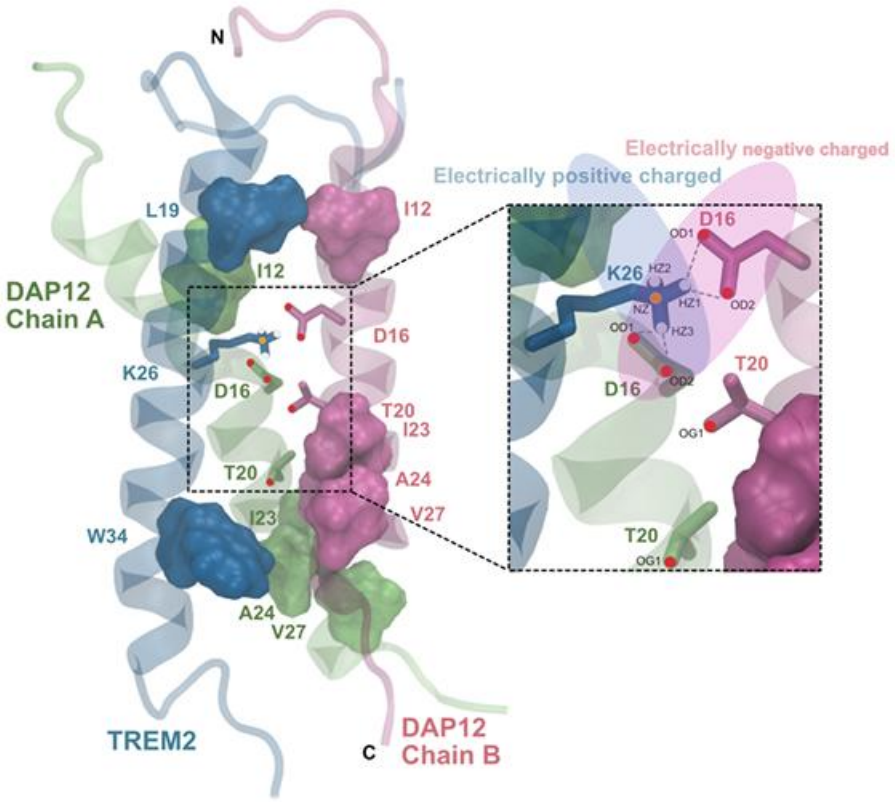

Figure 4 - Proposed TREM2/DAP12 binding mechanism. TREM2, DAP12 Chain A, and Chain B are shown in blue, lime, and mauve. The blue and red shaded regions highlight the K26 (TREM2) and D16 (DAP12) salt

bridge, with gray dashed lines indicating possible hydrogen bonds. Key hydrophobic pairs (L19/I12, W34/I23, W34/A24, W34/A27) are shown on the surface. (Zhong et al., 2024)

Recent studies have provided new insights into the structural dynamics of the TM. NMR spectroscopy and molecular dynamics simulations have revealed that the TM helix is predominantly α-helical but features a subtle kink near the conserved lysine residue K186. This kink is thought to influence the orientation of the helix within the lipid bilayer and to facilitate electrostatic interactions with the complementary aspartate residue in the DAP12 TM helix, stabilizing the receptor-adaptor complex. Such structural adaptations also confer increased flexibility to the TM domain, which is essential for proper signal transduction and overall receptor function (22,21).

However, models of the TREM2–DAP12 interface, including salt-bridge and hydrophobic interactions [21], rely largely on molecular dynamics simulations and in silico predictions, which cannot fully reflect conformational flexibility or membrane context.

1.2 TREM2 as a key modulator of microglial function in the brain

Multiple studies have consistently revealed that TREM2 expression is primarily restricted to microglial cells within the brain parenchyma, while it remains undetectable in neurons, astrocytes, and oligodendrocytes under physiological conditions (23,24). Growing evidence underscores its role in sustaining microglial homeostasis by regulating lipid handling, phagocytosis, and cellular responses to neuronal stress or injury (25,26). In the aging brain, and especially in regions undergoing neurodegenerative changes, TREM2 expression increases, supporting the role for this receptor in preserving neural integrity and homeostatic balance (27,28).

One of the most distinctive physiological roles of TREM2 lies in its capacity to orchestrate the transitions between microglial activation states. In the healthy brain, microglia maintain a ‘homeostatic’ phenotype, typified by an extensively ramified morphology, low basal production of pro-inflammatory mediators, and the expression of canonical homeostatic markers such as P2RY12, TMEM119, CX3CR1, SALL1, FCRLS, GPR34, and HEXB, many of which are regulated by TGF-β-dependent signalling [29], [30]. In this surveillance state, microglia exhibit remarkable motility, constantly patrolling the neural parenchyma to monitor synaptic integrity and to remove apoptotic material without eliciting overt immune activation. Upon neuronal injury or exposure to pathological cues, TREM2 signalling functions as a pivotal molecular switch that drives the reprogramming of microglia toward a “reactive” or “disease-associated” phenotype (DAM) (**Figure 5**). This transition entails a profound remodelling of the microglial transcriptome, characterized by the suppression of homeostatic gene networks and the induction of genes involved in lipid metabolism (APOE, LPL), phagocytosis (CD68, CST7), and

lysosomal function (CTSD, LAMP1) (2,31). Through these changes, TREM2 endows microglia with enhanced metabolic and degradative capacities, enabling them to clear cellular debris, aggregated proteins (Beta-amyloid, hyperphosphorylated tau, alpha-synuclein), and damaged myelin with greater efficiency. Conversely, loss-of-function mutations or deficiency of TREM2 critically impair this adaptive transition, leading to an accumulation of apoptotic bodies and lipid-rich waste products, ineffective containment of amyloid pathology, and a subsequent amplification of neuronal stress and degeneration (4,32). Thus, TREM2 signalling emerges as an indispensable determinant of microglial plasticity, ensuring a finely tuned balance between immune vigilance and neuroprotection.

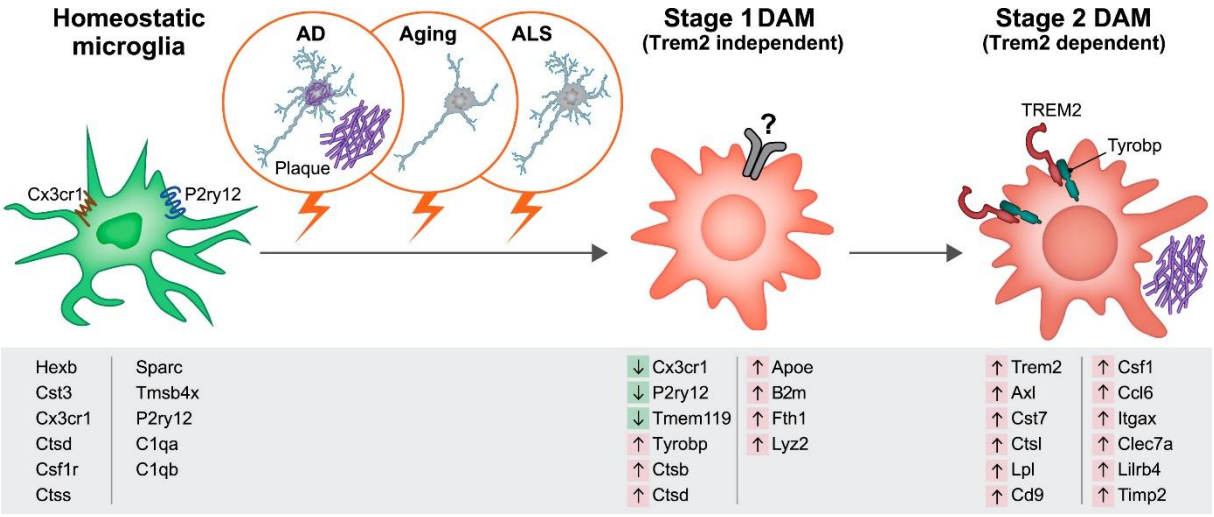

Figure 5 - Schematic representation of microglial transition from a homeostatic state to stage 1 (TREM2-independent) and stage 2 (TREM2-dependent) DAM phenotypes in different conditions such as aging, Alzheimer's disease, or ALS pathology. Key genes up- (red arrows) or down-regulated (green arrows) in each stage are indicated below. (Keren-Shau et al., 2017)

TREM2 serves as a central node in the regulation of microglial metabolic programs. It has been reported that activation of the TREM2–DAP12–SYK signalling cascade engages little known downstream effectors, such as the PI3K-AKT-mTOR and MAPK/ERK pathways, which collectively promote anabolic metabolism, enhance mitochondrial integrity, and reinforce microglial resilience under metabolic stress (4,33).Through this finely tuned regulatory network, TREM2 may enable microglia to meet the energetic demands associated with motility, phagocytic clearance, and the controlled secretion of cytokines and neurotrophic factors. In contrast, the loss or functional impairment of TREM2 is suggested to induce a shift toward a glycolytic phenotype [4] leading to TREM2-deficient microglia energetically compromised, exhibiting diminished phagocytic capacity and increased inflammatory reactivity. TREM2 serves also as a crucial regulator of microglia-neuron communication. A central

aspect of this neuroimmune interaction involves the TREM2-dependent recognition and phagocytosis of apoptotic neurons, degenerating synapses, and cellular debris (34,35). Through this continuous surveillance, microglia prevent the accumulation of damage-associated molecular patterns (DAMPs) and exacerbate inflammatory responses that compromise neuronal viability. In parallel, TREM2 signalling influences the microglial secretome, modulating the synthesis and release of neurotrophic mediators including insulin-like growth factor 1 and brain-derived neurotrophic factor [36]. Through these trophic interactions, TREM2 contribute to the maintenance and remodelling of neuronal networks during both development and adaptive repair.

1.3 TREM2 putative ligands: current knowledge and gaps in mechanistic understanding

TREM2 is classified as an "orphan" receptor, since no specific TREM2 ligands were reported and several aspects of TREM2 signalling, from the molecular receptor-ligand interaction to the intracellular transduction mechanisms, remain poorly understood [37]. TREM2 engagement covers a structurally diverse array of molecules, including phospholipids, lipoproteins, and misfolded or aggregated proteins [38]. Rather than binding a single, well-defined motif, TREM2 appears to act as a broad sensor of molecular patterns, detecting cues associated with lipid dysregulation, cellular stress, or tissue damage (39,40). This versatility likely underlies TREM2 capacity to orchestrate diverse processes. A recent review [41] summarized the current understanding of the structural motifs recognized by TREM2 (Table 1).

Table 1 - Summary of reported putative TREM2 ligands and their associated biological functions [41].

Ligands	Biological function	Reference
Dextran sulfate, LPS, and LTA	-	[42]
Lipoligosaccharides (LOS) from N. Gonococcusan	Interleukin-6 production in HeLa cervical carcinoma cells	[43]
unknown ligand in C. jejuni	-	[43]
Phosphatidylserine	Sustaining of the microglial response to Ab accumulation and regulation of microglial function by transducing intracellular signals on apoptotic cells	(44,39)
Phosphatidylethanolamine		
Cardiolipin		

Nucleic acids released by ischemic brain	Microglial activation to amoeboid phenotype and increase phagocytosis of injured neurons in brain ischemia	[45]
Escherichia coli	-	[46]
Apolipoprotein	Apolipoprotein Increase of phagocytosis in microglia	[47]
Beta amyloid forms	Activation of NFAT signaling and internalization of beta amyloid forms	[48]
Glycolipids and sulfoglycolipids	-	(49,50,51)
Non-glycosylated mycolic acid-containing lipids	-	(52,53)
Sphingosine-1-phosphate	-	[54]

Sulfated dextrans, lipopolysaccharide, and lipoteichoic acid have attracted attention as representative anionic macromolecules among the TREM2 putative ligands. TREM2 has been proposed to act as a sensor for negatively charged molecules, prompting in deepen biochemical investigations. Sulfated dextrans, synthetic polysaccharides densely decorated with sulfate groups, engage TREM2 primarily through electrostatic complementarity rather than sequence-specific recognition (42,27). Similarly, LPS from Gram-negative and LTA from Gram-positive bacteria associate with recombinant TREM2 constructs, consistent with charge- and surface-driven interactions rather than canonical receptor-ligand binding [55].

However, these studies rely on the use of recombinant TREM2-Fc proteins, huge amount of ligand, and multivalent plate- or bead-based assays, conditions that favour nonspecific electrostatic interactions and may overestimate physiological relevance (27,15).

In addition, TREM2 has emerged as a versatile receptor for charged membrane lipids, as PS and phosphatidylethanolamine (PE). Under physiological conditions, these phospholipids reside largely in the inner leaflet of the plasma membrane; upon apoptosis, neuronal injury, or cellular stress, they become exposed, enabling TREM2-expressing myeloid cells to recognize and clear cellular debris (39,19). In β-amyloid pathology, exposed PS on damaged neurons acts as a critical “eat-me” signal for microglia,

facilitating clearance and maintaining neural homeostasis [47]. Sulfatides, sulfated glycosphingolipids enriched in myelin and neuronal membranes, are also proposed TREM2 ligands. Their exposure increases during neurodegeneration, and *in vitro* studies indicate that TREM2 binding promotes microglial recognition and phagocytosis of sulfatide-rich debris [27]. Cardiolipin, a dimeric phospholipid of the inner mitochondrial membrane, has recently emerged as another candidate. When externalized on stressed or apoptotic cells, cardiolipin may recruit TREM2 to facilitate clearance of damaged mitochondria and neuronal fragments, though *in vivo* validation is still limited [56]. Evidence on the classification of PS, PE, sulfatides, and cardiolipin as bona fide TREM2 ligands remains elusive and derives largely from *in vitro* assays, where TREM2 exhibits high ligand promiscuity (27,39), and from computational docking predictions [56].

ApoE is one of the most studied putative ligands, binding TREM2 with measurable affinity. Different biological and computational studies suggested that TREM2 interacts with all major ApoE isoforms (E2, E3, and E4), facilitating the uptake of ApoE-containing lipoproteins in microglia and macrophages, thereby linking TREM2 to lipid metabolism and immune regulation [47]. Disease-associated variants of TREM2, such as R47H, reduce binding to ApoE, suggesting that this interaction may be critical for receptor-mediated lipid handling and microglial function [57].

The research group where I carried out my PhD project, recently characterized the synthetic sulfoglycolipid Sulfavant A (SULF A) as the first synthetic ligand of TREM-2 receptor [50]. In a TREM2 reporter system, SULF A effectively triggered receptor activation, exhibiting a markedly stronger activity than both phosphatidylserine and the anti-TREM2 antibody. Binding of SULF A promotes a “homeostatogenic” dendritic cell phenotype, characterized by upregulation of MHC class II and co-stimulatory molecules without triggering pro-inflammatory cytokine release, reflecting a controlled immunomodulatory profile [50]. Engagement of TREM2 by SULF A drives dendritic cell maturation and promotes naïve T cell proliferation and differentiation of regulatory T cell subsets, by proving the potential of this molecule as a controlled immunomodulatory agent for therapeutic applications [51]. In a very recent study [58], treatment of primary murine microglia with SULF A fine-tunes microglial activation, enhancing functional capabilities such as motility and phagocytosis without triggering classical pro- or anti-inflammatory cytokine release (**Figure 6A**). In experimental *in vivo* models of both early and late stages of Alzheimer disease experimental *in vivo* models, SULF A acts as a novel and promising small-molecule candidate for the therapeutic intervention by promoting microglial surveillance, facilitating the selective clearance of neurotoxic Aβ forms (**Figure 6B-C**), reducing Aβ plaque burden, and preserving vulnerable neuronal populations.

The collective data on SULF A underscore the potential of sulfated lipids as bona fide TREM2 ligands and open new avenues for investigating the role of endogenous sulfur-containing lipids in the brain.

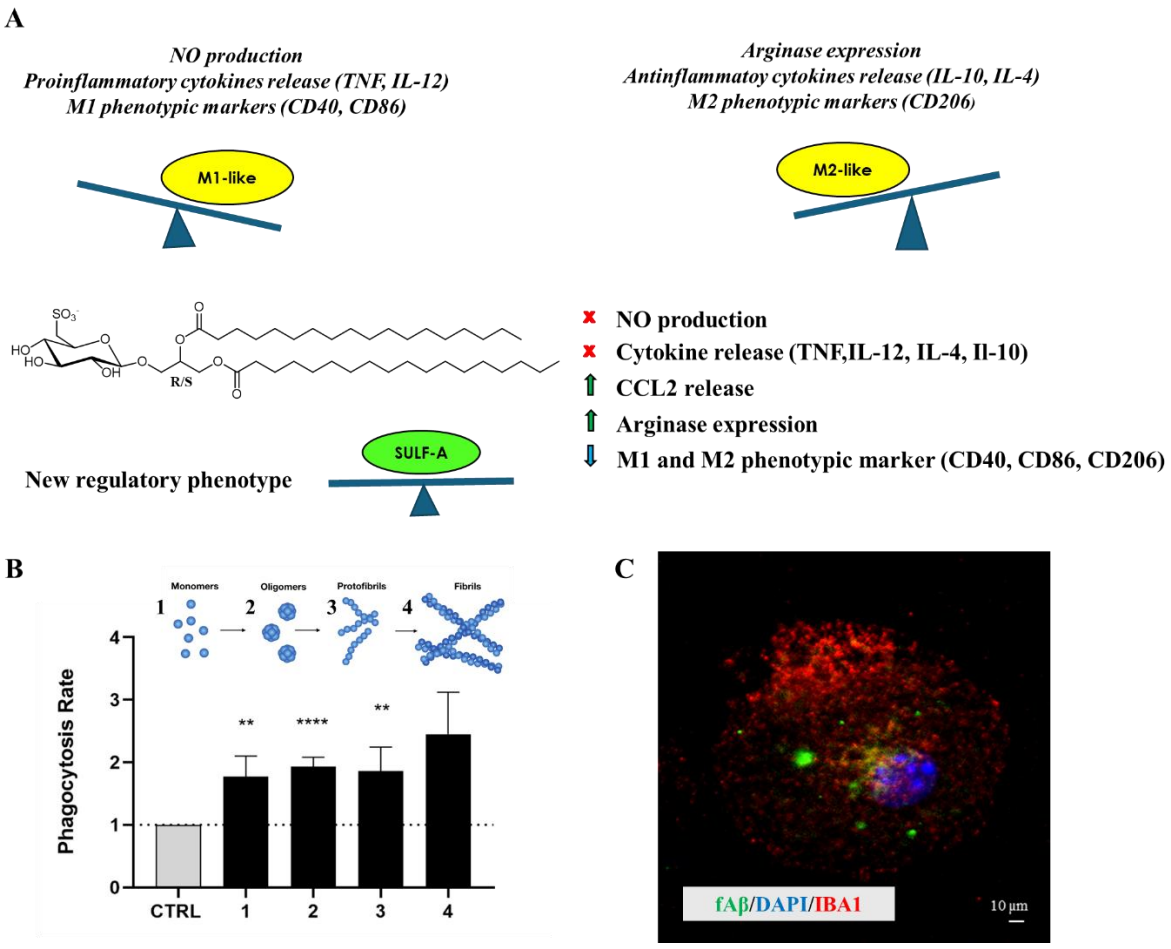

Figure 6 - Effect of Sulfavant A SULF A on primary mouse microglia (A) Induction of a novel regulatory phenotype by SULF A, compared with classical M1-like pro-inflammatory and M2-like anti-inflammatory states. (B) Phagocytosis assay conducted on primary murine microglia treated for 3 h (n = 4) with monomers (1), oligomers (2), prefibers (3) and fibers (4) of fAβ, untreated (CTRL) and stimulated with SULF A (10 µg/mL); data are expressed as phagocytosis rate calculated from the MFI after measurement of internalized fluorescence fibril intensity by flowcytometry (n = 3). (C) Representative confocal microscopy images of fAβ + SULF A treated murine primary microglia stained with DAPI (blue) and IBA1 (red) after phagocytosis assay for 3 hours with fAβ (green). (Gallo et al., 2025)

Another molecule that shares physicochemical similarities with PS and SULF-A is sphingosine-1-phosphate (S1P), a bioactive sphingolipid generated by phosphorylation of sphingosine. S1P consists of a long-chain amino alcohol backbone bearing a terminal phosphate group, conferring strong amphipathic properties. Beyond its canonical signalling via G-protein–coupled S1P receptors, S1P has recently been implicated as a potential TREM2 ligand, associated with increased phagocytic activity and enhanced microglial responsiveness *in vitro* and in ischemic models [54].

Finally, mycolic acids (MAs), long-chain fatty acids from mycobacterial cell walls, have been identified as potential TREM2 ligands. TREM2 recognizes non-glycosylated mycolic acids and, via DAP12, triggers ITAM/SYK signalling, influencing NF-κB and AP-1 activation, cytokine production, macrophage metabolism, and phagocytic activity. Unlike glycosylated MAs that signal via Mincle, TREM2 signalling is CARD9-independent [53]. During mycobacterial infection, engagement by non-glycosylated mycolic acids recruits iNOS-negative, permissive macrophages, highlighting TREM2 role in downregulating macrophage activation and favouring bacterial spreading [53].

1.4 Emerging therapeutic avenues for TREM2 in Alzheimer Disease: antibodies, hydrophobic small molecules, and peptide modulators

Antibody-based approaches have long constituted a fundamental strategy in modulating immune receptor function. Monoclonal antibodies directed against TREM2 have been engineered to enhance receptor activation, support microglial viability, and fine-tune phagocytic responses, particularly within the context of neurodegenerative disorders such as Alzheimer's disease. Preclinical investigations have shown that agonist antibodies can amplify TREM2 signalling, by promoting microglial proliferation and a more efficient clearance of amyloid in pathological animal models [59]. Mechanistic studies suggest that these antibodies engage the extracellular immunoglobulin-like domain of TREM2, triggering conformational shifts that emulate natural ligand binding and strengthen interaction with the adaptor protein DAP12. By stabilizing the flexible stalk proximal to the cleavage site (**Figure 7**), agonist antibodies promote receptor dimerization and ITAM phosphorylation, thereby enhancing downstream signalling and microglial functionality [60].

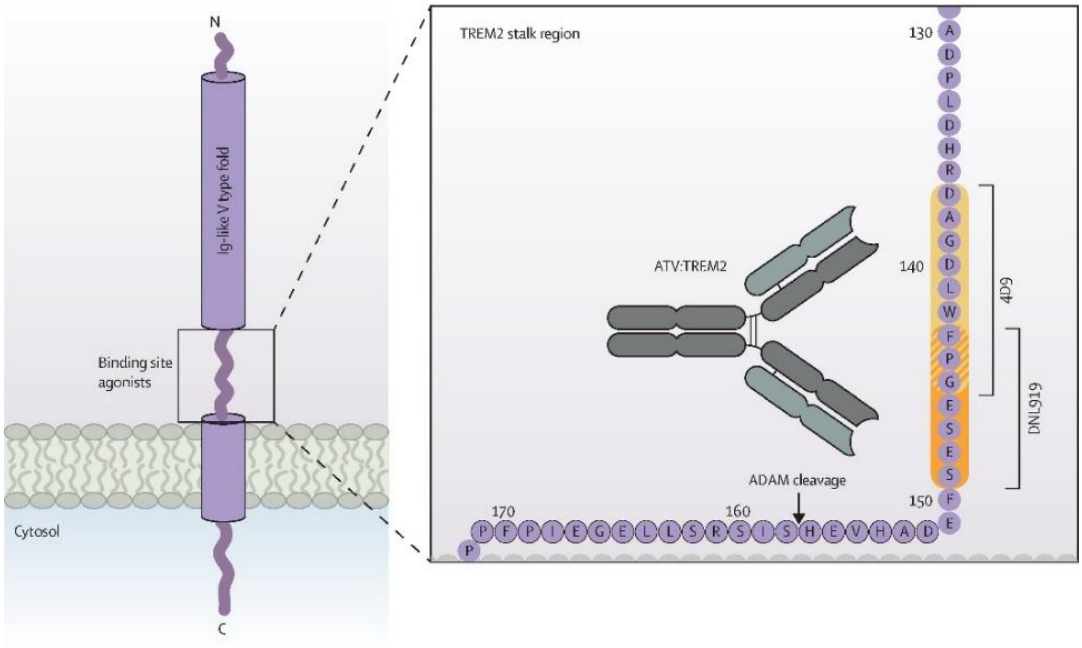

Figure 7 - Binding of agonistic anti-TREM2 antibodies and mechanism of transport across the blood–brain barrier (Schlepckow et al. 2023)

Despite encouraging preclinical data, several obstacles remain in the translational development of TREM2-targeting antibodies. These large molecules have a limited ability to cross the blood–brain barrier [61] and trigger off-target immune responses [60]. Prolonged receptor engagement further complicates therapeutic strategies, as chronic TREM2 activation can provoke receptor desensitization or downregulation, as proved in mouse models [62].

The INVOKE-2 trial, a Phase 2 study evaluating the TREM2-targeted antibody AL002 in early Alzheimer's disease, did not meet its primary endpoint of slowing clinical progression as measured by the Clinical Dementia Rating Sum of Boxes. Additionally, there were no significant effects on secondary clinical and functional endpoints, nor on amyloid PET imaging or fluid biomarkers [63]. This outcome has led to a reconsideration of TREM2-targeted therapies in Alzheimer's disease, highlighting the need for further research to understand the receptor's role and to optimize therapeutic strategies.

Among emerging alternatives to antibody-based therapies, synthetic hydrophobic small molecules (**Figure 8A**) have gained attention for modulating TREM2. These compounds engage the extracellular domain of TREM2, stabilizing its association with DAP12 and promoting downstream signalling (**Figure 8B**), while avoiding the steric hindrance and immunogenicity typically associated with antibodies.

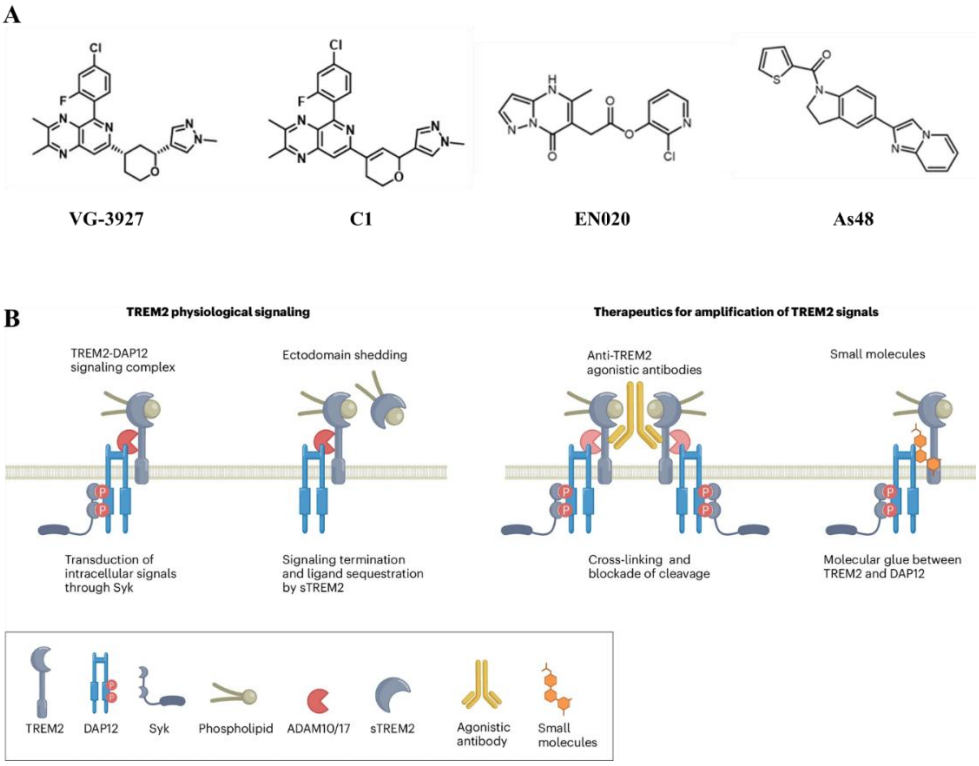

Figure 8 - Schematic overview of physiological TREM2 signalling and its therapeutic amplification through strategies aimed at potentiating receptor activation. (A) Chemical structures of small-molecule TREM2 agonists VG-3927, C1, EN020, and AS48. TREM2 signalling and therapeutic targeting. (B) Phospholipid ligands activate TREM2 at the microglial surface, triggering DAP12 phosphorylation and SYK signalling. ADAM10/17-mediated shedding limits receptor signalling and releases soluble TREM2. Agonistic antibodies and small molecules enhance TREM2 clustering or stabilize its interaction with DAP12, thereby amplifying downstream activation. (Marco Colonna and David M. Holtzman, 2025)

VG-3927 (heteroaromatic compound) is the first orally bioavailable and selective agonist of the microglial receptor TREM2. Identified through structure-based virtual screening, VG-3927 enhances microglial phagocytosis and potentiates DAP12-mediated ITAM phosphorylation, thereby reinforcing innate immune responses in the central nervous system. Preclinical data demonstrate favourable CNS penetration and pharmacokinetics, and the compound is currently under clinical development for Alzheimer's disease [64]. C1, a structural analogue of VG-3927, was designed to improve metabolic stability and CNS penetration while retaining TREM2 agonism. Molecular docking studies indicate that C1 forms stable polar and hydrophobic interactions with the extracellular domain of TREM2, supporting its functional activity [65]. EN020 (heterocyclic compound containing nitrogen and chlorine atoms), discovered via AI-assisted virtual screening, binds TREM2 with high affinity and promotes microglial phagocytosis in BV2 cells. Its activity, however, is sensitive to scaffold modifications, highlighting the need for further optimization to enhance potency and specificity [66]. Finally, As48 was identified through affinity selection-mass spectrometry as a selective TREM2 modulator, displaying ~7-fold

higher affinity for TREM2 over TREM1. As48 acts both as an agonist and as an inhibitor of ADAM-mediated TREM2 shedding, offering a strategy for fine-tuned modulation of microglial function [67]. Small-molecule agonists of TREM2 represent an exciting frontier in microglial modulation, yet their translation into effective therapies remains challenging (64,66) , since sustaining the exposure without off-target effects or metabolic instability remains difficult [68]. Moreover, the complexity of TREM2 signalling-capable of both neuroprotective and pro-inflammatory outcomes- demands careful tuning rather than simple activation (55,69).

SCHOOL (Signalling Chain HOmoOLigomerization) is a new promising strategy, which targets single-chain immune receptors by perturbing critical intra-complex interactions rather than competing with endogenous ligands [70]. Unlike antibodies and small-molecule agonists that directly target TREM2, this technique involves the use of synthetic peptides as a new class of ligand-independent modulators [70]. In this context, the peptide IA9 (sequence IFLIKILAA), is selectively inserted between the transmembrane domain of TREM2 and its signalling adaptor DAP12 (**Figure 9A-B**). By interfering with the assembly of the functional receptor complex TREM2-DAP12, IA9 blocks downstream pathway, providing a novel and orthogonal mechanism to modulate TREM2-mediated immune responses [71].
In vivo, IA9 demonstrated therapeutic potential in a collagen-induced arthritis mouse model, significantly reducing joint inflammation, tissue damage, and proinflammatory cytokine release, highlighting its utility as a ligand-independent TREM2 inhibitor for controlling autoimmune and inflammatory responses [71]. Furthermore, in central nervous system cancer models, IA9 disrupted TREM2–DAP12 interactions, modulated microglial immune responses, and influenced tumour growth in a TREM2-dependent manner, suggesting its broader applicability as a ligand-independent therapeutic agent in both inflammatory and neoplastic context [72].

Beyond its therapeutic intent, IA9 provides a unique experimental tool to probe TREM2 function *in vitro*, enabling mechanistic dissection of receptor-mediated signalling pathways. IA9 selectively perturbs the assembly of the TREM2-DAP12 signalling complex, offering a ligand-independent means to interrogate receptor activation. This approach has never been described before but could allow the distinction between direct ligand-induced effects and intrinsic TREM2-dependent signalling, revealing downstream pathways responsible for phagocytosis, cytokine release, and microglial activation.

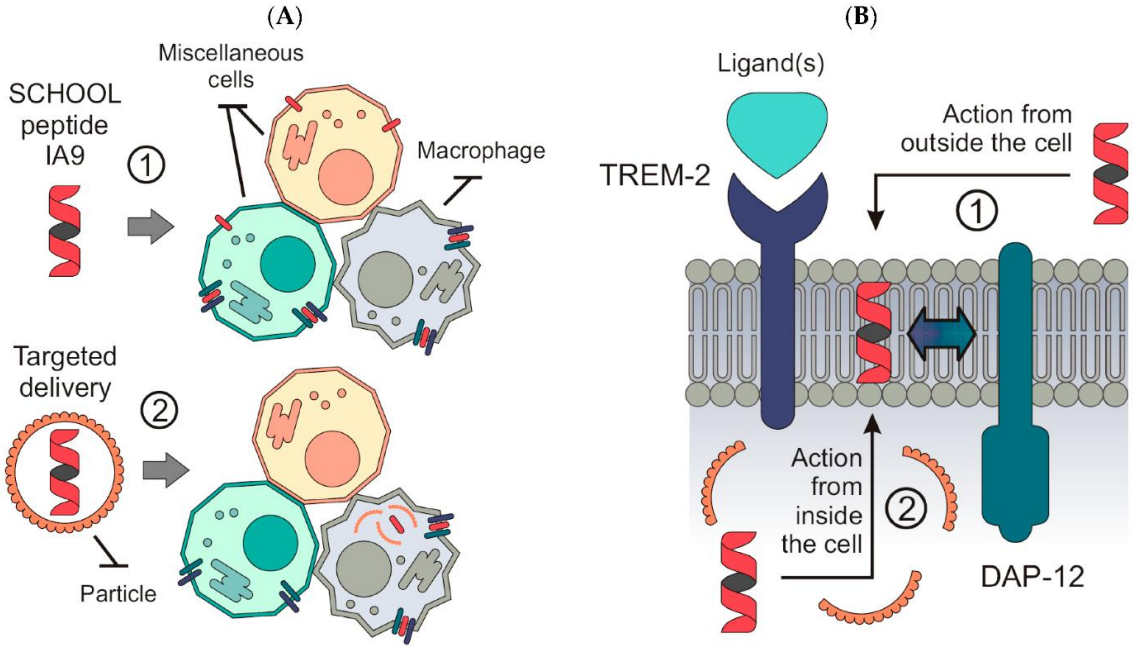

Figure 9 - Schematic representation of ligand-independent TREM2 inhibition and macrophage-targeted delivery. (A) IA9 inserts into the membrane either externally or internally, blocking TREM2 on expressing cells. B) Similar to other SCHOOL peptides, IA9 inhibits TREM2 by disrupting its interaction with DAP12.

Aim of the thesis

The primary objective of this PhD project is to advance the mechanistic understanding of TREM2 activation by small molecules, with particular emphasis on elucidating the molecular principles that govern receptor engagement and signal propagation. Although TREM2 is a central microglial receptor orchestrating immune surveillance, phagocytic clearance, and neuroinflammatory responses in the central nervous system, the identity and mode of action of its physiological mediators remain only partially defined. Clarifying these endogenous drivers of TREM2 function is essential for reconstructing the behavior of the receptor in native, physiologically relevant settings and for resolving the molecular cues that dictate its activation dynamics and downstream response.

This mechanistic endeavor is grounded in the characterization of Sulfavant A as a probe to dissect receptor signalling, and is guided by three principal aims:

1. **Addressing the architecture of receptor–adaptor communication at the molecular level** by combining small molecule-dependent activation assays with targeted biochemical perturbation of the TREM2-DAP12 axis, employing synthetic DAP12-affine peptides as mechanistic probes to selectively modulate and illuminate TREM2 signalling.

2. **Interrogating physiological mechanisms in mammalian systems** through the comprehensive chemical profiling of sulfur-containing metabolites in the mouse brain and the establishment of an integrated bioassay platform to evaluate their TREM2-dependent activities.

3. **Identifying candidate physiological mediators of TREM2**, emerging from the chemical and functional profiling of brain-derived sulfur-containing compounds, and evaluating their capacity to engage and modulate the receptor under biologically relevant conditions.

Section II: Results and discussion

Chapter 2

TREM2-dependent activity: insights into the IA9-K inhibitor peptide

2.1 Evaluation of biological effects of IA9-K peptides

The study of TREM2 signalling with specific putative agonists requires a system that can selectively inhibit receptor activation. In this context, the inhibitory peptide IA9-K (IFLIKILAA), previously described in section 1.4, represents a valuable tool for such investigations.
The ability of IA9-K to inhibit TREM2-signal was evaluated using a TREM2 reporter cell system gifted from Prof. Marco Colonna [39]. This cellular model is an immortalized murine lymphocytic cell line, transfected with the human TREM2-DAP12 expression vector, and the eGFP reporter gene, placed under the control of NFAT (nuclear factor of activated T cells) responsive regulatory elements, that represents the best-characterized transcription factor downstream of TREM2 signalling [55]. Receptor activation can be quantitatively assessed by measuring the percentage of GFP-positive cells through flow cytometry.

IA9-K was tested for the ability to interfere with TREM2 activation at the concentrations of 100 μM and 250 μM (PBS/DMSO 1:1, v/v, 2%), as established from preliminary titration experiments.

The obtained results showed as the biological activity of this peptide was markedly influenced by its counterion (**Figure 10**). Trifluoroacetate (TFA) salt of IA9-K effectively inhibited TREM2-mediated signalling in a dose-dependent manner upon stimulation with mycolic acid (15 μg/mL), used as a positive control, reaching nearly 50% inhibition compared to the vehicle-treated control (**Figure 10A**). However, when a subsequent batch of the peptide, reformulated as hydrochloride (HCl) salt to remove the TFA counterion, was tested under the same conditions, its inhibitory capacity was substantially reduced, achieving only ~25% inhibition at both concentration (**Figure 10B**). This discrepancy initially observed by chance, highlighted a potential role of the counterion in shaping peptide behaviour. These findings suggest that the ionic microenvironment could critically influence the conformational landscape

of IA9-K and, in turn, its ability to interfere with TREM2–DAP12 signalling. This observation prompted a biophysical characterization aimed at elucidating the mechanism underlying this effect.

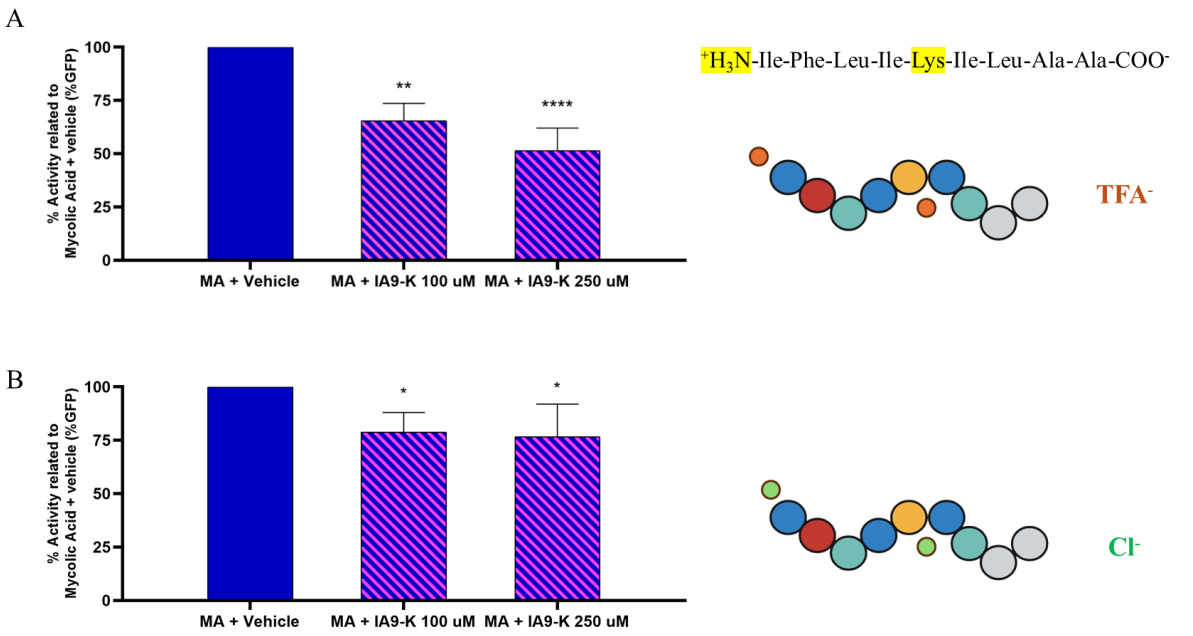

Figure 10 - Effect of IA9-K associated-counterion- on TREM2 reporter activity. Activity is expressed as the percentage of GFP-positive cells relative to positive control mycolic acid (15 µg/mL) stimulation in the presence of the vehicle control (PBS/DMSO 1:1, v/v, 2%); A) dose-dependent inhibitory activity of IA9-K in its trifluoroacetate (TFA) form; B) dose-dependent inhibitory activity of IA9-K following exchange with hydrochloride (HCl). For each experiment, two independent measurements had been reported (n=2). Ordinary one-way ANOVA, * $p \leq 0.05$. ** $p \leq 0.01$, **** $p \leq 0.0001$ vs vehicle control.

The inhibitory effect of the IA9-K peptide was confirmed by the analysis in system of Fluorescence lifetime imaging microscopy (FLIM) combined with Förster resonance energy transfer (FRET) specifically designed to monitor the proximity and dynamics of protein–protein interactions (manuscript in preparation). In this experimental setup, the immortalized human microglial cell line HMC3 [73] was co-transfected with TREM2–mTurquoise (donor) and DAP12-YPet (acceptor) fusion constructs, allowing the visualization of the interaction between the two proteins in living cells (Section III, paragraph 5.5). In a FLIM-FRET system, the fluorescence lifetime (τ) reflects the average time that the donor fluorophore remains in its excited state before photon emission [74]. The energy transfer to an acceptor shortens this lifetime and provides a sensitive measure of molecular proximity. As shown in **Figure 11A**, τ initially decreased slightly at ~30 s relative to time 0, followed by a progressive increase from ~2 min that was subsequently maintained over time. This pattern suggests that, from approximately

1 min onward, the two proteins underwent spatial separation, likely driven by the specific interference of the peptide IA9-K, and provides a direct indication of the capacity of peptide to modulate TREM2-dependent signal transduction. A scrambled version of IA9-K, in which the nine amino acids were rearranged to generate the sequence ILKAIALFI, was synthesized and tested as a negative control in this system. This scrambled IA9-K did not induce any variation in τ over time (**Figure11B**).

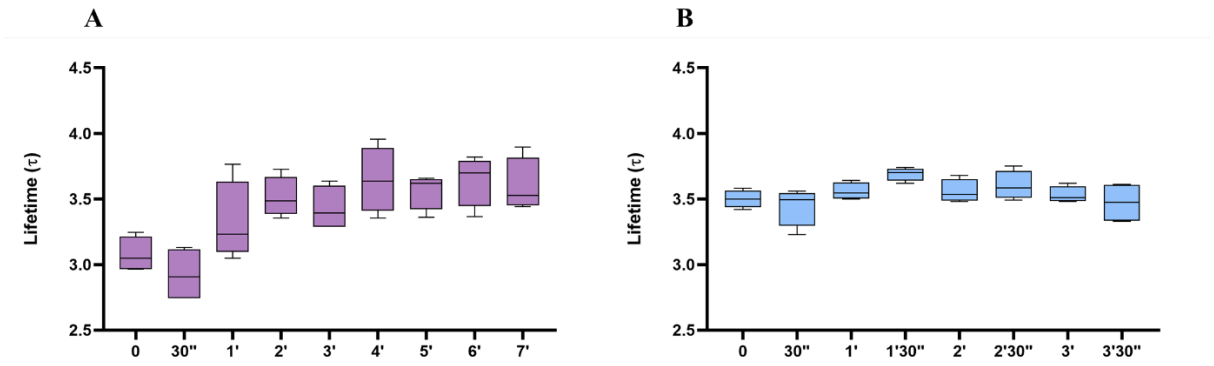

Figure 11 - **Temporal distribution of fluorescence lifetime;** highlighting dynamic changes in donor–acceptor proximity upon IA9-K (A) and scramble (B) treatment (5 µg/mL, vehicle DMSO 0.5 %). Three ROIs were analysed for each time point.

2.2 Secondary structures of IA9-K peptides in membrane-mimicking environments

Given their predominantly hydrophobic nature and membrane-targeted activity, initial attempts were made to characterize the peptides IA9-K (TFA) and IA9-K (HCl) by circular dichroism (CD) in small unilamellar vesicles (SUVs). However, their limited solubility in water prevented the application of this approach. Faced with this limitation, CD analyses were performed in water–trifluoroethanol (TFE)

mixtures spanning 20–100% TFE; This system is considered a suitable compromise for studying peptide structure under membrane-mimicking conditions [75].

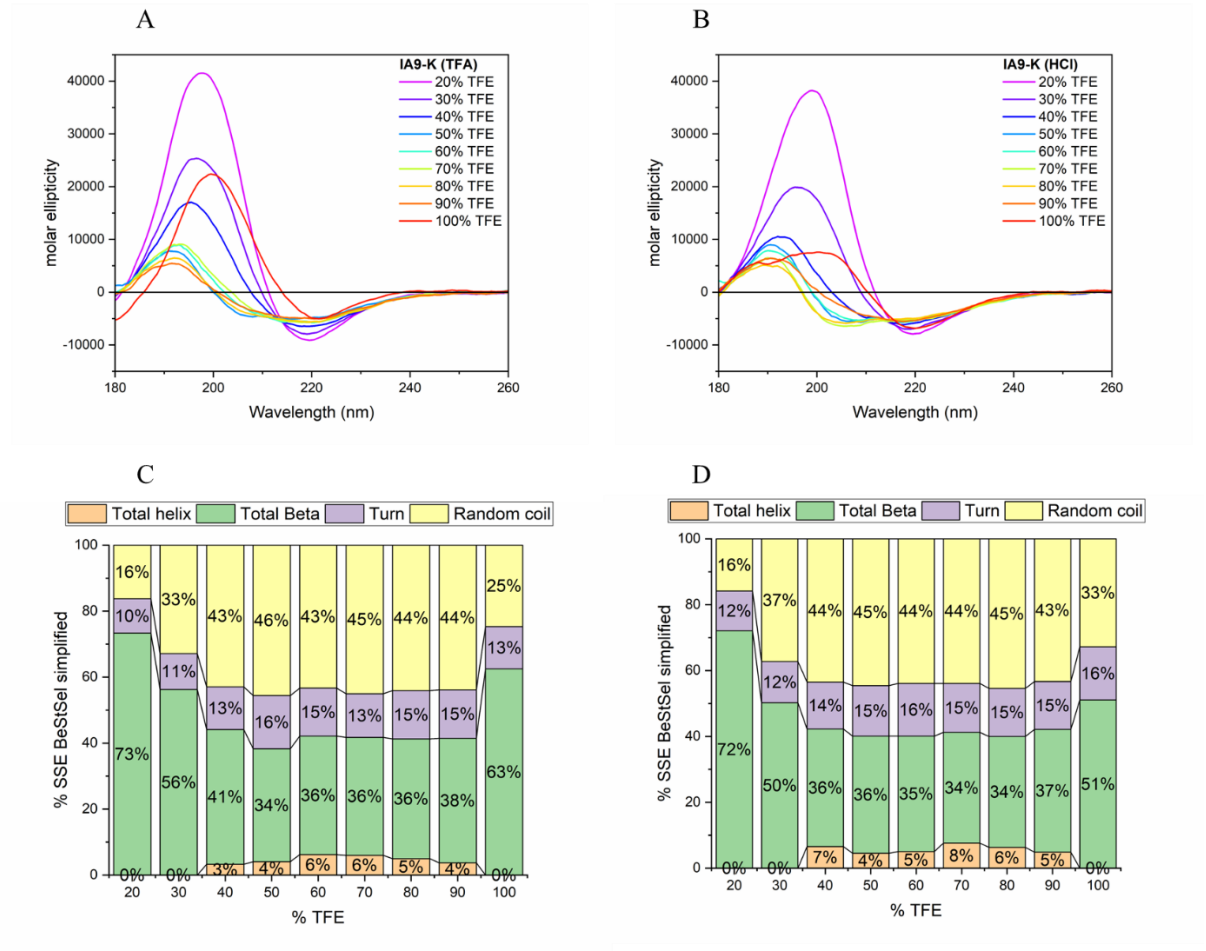

Figure 12 – Circular dichroism spectra of IA9-K/TFA, and IA9-K/HCl peptides recorded in different water–TFE mixtures (20-100% TFE). Peptides were dissolved in pure TFE and diluted with appropriate solvent to a final concentration of 0.1 mg/mL. (A–B) Spectra were collected in the 180–260 nm range and converted to molar ellipticity. (C–D) Simplified secondary structure predictions obtained using the BeStSel algorithm, showing the relative contributions (%) of total helices, total β-sheets, turns, and random coil components.

Contrary to expectations for a transmembrane domain fragment, CD spectra across all conditions lacked pronounced α-helical features and instead revealed a β-like conformation for both peptides (**Figure 12A–B**). Spectral data were analyzed using the BeStSel platform [76], which deconvolutes CD spectra to estimate secondary-structure content and is particularly accurate for β-sheet–rich peptides (**figure 12C-D**). BeStSel analysis indicated that, at 20% TFE, both peptides adopted a predominantly β-sheet conformation (~70%), with minor contributions from turns (~10%) and disordered regions (~16%). Increasing TFE levels progressively reduced β-structural content and enhanced disorder, until a stable

conformational equilibrium was reached at 40–50% TFE and maintained up to 90% TFE. This trend was observed in the spectra by a gradual decrease and blueshift of the maximum at 197 nm (toward 190 nm) and a reduction of the negative band near 210 nm. At intermediate TFE concentrations (40–90%), only minor α-helical contributions (<10%) were detected, and these remained within the uncertainty of the method. Nevertheless, the characteristic α-helical signature, defined by the double negative bands at ~208 and ~220 nm and the positive band at ~195 nm, became discernible between 60–90% TFE for IA9-K (TFA) and 60–80% TFE for IA9-K (HCl). Under fully hydrophobic conditions (100% TFE), both peptides regained substantial β-structuration, approximately 50% for IA9-K/HCl and 63% for IA9-K/TFA, marking a divergence between the two samples. IA9-K/TFA exhibited a slight redshift of the λ max (200 nm) and a lower overall intensity compared with 20% TFE, while IA9-K/HCl showed even weaker spectral features. CD spectra were analysed using the BeStSel algorithm, which provides a reasonable approach for probing secondary-structure features in β-rich and conformationally flexible peptides, although it is generally more optimized for proteins. For completeness, peptide-specific reference sets, such as those introduced by Reed and Reed [77], may offer a complementary framework for evaluating CD-based structural analyses.

Analyses conducted in TFE offer insight into the conformational preferences these peptides may adopt under hydrophobic conditions; however, such observations should be validated through complementary studies in intact membrane environments. In this context, *Oriented Circular Dichroism* (OCD) was employed to measure the differential absorption of circularly polarized light by aligned lipid–peptide samples, yielding information on both the secondary structure and orientation of membrane-associated peptides [78]. OCD is widely used for α-helical cell-penetrating peptides, for which Moffitt's theory allows the observed spectrum to be related to the angle of the helix relative to the bilayer [79]. The CD signature of β-structured peptides, however, is considerably more complex, and the diversity of β-sheet arrangements (e.g., parallel, antiparallel, twisted, β-helical) precludes a comprehensive quantitative model or standardized interpretation. Nevertheless, qualitative spectral features can still reveal the probable orientation of β-structured peptides within the membrane, whether lying parallel to the bilayer, spanning it perpendicularly, or adopting intermediate tilt angles, as well as providing insight into their interactions with the lipid environment. Specifically, previous studies on helical antimicrobial peptides [80] have observed that at low peptide-to-lipid (P/L) ratios, the peptides tend to adopt a carpet-like arrangement, lying parallel to the membrane surface. As the P/L ratio increases, the peptides progressively shift their orientation toward an inserted state. Building on these premises, the spectral differences observed between experiments performed at peptide-to-lipid ratios (P/L) 1:15 and at P/L of 1:60 were used to infer the possible orientation of the analysed peptides.

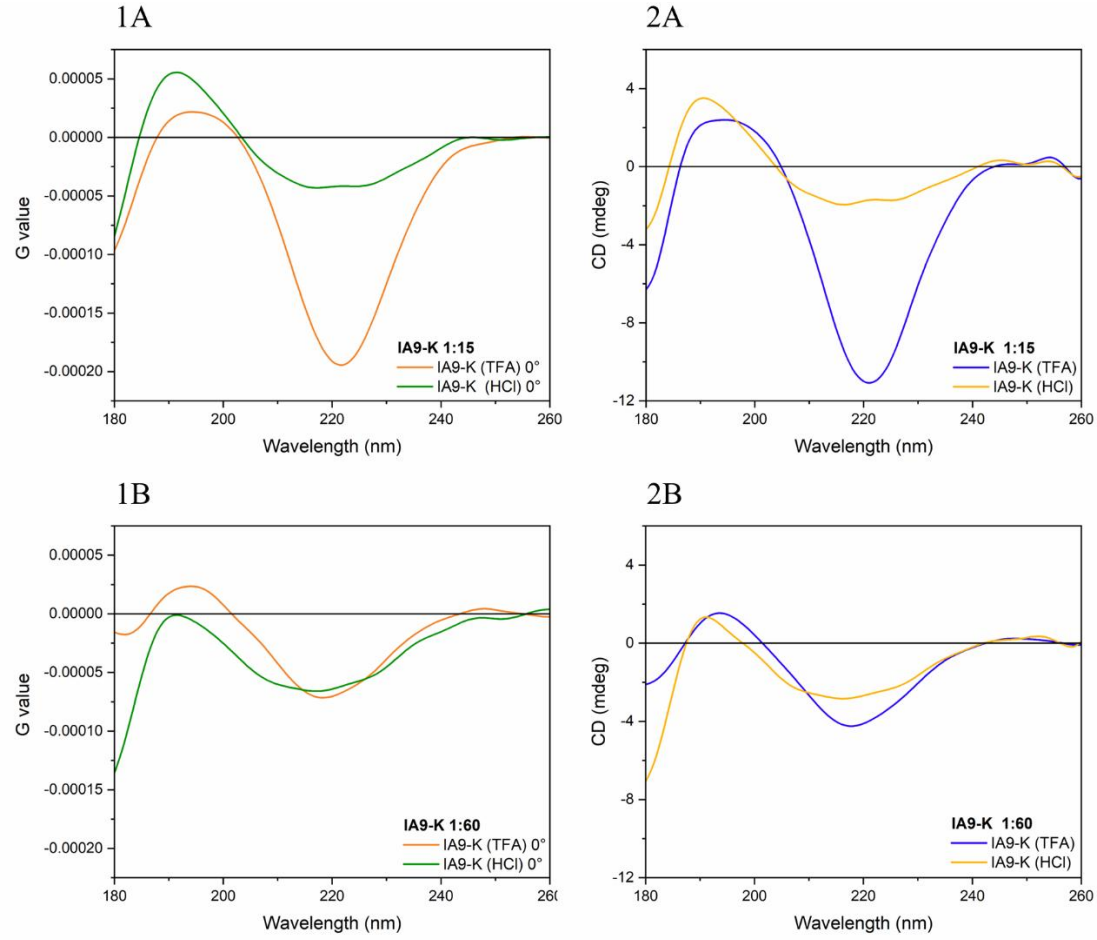

Figure 13 – **Oriented circular dichroism (OCD) of IA9-K/TFA and IA9-K/HCl synthetic peptides recorded in DMPG/DMPC 1:3 at a 0° angle**. Peptides were dissolved in $CHCl_3/CH_3OH$ (1:1, v/v) at a final concentration of 2.44 mg/mL and mixed with phospholipids (DMPG/DMPC 1:3) yielding a P/L ratio of 1:15 (1A-2A) and a P/L ratio of 1:60 (1B-2B). Spectra were collected in the 180–260 nm range express in terms of mdeg and normalized as G-value.

The peptides were dissolved in $CHCl_3/CH_3OH$ (1:1, v/v) at a concentration of 2,44 mg/mL and co-dissolved with a mixture of dimyristoyl-phosphatidylglycerol (DMPG) and dimyristoyl-phosphatidylcholine (DMPC) in a 1:3 molar ratio, also dissolved in $CHCl_3/CH_3OH$ (1:1, v/v) at 10 mg/mL, at two distinct P/L of 1:15 and 1:60. For OCD measurements, the sample was deposited onto a fused silica window, and the solvent is removed to form a dry film.

To perform solid-state measurements, an in-house built cell was employed (ICB-CNR laboratories of Padua – Department of Chemistry, University of Padua, Italy): it consists of a simple PEEK hollow cylinder (with octagonal bases, more accurately described as a right octagonal prism geometry) that accommodates two round fused silica windows (one with the deposited peptide/lipid sample, the second to create a sealed chamber) and contains a small reservoir for taking up an aqueous salt solution for humidifying the sample. The incident light beam is perpendicular to these windows, and between scans

the cell is rotated around the beam direction, and flipped front-to-back, for averaging of the spectra to minimize linear dichroism (LD) artifacts. The geometry of the cell was studied to maintain the sample at the same distance from the detector when flipping the cell front-to-back.

In solid-state samples the effective concentration of chiral molecules and the optical path length are often difficult or impossible to define precisely. This makes direct comparison of CD intensities unreliable. To overcome this limitation, the CD signal is expressed as the G factor (also called the anisotropy factor), which normalizes the difference in absorption of left- and right-circularly polarized light by the total absorbance. Because the G factor is dimensionless and independent of sample thickness or concentration, it provides a consistent measure of intrinsic chiroptical activity, allowing meaningful comparison between different samples. Since CD spectra may be influenced by LD, spectra were collected at multiple sample orientations [81], which are at 0° and 90° for the front face, and the flipped front-to-back and measured at the same 0° for the back face. No appreciable differences were observed among orientations (Appendix A). **Figure 13** shows the 0° spectra of IA9-K/TFA and IA9-K/HCl at both P:L ratios. At P/L ratio 1:15, IA9-K/TFA displayed a markedly deeper minimum near 220 nm compared with IA9-K/HCl, which instead exhibited a slightly more intense maximum around 190 nm. These spectral features are consistent with β-structured conformations; however, the counterion appears to modulate peptide orientation within the membrane. Specifically, at a P/L ratio of 1:60 (**Figure 13-1B**) both peptides show similar spectra, whereas at P/L 1:15 (**Figure 13-1A**) IA9-K/HCl shows a CD spectrum similar to those observed at low P/L ratio, at which, according to literature data, the peptides tend to adopt a carpet-like arrangement. Conversely, IA9-K/TFA shows an increased intensity of the negative band, along with a slight shift of the λ_{max} from 219 to 222 nm, likely suggesting a change in peptide orientation towards insertion in-between phospholipid acyl chains. The CD spectra in **Figures 13-2A** and **13-2B** are likewise presented in mdeg, showing the same overall spectral features. However further experiments are needed to identify the spectra corresponding to the completely inserted state, the completely surface-bound state, and the intermediate states, in order to confirm if the observed pattern can be attributed to a tilted or inserted positioning of the IA9 peptides relative to this specific lipid system [82].

2.3 Exploring counterion effects in IA9-K peptides by NMRtist

Complementing the circular dichroism analyses, the influence of counterions was further explored via NMR spectroscopy. Due to their very limited solubility, the peptides could only be prepared at a relatively low concentration of 0.5 mM in 100% DMSO-d_6, and they were essentially insoluble at lower DMSO percentages, particularly in aqueous conditions. 2D COSY, TOCSY, and ROESY spectra were

then acquired. While DMSO serves as the solvent for peptide preparation and subsequent introduction into the biological system, its strong far-UV absorbance precludes CD measurements. To obtain a 3D representation of the plausible conformations of the two peptides in pure DMSO, the acquired spectra were further processed using NMRtist, an advanced computational platform that performs automatic resonance assignment and integrates experimental NMR data with machine learning algorithms to generate 3D structural models of peptides and proteins. [83].

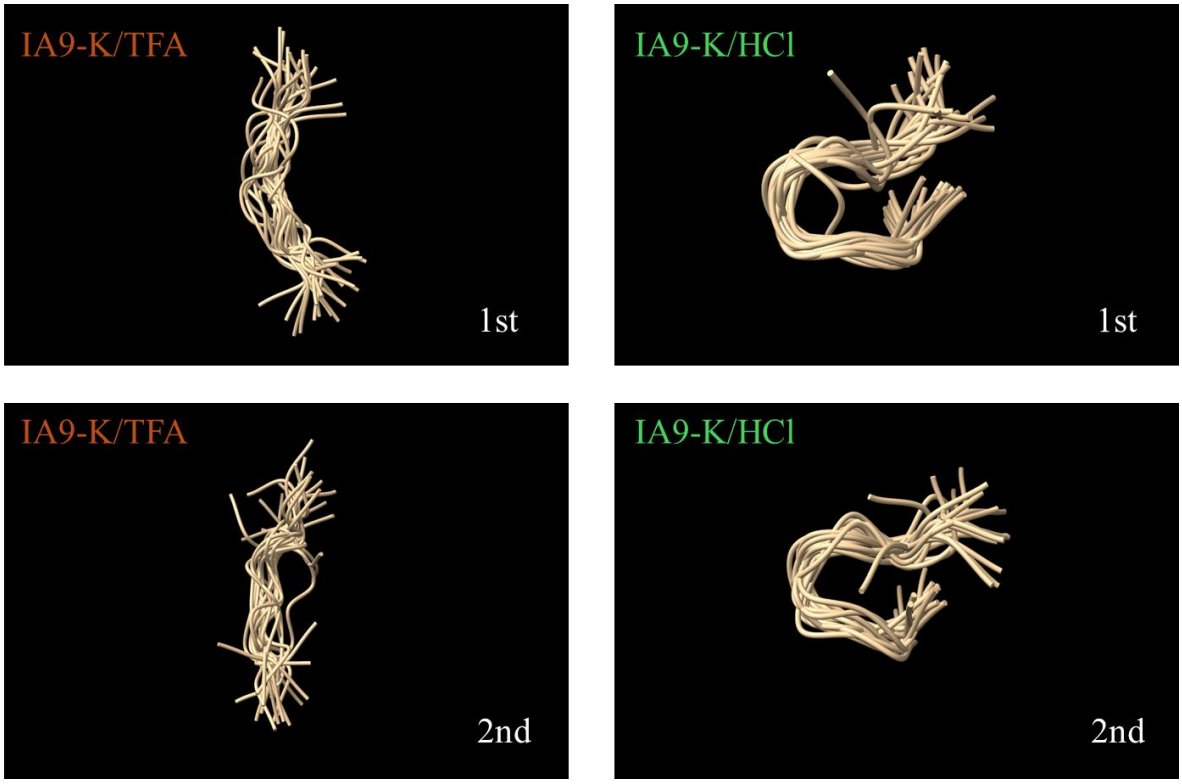

Figure 14 – **Molecular representations generated with ChimeraX 1.10 of the IA9-K/TFA and IA9-K/HCl peptide models obtained from NMRtist calculations in 100% DMSO**. Two structural models (1st and 2nd) were generated, comprising ensembles of twenty conformers.

For each peptide, two structural models (1st and 2nd) were generated, each comprising an ensemble of twenty conformers (**Figure 14**). The analysis revealed a clear trend, showing that TFA salt of IA9-K adopts a stretched conformation modestly folded only in the central region, whereas exchange to the HCl form promotes a markedly more pronounced folding, resulting in a "U" shaped form bringing closer spatial arrangement of residues within the central segment.

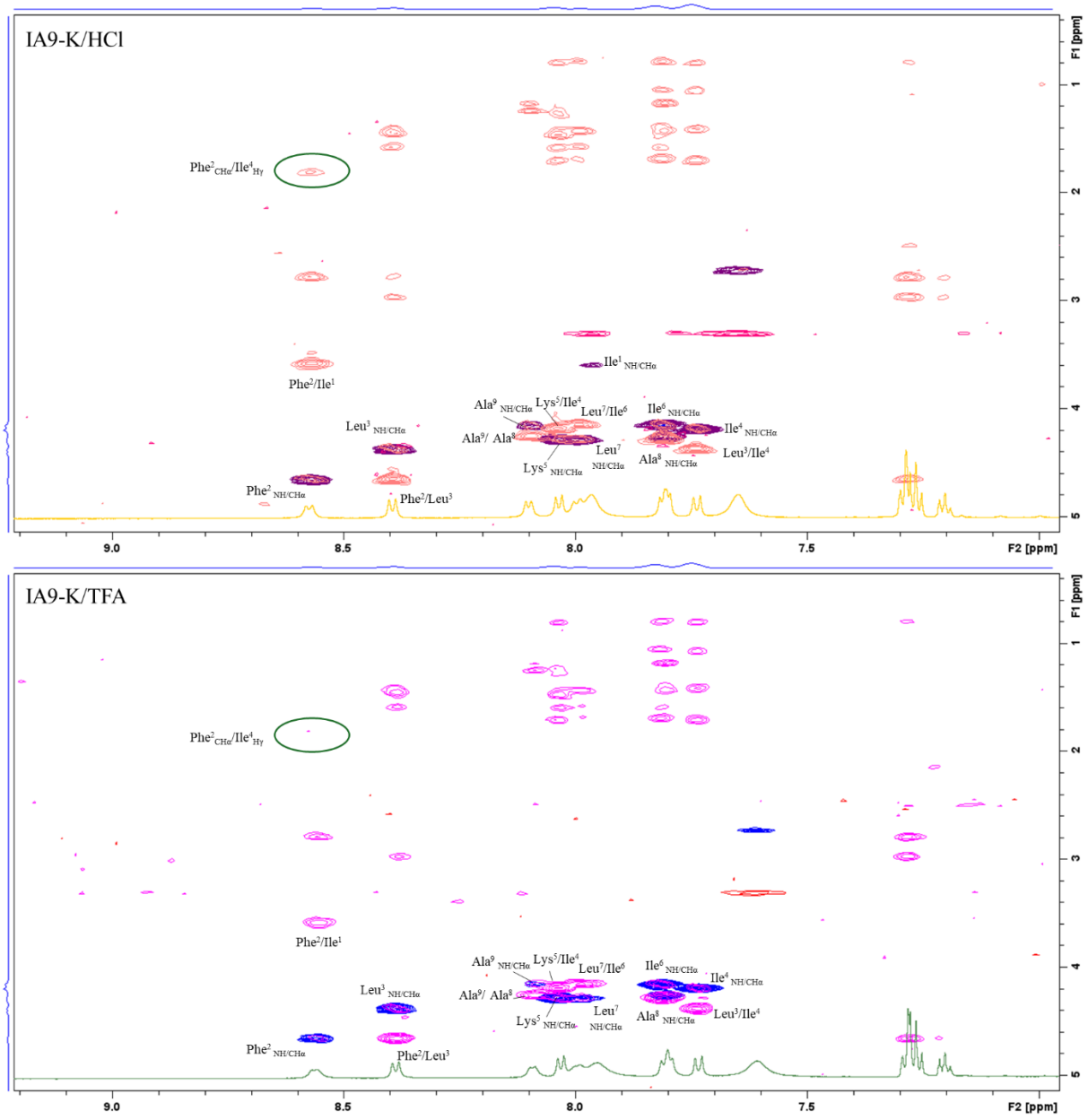

Figure 15 – **Amide-resonance detail of COSY (purple in the upper panel, and blue in the lower panel) and ROESY (red in the upper panel, and magenta in the lower panel) 2D-NMR spectra of IA9-K peptides in 100% DMSO-D$_6$.**

To further validate the structural features inferred from the computational models, a comparison was performed between the 2D NMR spectra of the two peptide forms. The overlay of the COSY (blue/dark violet) and ROESY (purple/red) spectra reveals a distinctive cross-peak present in IA9-K/HCl yet missing in IA9-K/TFA (within and missing in the green circle in the upper and lower panels, respectively, of **Figure 15**). Focusing on phenylalanine, the second residue from the N-terminus, this

weak cross-peak originates from the spatial proximity between its α-proton and one of the γ-methylene protons (–CH_2) of isoleucine 4. This observation is consistent with the more pronounced folding identified in the structural models, which brings these residues into close spatial contact.

2.4 Counterion-dependent folding of IA9-K variants

The investigation of counter-ion effects on IA9 peptides was extended to variants featuring sequence modifications. Peptides named IA9-G (IFLIGILAA) were synthesized, in which lysine was replaced with glycine to completely remove the positive charge and render the peptide fully hydrophobic. Both the TFA and HCl salts were prepared for IA9-G. Additionally, a scrambled version of IA9-K was synthesized, in which the positions of the nine amino acids were rearranged, yielding the sequence ILKAIALFI. With the aim of evaluating these peptides in biological systems, the same physicochemical characterization previously performed for IA9-K was also carried out for these variants.

The study in the hydrophobic environment of TFE revealed no significant differences between IA9-G/TFA and IA9-G/HCl, with both peptides displaying a tendency to adopt β-sheet structures. Compared to IA9-K, the contribution of β-structuring was estimated at 40–45% under all conditions analyzed, based on BeStSel processing. Analysis of the CD spectra showed that for IA9-G/TFA (**Figure 16A**), the positive band around 200 nm exhibited a slight increase from 20% to 50% TFE, followed by a decrease leading to a pronounced minimum, indicative of an overall increase in disorder, which was not reflected in the BeStSel analysis. The negative band around 220 nm remained relatively constant up to 70% TFE, after which a progressive loss of intensity was observed. In the case of IA9-G/HCl (**Figure 16B**), the positive band at 200 nm reached maximum intensity at 20% TFE and gradually decreased with increasing TFE content. The behavior of the negative band around 220 nm was identical to that observed for IA9-G/TFA.

Regarding IA9-K scramble, the peptide was minimally affected by variations in the water/TFE ratio, displaying a CD spectrum characterized by a pronounced minimum at 200 nm and a less intense minimum between 210 and 220 nm. Additionally, the spectra exhibited a positive band at 190 nm, whose intensity was lowest at 20% TFE, increased to a maximum from 30% TFE, and then decreased again beyond 80% TFE (**Figure 16C**). BeStSel analysis did not reveal significant variations across the different conditions; however, consistent with the overall spectral profile, a higher degree of disorder was observed compared to both IA9-K scramble and IA9-G (**Figure 16D-F**).

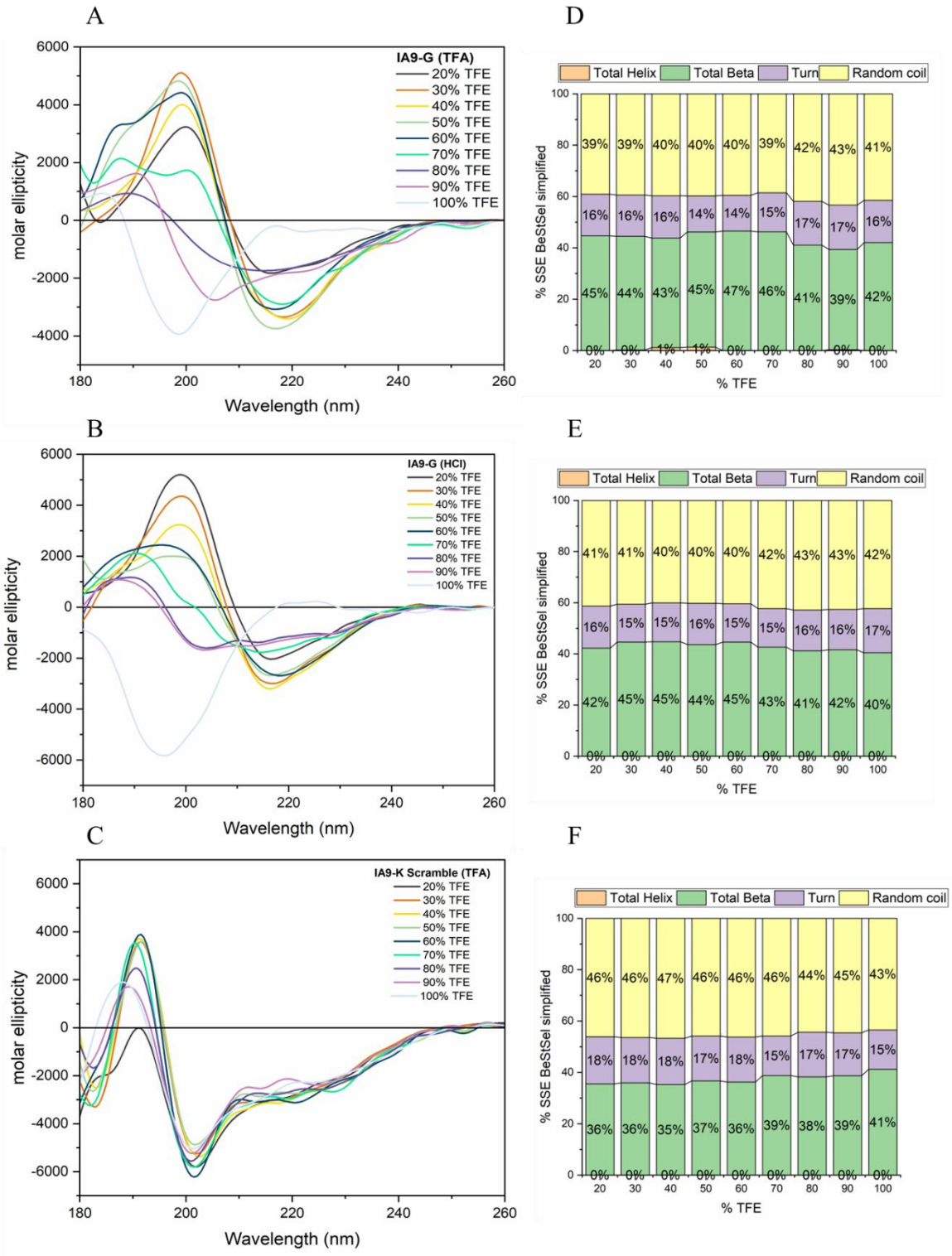

Figure 16 - Circular dichroism spectra of IA9-G/TFA, IA9-G/HCl and IA9-K scramble peptides recorded in different water–TFE mixtures (20-100% TFE). Peptides were dissolved in pure TFE and diluted with appropriate solvent to a final concentration of 0.1 mg/mL. (A–C) Spectra were collected in the 180–260 nm range and converted to molar ellipticity. (D–F) Simplified secondary structure predictions obtained using the BeStSel algorithm, showing the relative contributions (%) of total helices, total β-sheets, turns, and random coil components

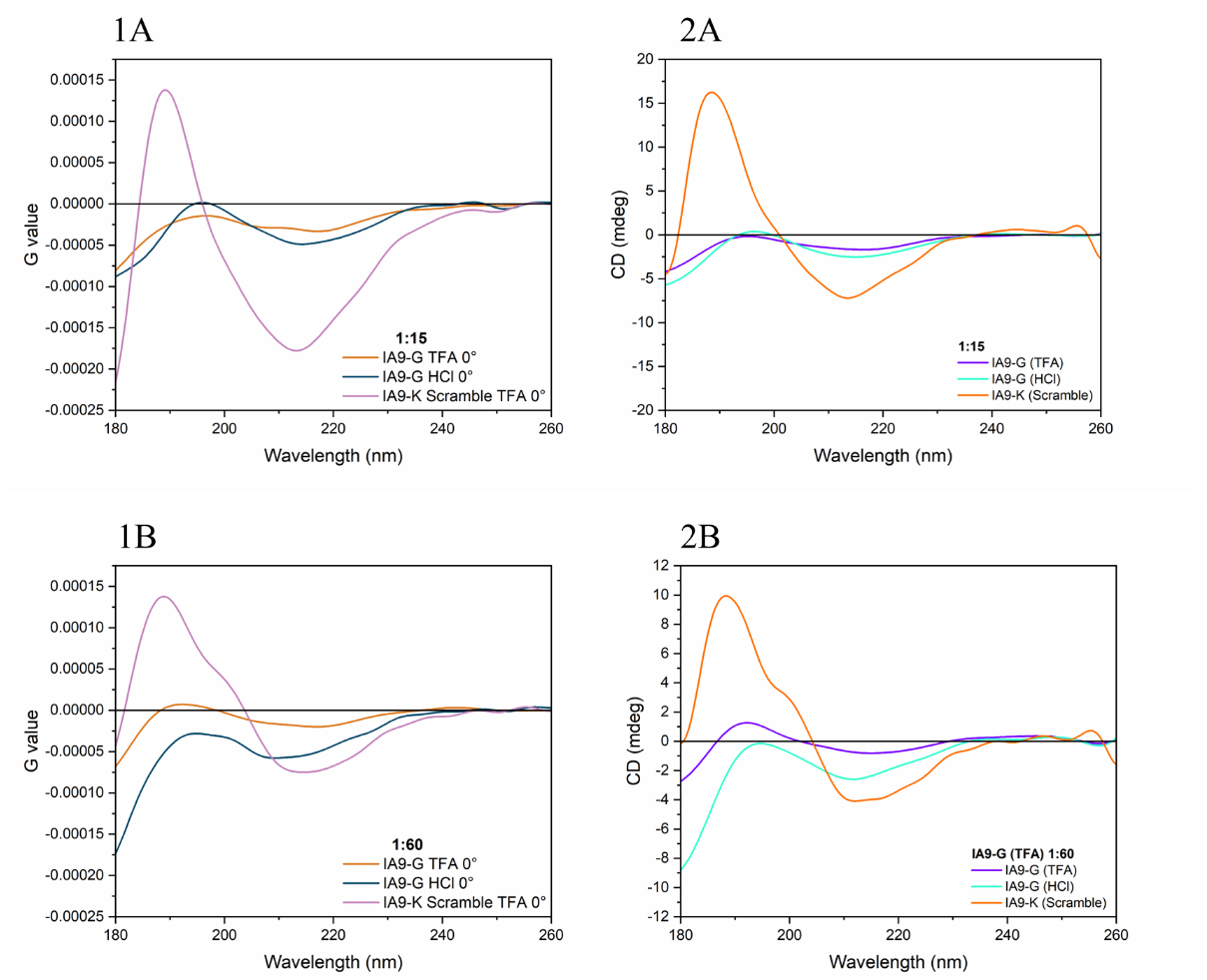

Figure 17 – Oriented circular dichroism (OCD) of IA9-G/TFA, IA9-G/HCl and IA9-K scramble synthetic peptides recorded in DMPG/DMPC 1:3 at a 0° angle. Peptides were dissolved in $CHCl_3/CH_3OH$ (1:1, v/v) at a final concentration of 2.44 mg/mL and mixed with phospholipids (DMPG/DMPC 1:3) yielding a P/L ratio of 1:15 (1A-2A) and a P/L ratio of 1:60 (1B-2B). Spectra were collected in the 180–260 nm range express in terms of mdeg and normalized as G-value.

The peptides IA9-G (TFA/HCl) and IA9-K scramble were also analyzed by OCD. Sample preparation and experimental conditions were identical to those described previously. As in earlier experiments, no differences were detected when spectra were acquired at 90° or from the back side of the sample, thereby excluding contributions from LD. As shown in **figure 17-1A** and **17-1B**, IA9-G peptides exhibited no evidence of preferred secondary structure, irrespective of the dilution or counterion used. This observation suggests that IA9-G predominantly adopts a parallel orientation relative to the plane of the lipid bilayer. In contrast, IA9-K scramble displayed a distinct spectral signature: at higher density (P/L 1:15), the CD spectrum was characterized by a pronounced positive band near 190 nm and an intense negative band around 210 nm. Upon dilution (P/L 1:60), the negative band markedly decreased in

intensity, accompanied by a broader and less defined maximum. These findings indicate that IA9-K scramble possesses an enhanced ability to interact and penetrate the lipid bilayer, apparently even more effectively than IA9-K/TFA, while adopting a β-sheet-like conformation. At lower peptide densities, the reduced signal intensity suggests a less embedded, more surface-associated orientation within the membrane. In this case as well, the CD spectra in **Figures 17-2A** and **17-2B** are additionally displayed in mdeg, exhibiting the same overall spectral features.

Finally, the influence of the counterion on the IA9-G peptides was also examined using the NMR-based approach, with the additional aim of assessing whether the substitution of lysine with glycine, and the resulting increase in overall hydrophobic character, affects the conformational behaviour of the peptide under these conditions. The experiments were conducted under the same conditions as previously described.

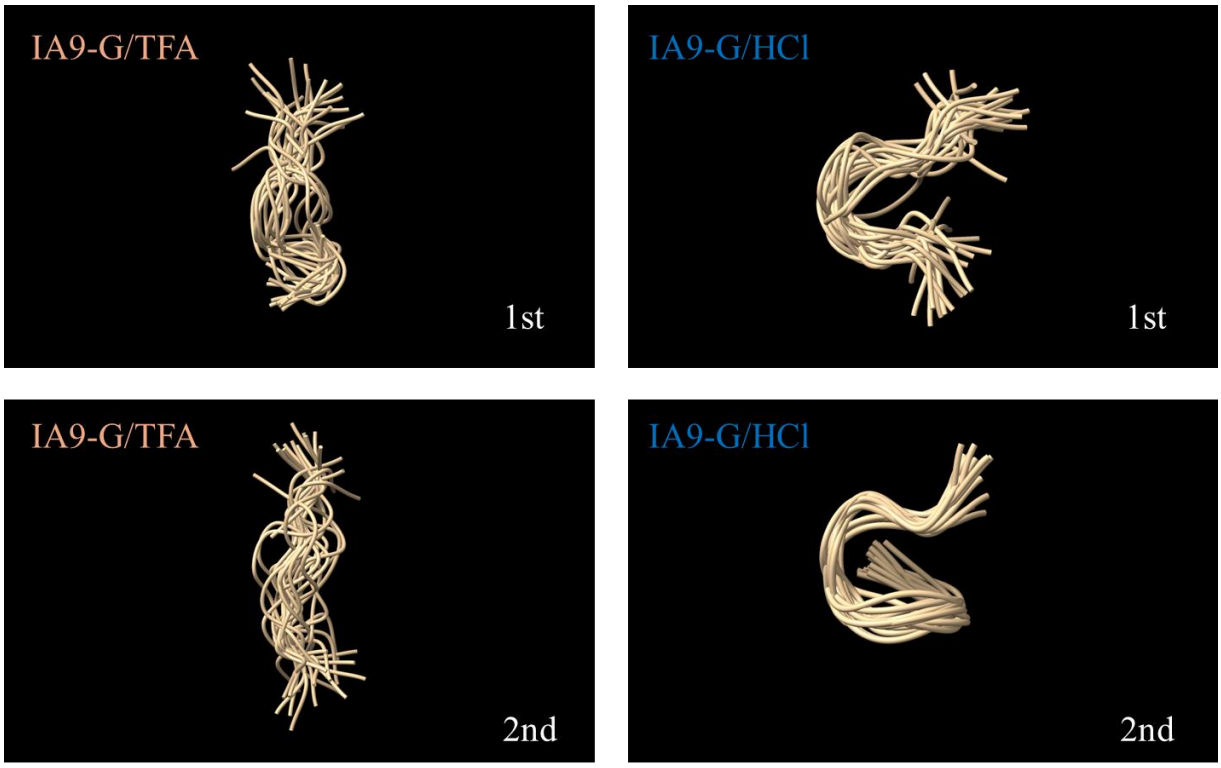

Figure 18. Molecular representations generated with ChimeraX 1.10 of the IA9-G/TFA and IA9-G/HCl peptide models obtained from NMRtist calculations in 100% DMSO. Two structural models (1st and 2nd) were generated, comprising ensembles of twenty conformers.

Comparison of the 3D models generated by NMRtist (**Figure 18**) revealed that, as had been observed for the IA9-K peptides, the presence of chloride ions markedly influenced the conformational landscape of IA9-G. Specifically, the chloride form exhibited a pronounced central folding, though slightly less defined than that of IA9-K. Notably, the IA9-G/TFA models had shown a higher degree of conformational heterogeneity, with conformers displaying reduced structural overlap, an indication of increased flexibility within the peptide ensemble. Furthermore, analysis of the 2D NMR spectra revealed, also in this case, that the cross-peak arising from the spatial proximity between the α-proton and one of the γ-methylene protons ($–CH_2$) of isoleucine 4 was markedly more intense in IA9-G/HCl, reflecting a closer spatial proximity in this region and corroborating the conformational differences observed in the 3D models (Appendix A).

Chapter 3

Comprehensive characterization of sulfolipids in the mouse brain

3.1 Optimization of lipid extraction for mouse brain tissue

In order to qualitatively characterize the sulfolipid families in mouse brain, total lipid extraction had been performed according to the Bligh and Dyer method [84]. The procedure had been applied to brains (n=2) of a 2–3-month-old female mouse with a wet weight of 421 ± 4 mg. In the original protocol described by Bligh and Dyer, tissue homogenization was carried out directly in a ternary mixture of chloroform ($CHCl_3$), methanol (CH_3OH), and water (H_2O) (1:2:0.8, v/v/v), followed by a single adjustment of solvent volumes to reach the final ratio of 2:2:1.8 required for phase separation. The protocol employed in this study introduced several modifications aimed at improving the lipid recovery and the representation of polar species. Modifications to the classical Bligh and Dyer workflow, including altered solvent ratios and the stepwise addition of $CHCl_3$ and H_2O to an initially CH_3OH-rich homogenate, have been reported to affect the efficiency of phase formation and the lipid recovery [85]. Accordingly, extraction started in an excess of methanol, with chloroform and water subsequently added in a gradual manner, allowing solvent proportions to be progressively adjusted until biphasic separation had been achieved (Section III, paragraph 5.9). These modifications allowed the recovery of a broader spectrum of lipid species and mitigated the potential underestimation of more hydrophilic molecular classes. The recovered organic phase ($CHCl_3$–CH_3OH) weighed 31.1 ± 2.1 mg and was then used for the subsequent high-resolution untargeted LC–MS/MS analysis (both ESI positive and negative mode) to characterize the lipid composition (Section III, paragraph 5.11).

3.1.1 Lipid profiling of brain sulfolipids

To evaluate the lipid content of the organic extract and to assess the efficiency of the extraction procedure, as well as to identify sulfolipid families, the raw LC–MS/MS data was first queried against the *LipidSearch* database. LipidSearch is a specialized software for LC–MS/MS lipidomics that identifies lipid species based on retention time, fragmentation patterns, and ion masses. Its database contains over 1.2 million lipid ions across multiple classes, enabling the detection of both high- and low-

abundance species with a variety of ion adducts (+H, −H, +Na, +CH_3CO). The results of this analysis are summarized in the **Table 2**.

Table 2 – Grade A lipid species identified in the brain extract using LipidSearch, with the lipid family, acyl chain composition, adduct type, and corresponding *m/z* values reported.

LIPID FAMILY	CHAIN	ADDUCT	*m/z*
Ceramides	d18:1/18:0	M-H	564.53
Ceramides	d18:2/18:0	M-H	562.52
Ceramides	d20:1/18:0	M-H	592.56
Ceramides	d18:1/16:0	M-H	536.50
Ceramides	d18:1/24:1	M-H	646.61
Ceramides	d18:1/22:0	M-H	620.59
Ceramides	d18:0/18:0	M-H	566.55
Ceramides	d18:2/20:0	M-H	590.55
Phosphatidylethanolamines	18:0/20:4	M-H	766.53
Phosphatidylethanolamines	18:1/20:4	M-H	764.52
Phosphatidylethanolamines	18:1/18:1	M-H	742.53
Phosphatidylethanolamines	18:0/18:1	M-H	744.55
Phosphatidylethanolamines	16:0/20:4	M-H	738.50
Lyso-phosphatidylethanolamines	18:0	M-H/M+H	480.30/482.32
Lyso-phosphatidylethanolamines	22:6	M-H/M+H	524.28/526.29
Lyso-phosphatidylethanolamines	18:1	M-H/M+H	478.29/480.30
Lyso-phosphatidylethanolamines	16:0	M-H/M+H	452.28/454.29
Lyso-phosphatidylethanolamines	20:4	M-H/M+H	500.28/502.29
Lyso-phosphatidylethanolamines	20:1	M-H	506.32

Lyso-phosphatidylethanolamines	22:4	M-H	528.30
Phosphatidylcholines	16:0/22:6	$M+Na^+$	828.55
Phosphatidylcholines	16:0/16:0	$M+Na^+$	756.55
Phosphatidylcholines	16:0/18:0	$M+Na^+$	784.58
Phosphatidylcholines	18:0/18:1	$M+Na^+$	810.60
Phosphatidylcholines	22:6/22:6	$M+Na^+$	900.55
Lyso-phosphatidylcholines	16:0	$M+CH_3COO^-$	554.34
Lyso-phosphatidylcholines	18:0	$M+CH_3COO^-$	582.37
Lyso-phosphatidylcholines	18:1	$M+CH_3COO^-$	580.36
Phosphatidylinositols	18:0/20:4	M-H	885.55
Phosphatidylinositols	16:0/20:4	M-H	857.51
Phosphatidylinositols	18:1/20:4	M-H	883.53
Phosphatidylinositols	18:0/22:6	M-H	909.54
Phosphatidylinositols	16:0/18:1	M-H	835.53
Phosphatidylinositols	18:1/18:1	M-H	861.55
Phosphatidylserines	18:1/18:1	M-H	786.53
Phosphatidylserines	22:6/22:6	M-H	878.50
Phosphatidylserines	18:1/20:1	M-H	814.56
Phosphatidylserines	18:0/20:4	M-H	810.53
Sulfo-quinovosyldiacylglycerols	18:0/18:0	M-H	849.58

LipidSearch classifies each lipid species according to a confidence grade A, B, or C, with grade A representing the most robust and reliable identifications. Accordingly, only grade A assignments were reported, ensuring unambiguous confirmation of both the lipid class and fatty acyl composition via MS/MS analysis. The lipidome was predominantly composed of ceramides and glycerophospholipids.

Within the glycerophospholipid subset, phosphatidylethanolamines, phosphatidylcholines (along with their lysophospholipid derivatives), phosphatidylinositols, and phosphatidylserines (including their lysophospholipid forms) were observed. *m/z*

LipidSearch-based strategy, which relies on information contained in existing databases, did not enable a comprehensive characterization of the sulfolipidome. Indeed, only a single set of data coherent with the sulfoquinovosyldiacylglycerol species with two stearic acids (SQDG18:0_18:0, 849.58 *m/z*, highlighted in red) was tentatively recognized by the software. This revealed an analytical bottleneck inherent to database-dependent approaches, since the strong reliance on previously characterized lipid profiles may lead to the under or misrepresentation of minor lipid classes, like for sulfolipids, thereby limiting their detection and characterization. Based on these limitations, an alternative strategy was adopted using the *MZmine* [86] platform. This software provides a comprehensive suite of tools for mass spectrometry data processing, including peak detection, deconvolution, alignment, and identification. MZmine also allows visualization of raw LC–MS/MS data as three-dimensional MS/MS scatter plots, where each detected ion is represented as a dot according to its retention time (x-axis), precursor ion *m/z* (y-axis), and precursor ion intensity (z-axis). **Figure 19** shows a two-dimensional section of the scatter plot, in which dots with more intense coloration represented precursor ions of higher intensity.

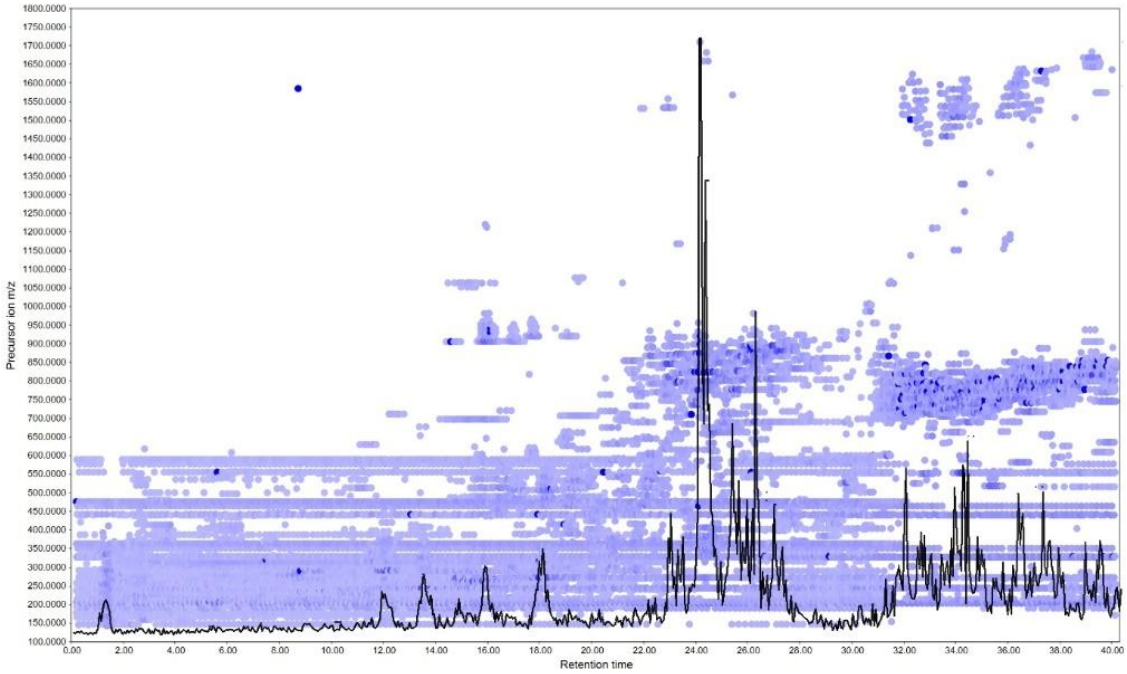

Figure 19 – **Two-dimensional MS/MS scatter plot of the organic mouse brain extract obtained from LC–MS/MS raw data and visualized using the "Number of best fragments" (95) filter**. Each dot represents a detected ion, with retention time on the x-axis, precursor *m/z* on the y-axis, and precursor ion intensity on the z-axis. The Total Ion Chromatogram (TIC) was overlaid to highlight the correspondence between global ion intensity and the spatial distribution of the most abundant precursor ions in the dataset.

Three distinct clusters of precursor ions were inferred alongside excluded species *m/z* corresponding to adducts, in-source fragments, and solvent-related species. A first group of relevant molecules comprised species with *m/z* range between 700-1000 and retention times between 20 and 26 minutes. A second cluster included ions with slightly lower *m/z* values and retention times of 30-40 minutes, while a third cluster represented *m/z* species around 1500-1700 *m/z*, with retention times spanning 32-40 minutes.

In addition to providing a global visualization of the raw data as a MS/MS scatter plot, it was possible to refine the search for specific precursor ions by applying filters based on diagnostic fragments [87]. Sulfate ($-OSO_3^-$) [88] or sulfonate groups ($-SO_3^-$) account for the most common forms of oxidized sulfur in lipids [89], making these moieties diagnostic fragments for targeted lipid identification. Both groups exhibit high stability under negative ESI conditions. Sulfated lipids generate the characteristic bisulfate fragment ion (*m/z* 96.958, HSO_4^-) [90], whereas sulfonate loss produce diagnostically bisulfite fragment ion (*m/z* 80.963, HSO_3^-) [91]. Accordingly, these two fragmentations were employed to filter the sulfolipid clusters described above.

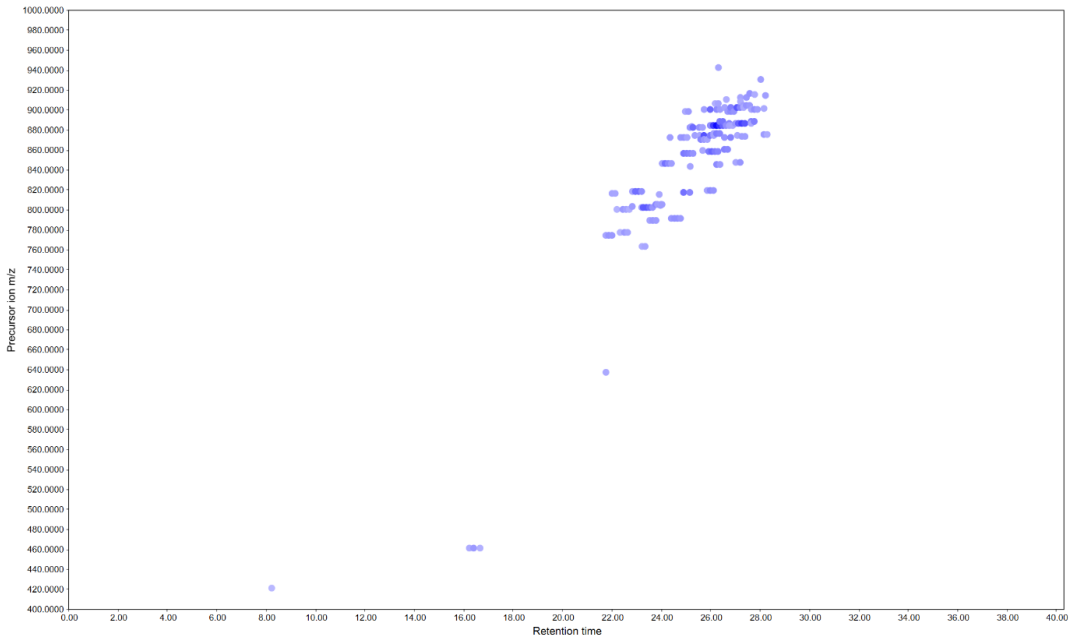

Figure 20 – Representative MS/MS scatter plot of the C/M mouse brain extract from the LC–MS/MS raw data, filtered for ions generating the diagnostic bisulfate fragment (*m/z* 96.958, HSO_4^-) and using the "Number of best fragments" (value 95) option. Each dot represents a detected precursor ion, with retention time on the x-axis, precursor *m/z* on the y-axis, and precursor ion intensity on the z-axis, highlighting the distribution of the most intense sulfur-containing lipids in the dataset.

After applying these diagnostic filters, no precursor ions generating the bisulfite ion were detected, providing robust evidence for the absence of sulfonated lipids in brain tissue (data not shown). In

contrast, a substantial number of sulfated species were identified on the basis the diagnostic bisulfate fragment (*m/z* 96.958, HSO_4^-) (**Figure 20**). Furthermore, "Number of best fragments" option (displaying the ions with the highest intensities from each scan) and the "Base peak percent" option (plotting ions above a set percentage of the base peak intensity) were applied under optimized conditions to obtain a comprehensive and inclusive output of the detected species. The MS/MS spectra of the ions included in the merged dataset (Appendix A) were further double-checked by manual inspection to generate a final list of products including three distinct families of sulfated lipids (detectable in ESI negative mode), in addition to sulfated cholesterol (*m/z* 465.304) characterized by absence of fragmentation due to the chemical stability of the polycyclic aliphatic core *m/z*(**Figure 21**). No additional sulfated sterols were identified.

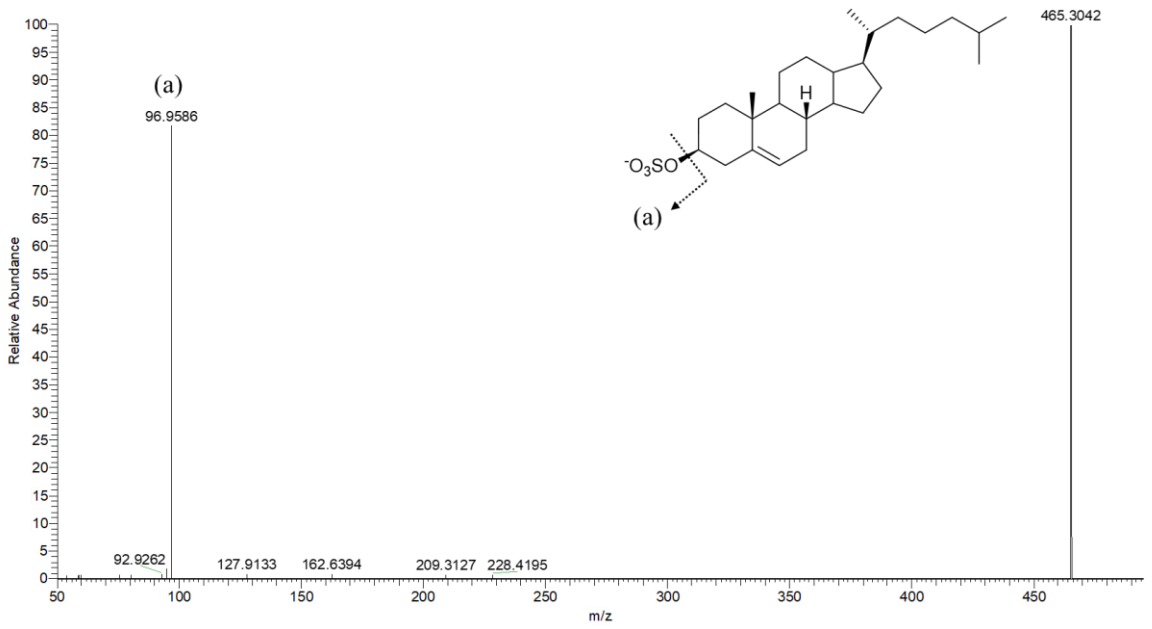

Figure 21 – MS/MS spectrum of sulfated cholesterol (*m/z* 465.304) acquired in negative electrospray ionization (ESI-), Higher-energy Collisional Dissociation (HCD) 35.0 eV. The spectrum shows the characteristic bisulfate fragment ion (*m/z* 96.958, HSO_4^-), corresponding to the loss of the sulfate group.

Among the sulfolipid classes, a prominent group corresponded to 3-O-sulfo-galactosyl ceramides, commonly referred to as sulfatides. As representative example, the MS/MS spectrum of the precursor ion at *m/z* 878.603 $[M–H]^-$ (**Figure 22**) displayed the characteristic bisulfate fragment at *m/z* 96.958 (f) together with the diagnostic ion at *m/z* 241.001 (e), which was unequivocally assigned to sulfated galactose on the basis of metabolic considerations [92]. This fragment most likely originated from the

cleavage of the anomeric C-O bond with concomitant loss of the ceramide moiety, followed by rearrangements leading to the formation of galactopyranose-3-sulfate isomers.

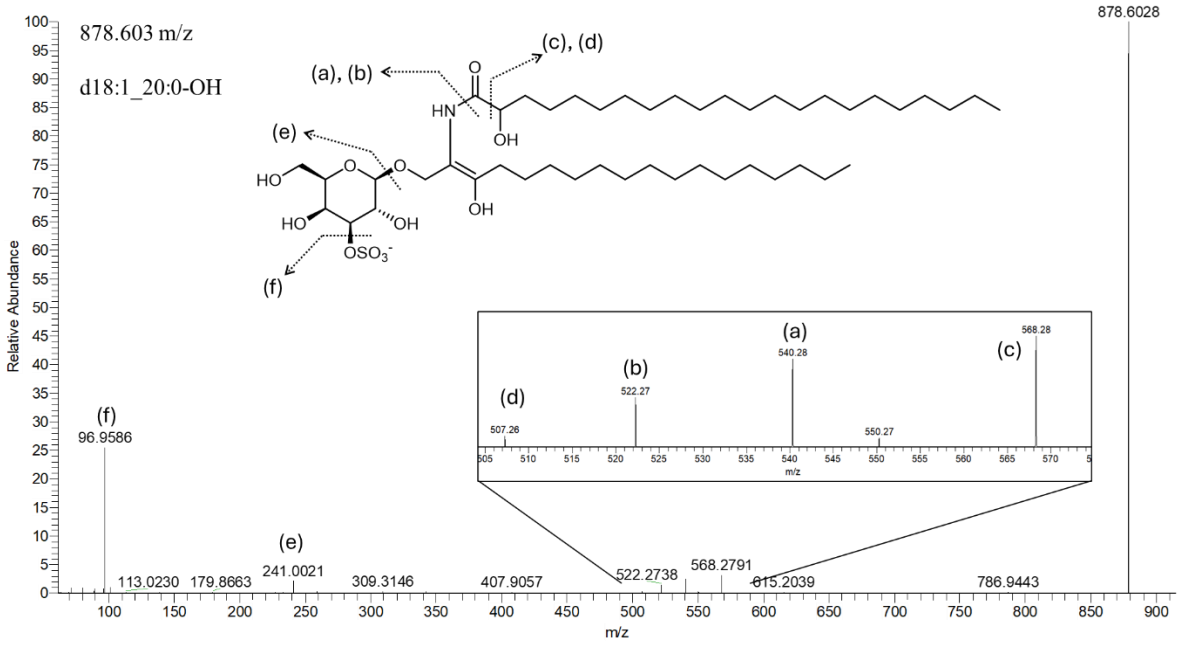

Figure 22 – MS/MS spectrum of sulfatide (*m/z* 878.603 [M–H]⁻) from mouse brain extract acquired in negative electrospray ionization (ESI–) using HCD at 35.0 eV. The spectrum displays the characteristic bisulfate fragment ion (*m/z* 96.958, HSO_4^-) and the diagnostic ion of sulfated galactose (*m/z* 241.001), along with a series of ceramide-derived fragments resulting from backbone cleavages and rearrangements typical of sulfatides containing α-hydroxy fatty acids.

In addition to these sugar-derived fragments, the spectrum displayed a series of ceramide-specific product ions at *m/z* 507.275 (d), 522.275 (b), 540.284 (a), and 568.571 (c), which reflected distinct backbone rearrangements associated with the presence of the α-hydroxyl group. In particular, the *m/z* 540 ion had arisen from selective cleavage of the C-C bond between the carbonyl carbon and the adjacent α-hydroxy carbon, a process that expelled CO together with the fatty acyl chain as an aldehyde. Elimination of water from this fragment subsequently generated the *m/z* 522 ion. Alternatively, direct aldehyde release from the same bond produced the *m/z* 568 ion, whose further fragmentation yielded the *m/z* 507 ion [93]. Within the sulfatide family, both α-hydroxylated and non-hydroxylated sulfatide species were detected. The absence of the electron-withdrawing hydroxyl group markedly reduced the formation of diagnostic fragments, rendering them fewer, less stable, and considerably more difficult to detect [94].

Table 3 reports the complete array of sulfatide species identified in this study, together with their characteristic diagnostic fragments, providing a comprehensive overview of the molecular diversity and fragmentation patterns that were observed.

Table 3 - Sulfatides identified in the C/M mouse brain extract by LC–MS/MS following MZmine deconvolution. For each species, the precursor *m/z*, the ceramide composition (type), and the corresponding diagnostic fragment ions are reported.

m/z	TYPE	MS/MS (fragments *m/z*)
778.5155	d18:1/16:0	96.9588 – 241.0016
804.5316	d18:1/18:1	96.9588 – 241.0024
806.5470	d18:1/18:0	96.9587 – 241.0024
820.5254	d18:2/18:0-OH	96.9587 – 241.0017 – 538.2705 – 566.2695
822.5419	d18:1/18:0-OH	96.9588 – 241.0022 – 507.2619 – 522.2742 – 540.2853 – 586.2810
850.5730	d18:1/20:0-OH	96.9588 – 241.0019 – 507.2609 – 522.2748 – 540.2839 – 568.2794
860.5942	d18:1/22:1	96.9588 – 241.0025
878.6042	d18:1/22:0-OH	96.958 – 241.0025 – 507.2596 – 522.2763 – 540.2875 – 568.2792
880.6169	d18:0/22-OH	96.9587 – 241.0023 – 524.2814 – 542.2980 – 570.2924
888.6251	d18:1/24:1	96.9587 – 241.0021
890.6403	d18:1/24:0	96.9587 – 241.0021
892.6205	d18:1/23:0-OH	96.9587 – 241.0018 – 507.2637 – 522.2756 – 540.2856 – 568.2803
894.6364	d18:0/23-OH	96.9587 – 241.0018 – 507.2637 – 522.2756 – 540.2856 – 568.2803
902.6033	d18:1/24:2-OH d18:2/24:1-OH	96.9586 – 241.0020 – 522.2744 – 540.2861 – 568.2766 96.9586 – 241.0020 – 538.2861 – 566.2766
904.6196	d18:1/24:1-OH	96.9587 – 241.0018 – 507.2631 – 522.2744 – 540.2862 – 568.2819
906.6356	d18:1/24:0-OH	96.9587 – 241.0022 – 507.2625 – 522.2782 – 540.2829 – 568.2819
908.6510	d18:0/24:0-OH	96.9588 – 241.0023 – 524.2883 – 542.3002 – 570.2715
920.6507	d18:1/25:0-OH	96.9587 – 241.0038 –522.2715 - 540.2853 – 568.2811
932.6504	d18:1/26:1-OH	96.9587 – 241.0020 – 540.2856 – 568.2781

The other two sulfolipid classes that had been identified were similarly marked by the presence of the diagnostic fragments at *m/z* 96.958 and 241.001, indicating that they also comprised sulfated hexose-

based lipids. One of these classes, however, was distinguished by a consistently abundant fragment at *m/z* 539.289, which appeared in all MS/MS spectra where this lipid type had been observed. **Figure 23** illustrates the case of the precursor ion at *m/z* 821.5449 $[M-H]^-$, which exhibited all three fragments above mentioned. Subtraction of the 539 Da fragment (a) from the precursor ion yielded a mass difference of 282 Da, consistent with an 18:1 fatty acid. The spectrum also contained a low-intensity ion at *m/z* 281.248 (a), plausibly corresponding to the deprotonated form of this fatty acid.

Taken together, these observations suggested that the *m/z* 539 fragment (a) represented a stable moiety retaining the sulfated hexose while lacking one acyl chain. A lipid class displaying this characteristic fragmentation pattern corresponds to 3-O-sulfo-galactosyl alkylacyl glycerols, commonly known as "seminolipids," which have been primarily studied in the context of testicular tissues [95]. Their structure is based on a glycerol backbone in the *sn*-configuration, with an ether-linked alkyl chain at the *sn*-1 position, an ester-linked fatty acyl chain at the sn-2 position, and a carbohydrate moiety at the *sn*-3 position. As in sulfatides, this sugar is a β-D-galactose residue specifically sulfated at the 3′-hydroxyl group [96]. The generation of the *m/z* 539 fragment strictly required the *sn*-1 ether-linked alkyl chain to be saturated and composed of 16 carbons (16:0). Strikingly, the spectrum also displayed a fragment at *m/z* 565.307 (a′), corresponding to the isomeric variant carrying a 18:1 alkyl chain. In this form, the molecule consequently lost a 16:0 acyl chain, producing a fragment at *m/z* 255.2330 (a'). In contrast, the fragments at *m/z* 299.0435 (a)/(a') + (b) and 315.0388 (a)/(a') + (e) were generated via concomitant loss the acyl chain and cleavage of the glycerol C–O bond. These rearrangements led to formation of stable ions, with the *m/z* 315 fragment presumably retaining the ether oxygen. Collectively, these observations indicate that the fragment ions arose from backbone rearrangements characteristic of alkylacyl glycerols.

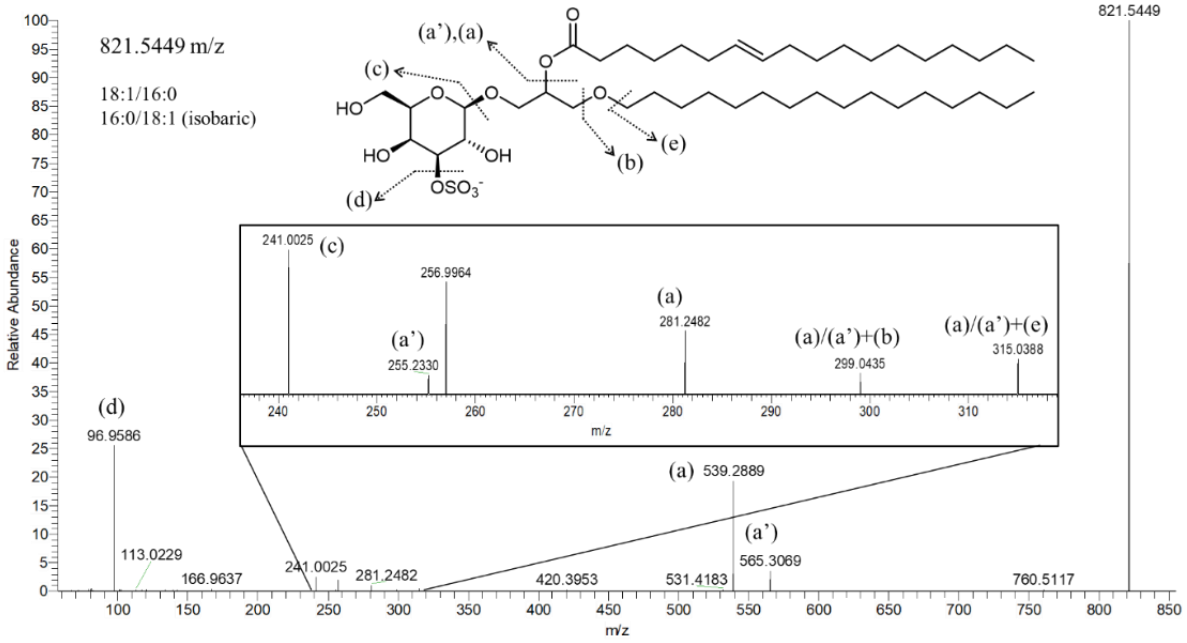

Figure 23 - MS/MS spectrum of the seminolipid (*m/z* 821.5449 [M–H]⁻) from the C/M mouse brain, acquired in negative electrospray ionization (ESI–) using HCD at 35.0 eV. The spectrum displays the characteristic bisulfate fragment ion (*m/z* 96.958, HSO_4^-) and the diagnostic ion of sulfated galactose (*m/z* 241.001), along with a prominent fragment at *m/z* 539.289, corresponding to the loss of the sn-2 acyl chain. Additional fragment ions at *m/z* 255.2330, 299.0435, and 315.0388 arise from backbone rearrangements involving the loss of both acyl and alkyl chains, with the *m/z* 315 fragment likely retaining the ether oxygen.

Full seminolipids pool characterization was supported using direct-infusion MS/MS spectra, building on the species list generated by MZmine and analyzed in a silica gel-purified fraction following anion-exchange enrichment, as will be shown later (paragraph 3.3). The last sulfolipid family identified was characterized by the presence of two acyl chains attached to the glycerol backbone, as unequivocally confirmed by the intense signals of the corresponding deacylated fragments (**Figure 24**). These lipids were assigned to the 3-O-sulfo-galactosyl diacylglycerols (SGDGs) [97]. For the precursor ion at *m/z* 781.475, fragment ions at *m/z* 525.237 (b) and 553.270 (a) corresponded to the loss of 16:0 and 14:0 acyl chains, respectively. The spectrum also displayed the fragment at *m/z* 299 (a) + (b), previously described, along with the ion at *m/z* 227 (a), resulting from the loss of the 14:0 chain.

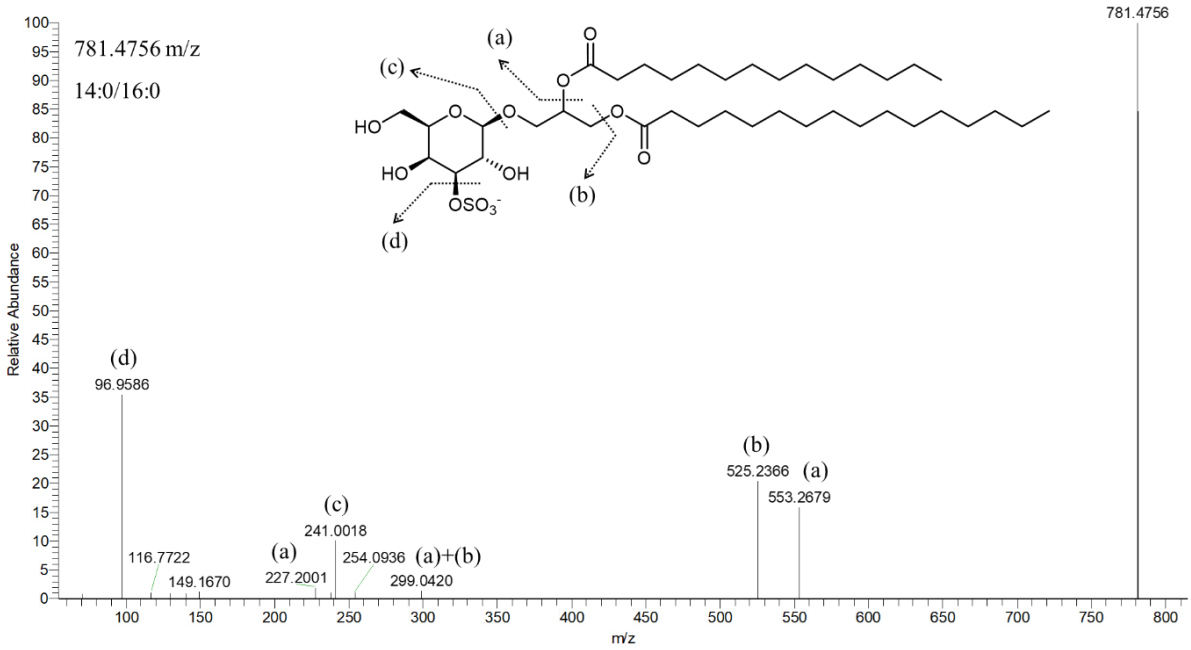

Figure 24 – MS/MS spectrum of the 3-O-sulfo-galactosyl diacylglycerol (SGDG, *m/z* 781.475 [M–H]⁻) from the C/M mouse brain, acquired in negative electrospray ionization (ESI–) using HCD at 35.0 eV. The spectrum displays the characteristic bisulfate fragment ion (*m/z* 96.958, HSO_4^-) and the diagnostic ion of sulfated galactose (*m/z* 241.001), along with fragment ions at *m/z* 525.237 and 553.270, corresponding to the loss of the 16:0 and 14:0 acyl chains, respectively. Additional fragments at *m/z* 299 and 227 arise from backbone rearrangements involving acyl chain losses, collectively defining the characteristic fragmentation pattern of this lipid class.

Unambiguous identification of all putative SGDG species listed by MZmine proved challenging, as the MS/MS spectra often contained fragments arising from contaminating phospholipids, which are highly abundant in brain tissue [98]. For example, as shown in **Figure 25**, the spectrum of the precursor ion at *m/z* 863.540, potentially corresponding to a SGDG composed of 16:0 and 20:1 acyl chains (indicated by fragments at *m/z* 553.270 and 579.285, respectively), also displayed the *m/z* 152.994 ion, a hallmark fragment characteristic (highlighted in red) of glicerophospholipids [99].

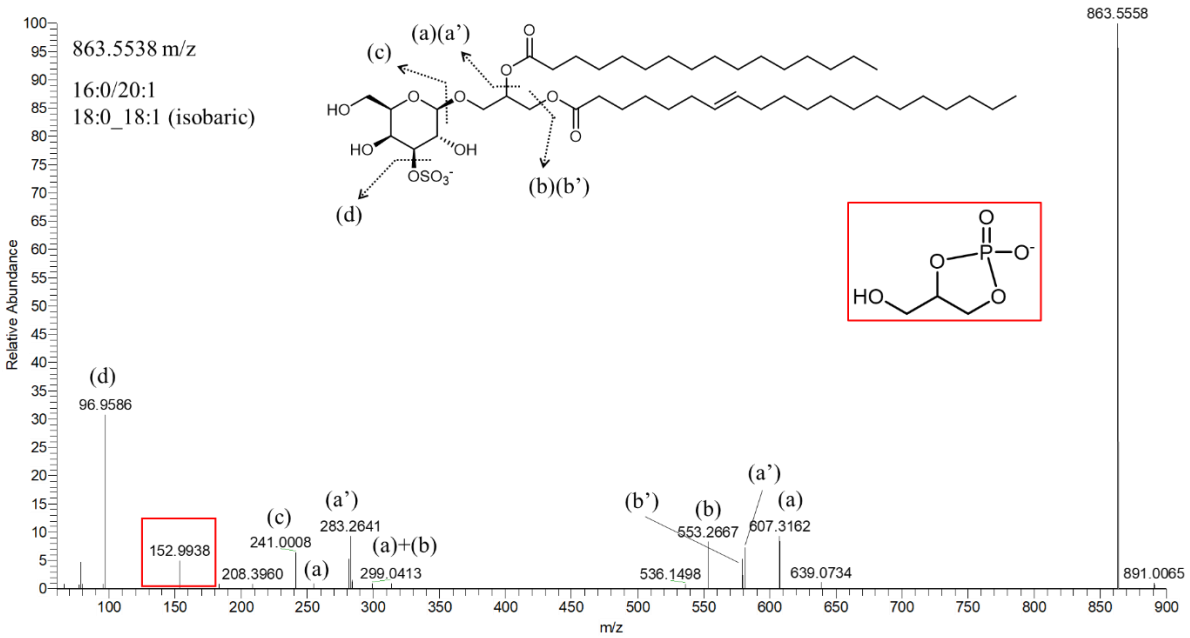

Figure 25 - MS/MS spectrum of the putative SGDG (*m/z* 863.540 [M–H]⁻) from the C/M mouse brain, acquired in negative electrospray ionization (ESI–) using HCD at 35.0 eV. The spectrum shows M-acyl fragment ions at *m/z* 553.270 and 579.285, corresponding to the sequential loss of 16:0 and 20:1 fatty acyl chains, supporting the SGDG assignment. An additional fragment at *m/z* 152.994, highlighted in red, originates from glycerophospholipid contaminants, which are prevalent in brain tissue.

Applying a diagnostic filter for the *m/z* 152.994 ion, in analogy with the *m/z* 96.958 filter, yielded the scatter plot shown in **Figure 26**. Despite its relatively low intensity, multiple lipids were detected with

retention times coinciding with those observed for sulfated species (20–30 min). This may explain the occurrence of glycerophospholipid fragment signatures detected in the MS/MS spectra of SGDGs.

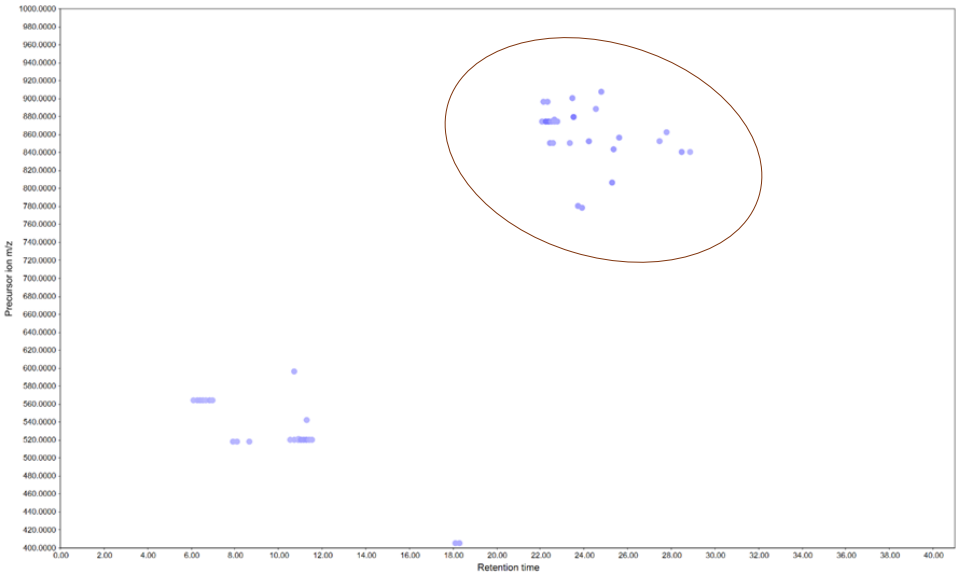

Figure 26 - Representative MS/MS scatter plot of the C/M mouse brain extract from the LC–MS/MS raw data, filtered for ions generating the fragment at *m/z* 152.994 and using the "Number of best fragments" (value 95) option. Each dot represents a detected precursor ion, with retention time on the x-axis, precursor *m/z* on the y-axis, and precursor ion intensity on the z-axis, highlighting (brown line) the distribution of ions associated with glycerophospholipid "contaminants".

3.2 Anionic lipid enrichment step to improve SGDGs characterization

A targeted enrichment was carried out using solid-phase extraction (SPE) on an $–NH_2$ functionalized resin, where anion-exchange chromatography selectively removed neutral and less polar lipids while retaining anionic species. This approach, exploiting the negative charge of sulfate groups, enabled efficient enrichment of sulfolipids [100] yielding cleaner spectra and improved detection sensitivity.

A suitable amount of C/M extract, corresponding to the resin loading capacity (6 mL of solvent per 500 mg of $–NH_2$ resin), was dissolved in $CHCl_3/CH_3OH$ (9:1) and loaded onto the $–NH_2$ resin. The column was then eluted sequentially with four solvent mixtures of increasing polarity (Section III, paragraph 5.10). The procedure employs sequential mixtures of $CHCl_3/CH_3OH$ 9:1, 8:2, and 75:25 to progressively remove neutral and zwitterionic lipids, thereby simplifying the sample matrix. Subsequently, an elution with $CHCl_3/CH_3OH$ 8:2 containing 100 mM $CH_3COO^-NH_4^+$ and 2% of NH_3 establishes ion-exchange conditions that favour the displacement of anionic species. Ammonia protonates the $–NH_2$ groups on the resin, while acetate ions mediate anion-exchange interactions, facilitating the selective release of negatively charged lipids. The entire developed procedure is showed in **Figure 27**. To assess lipid

composition and test enrichment efficiency evaluate the impact of fractionation, the enriched fractions were subjected to high-resolution untargeted LC–MS/MS, with the same chromatographic conditions applied to the total brain extract.

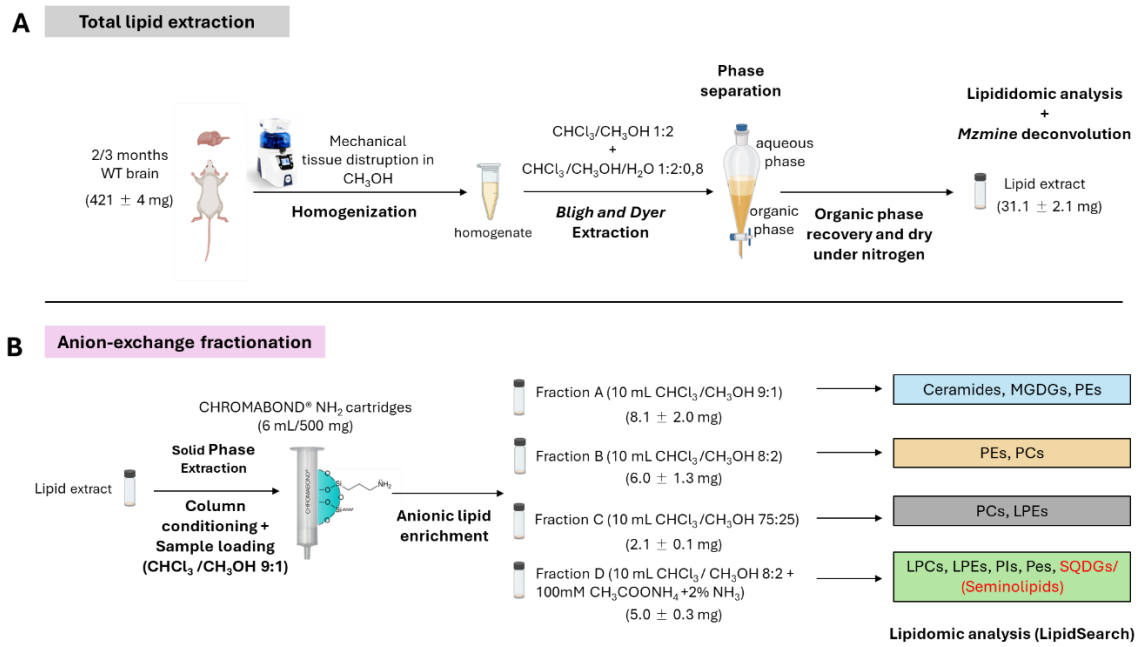

Figure 27 - Workflow for lipid extraction and anionic fractionation from mouse brains. (A) Lipid extracts were obtained from mouse brains following the Bligh and Dyer protocol. Brain homogenates were obtained in excess methanol, followed by chloroform ($CHCl_3$)-methanol (CH_3OH) extraction with the indicated solvent ratios. The organic phase was collected, dried under nitrogen, and analyzed by LC–MS/MS. Lipidomic data were processed using LipidSearch and deconvoluted with MZmine. (B) Anionic lipid enrichment was performed using an aminopropyl (-NH_2) resin. Four fractions were eluted with the solvents indicated in the scheme, dried under nitrogen, and subjected to lipidomic analysis with LipidSearch.

3.2.1 Lipidomic profiling of anionic lipids enrichment

To assess whether the anion-exchange procedure efficiently removed neutral and zwitterionic lipids, A the chromatographic lipid fractions were analyzed by using LipidSearch, according to the procedure applied to the $CHCl_3$/CH_3OH raw extract. While LipidSearch exhibited limited capacity for identifying sulfolipid families, it nonetheless proved to be valuable for tracking the distribution of major lipid classes across the different fractions (**Tables 4-7**).

The composition of fraction A ($CHCl_3$/CH_3OH 9:1, **Table 4**) is consistent with the expected behaviour of the lipids under these conditions. It was predominantly composed of ceramides, monogalactosyldiacylglycerols (MGDGs), and phosphatidylethanolamines (PEs). Ceramides and MGDGs are neutral, showing virtually no interaction with the -NH_2 resin, while PE are zwitterionic and

interact only weakly. Notably, the fractionation enabled the detection of MGDG, a class not observed in the unfractionated extract.

Table 4 - Grade A lipid species identified in the anionic exchange fraction A ($CHCl_3/CH_3OH$ 9:1) using LipidSearch, with the lipid family, acyl chain composition, adduct type, and corresponding *m/z* values reported.

LIPID FAMILY	CHAIN	ADDUCT	*m/z*
Ceramides	d18:1/18:0	M-H	564.54
Ceramides	d18:2/18:0	M-H	562.52
Ceramides	d20:1/18:0	M-H	592.57
Ceramides	d18:1/24:1	M-H	646.61
Ceramides	d18:1/16:0	M-H	536.50
Ceramides	d18:1/22:0	M-H	620.59
Ceramides	d18:2/20:0	M-H	590.55
Ceramides	d18:0/18:0	M-H	566.55
Ceramides	d18:1/21:0	M-H	606.58
Phosphatidylethanolamines	16:0/20:4	M-H	738.52
Phosphatidylethanolamines	18:1/18:1	M-H	742.53
Phosphatidylethanolamines	18:0/18:1	M-H	744.55
Phosphatidylethanolamines	18:1/20:4	M-H	764.52
Phosphatidylethanolamines	18:0/20:4	M-H	766.53
Monogalactosyldiacylglycerols	16:0/18:0	$M+Na^+$	781.58
Monogalactosyldiacylglycerols	16:0/16:0	$M+Na^+$	753.55
Monogalactosyldiacylglycerols	16:0/18:1	$M+Na^+$	779.56
Monogalactosyldiacylglycerols	14:0/16:0	$M+Na^+$	725.52
Monogalactosyldiacylglycerols	16:0/20:1	$M+Na^+$	807.60

Monogalactosyldiacylglycerols	16:0/20:0	$M+Na^+$	809.61
Monogalactosyldiacylglycerols	14:0/18:1	$M+Na^+$	751.533
Monogalactosyldiacylglycerols	18:1/18:1	$M+Na^+$	805.58
Monogalactosyldiacylglycerols	18:0/18:1	$M+Na^+$	807.60
Monogalactosyldiacylglycerols	14:0/14:0	$M+Na^+$	697.49

Fraction B ($CHCl_3/CH_3OH$ 8:2, **Table 5**) consisted mainly of PEs, as in fraction A, and included the first detection of phosphatidylcholines (PCs). Both lipid classes are zwitterionic. Due to their high abundance, PEs tended to span multiple fractions under similar elution conditions, continuing to elute in fraction B, while PCs appeared under these slightly more polar conditions.

Table 5 - Grade A lipid species identified in the anionic exchange fraction B ($CHCl_3/CH_3OH$ 8:2) using LipidSearch, with the lipid family, acyl chain composition, adduct type, and corresponding *m/z* values reported.

LIPID FAMILY	CHAIN	ADDUCT	*m/z*
Phosphatidylcholines	16:0/18:1	$M+Na^+$	782.570
Phosphatidylcholines	16:0/22:6	$M+Na^+$	828.554
Phosphatidylcholines	16:0/16:0	$M+Na^+$	756.555
Phosphatidylcholines	16:0/20:4	$M+Na^+$	804.554
Phosphatidylcholines	22:6/22:6	$M+Na^+$	900.554
Phosphatidylcholines	18:1/18:1	$M+Na^+$	808.586
Phosphatidylethanolamines	16:0/22:6	M-H	762.508
Phosphatidylethanolamines	18:0/18:1	M-H	744.555
Phosphatidylethanolamines	16:0/18:1	M-H	716.524
Phosphatidylethanolamines	18:1/22:6	M-H	788.524
Phosphatidylethanolamines	18:1/20:4	M-H	764.524

Phosphatidylethanolamines	16:1/18:1	M-H	714.508
Phosphatidylethanolamines	18:1/18:2	M-H	740.525

Fraction C ($CHCl_3/CH_3OH$ 75:25, **Table 6**) was dominated by lysophosphatidylethanolamines (LPEs) together with a cohort of PCs. As observed for PEs, PCs were recovered across multiple fractions, likely reflecting their high abundance. LPEs, which correspond to PEs lacking one acyl chain on the glycerol backbone, are relatively more polar species. Their elution under these more polar conditions therefore aligns with their structural properties.

Table 6- Grade A lipid species identified in the anionic exchange fraction C ($CHCl_3/CH_3OH$ 75:25) using LipidSearch, with the lipid family, acyl chain composition, adduct type, and corresponding *m/z* values reported.

LIPID FAMILY	CHAIN	ADDUCT	*m/z*
Phosphatidylcholines	16:0/20:4	$M+Na^+$	804.554
Phosphatidylcholines	14:0/16:0	$M+Na^+$	728.522
Phosphatidylcholines	16:0/16:1	$M+Na^+$	754.538
Phosphatidylcholines	16:0/18:2	$M+Na^+$	780.555
Phosphatidylcholines	16:0/22:6	$M+Na^+$	828.554
Phosphatidylcholines	16:0/16:0	$M+Na^+$	756.554
Lyso-phosphatidylethanolamines	18:0	M-H	480.309
Lyso-phosphatidylethanolamines	22:6	M-H	524.278
Lyso-phosphatidylethanolamines	18:1	M-H	478.293
Lyso-phosphatidylethanolamines	16:0	M-H	452.278

Fraction D ($CHCl_3/CH_3OH$ 8:2 + CH_3COONH_4 + 2% NH_3; **Table 7**) was enriched in anionic lipids, reflecting the effectiveness of the targeted elution strategy. Anionic phospholipids, including phosphatidylinositols (PIs) and phosphatidylserines (PSs), were selectively retained and subsequently released, confirming the ability of the -NH_2 resin to efficiently isolate negatively charged species. The PIs and PSs molecular species detected in this fraction exceeded that observed in the extract, further evidencing the occurrence of lipid enrichment.

Table 7 - Grade A lipid species identified in the anionic exchange fraction D (C/M 8:2 + CH_3COONH_4 + 2% NH_3) using LipidSearch, with the lipid family, acyl chain composition, adduct type, and corresponding *m/z* values reported.

LIPID FAMILY	CHAIN	ADDUCT	*m/z*
Lyso-phosphatidylethanolamines	18:0	M-H	480.310
Lyso-phosphatidylethanolamines	18:1	M-H	478.294
Lyso-phosphatidylethanolamines	16:0	M-H	452.280
Lyso-phosphatidylcholines	16:0	$M+CH_3COO^-$	554.346
Lyso-phosphatidylcholines	18:0	$M+CH_3COO^-$	582.380
Lyso-phosphatidylcholines	18:1	$M+CH_3COO^-$	580.362
Phosphatidylinositols	18:0/20:4	M-H	885.550
Phosphatidylinositols	18:1/20:4	M-H	883.535
Phosphatidylinositols	16:0/20:4	M-H	857.519
Phosphatidylinositols	18:0/18:1	M-H	863.565
Phosphatidylinositols	16:0/22:6	M-H	881.519
Phosphatidylinositols	16:0/18:1	M-H	835.531
Phosphatidylinositols	18:0/22:6	M-H	909.550
Phosphatidylinositols	18:0/22:4	M-H	913.581
Phosphatidylinositols	18:0/20:3	M-H	887.566

Phosphatidylinositols	16:0/22:4	M-H	885.550
Phosphatidylinositols	18:1/18:1	M-H	861.550
Phosphatidylinositols	16:1/18:1	M-H	833.517
Phosphatidylserines	16:0/18:1	M-H	760.514
Phosphatidylserines	18:0/18:1	M-H	788.546
Phosphatidylserines	18:1/18:1	M-H	786.529
Phosphatidylserines	18:1/20:1	M-H	814.560
Phosphatidylserines	18:0/22:6	M-H	834.531
Phosphatidylserines	22:6/22:6	M-H	878.499
Sulfo-quinovosyldiacylglycerols	16:0/16:0	M-H	793.515
Sulfo-quinovosyldiacylglycerols	18:0/18:0	M-H	849.578

Two ions at *m/z* 849.58 (also present in the raw extract) and *m/z* 793.52 were initially annotated as SQDGs. However, following deconvolution and re-assignment by MZmine, these ions can now be confidently attributed to seminolipids (specifically 16:1/16:0 and 20:1/16:0).

3.2.2 Comparative analysis of brain extract and enriched fractions

In addition to LipidSearch, the efficacy of anionic lipid enrichment in fraction D, obtained via anion-exchange chromatography, was further investigated by MZmine filtering, employing the same workflow previously applied to the C/M extract. No precursor ions generating the bisulfite fragment (*m/z* 80.963, HSO_3^-) were observed in fraction D, consistent with prior observations from the C/M extract (data not shown). Instead, as shown in **Figure 28**, comparison of the MZmine-derived scatter plots for the C/M extract and fraction D revealed an overlapping profile for sulfated molecules.

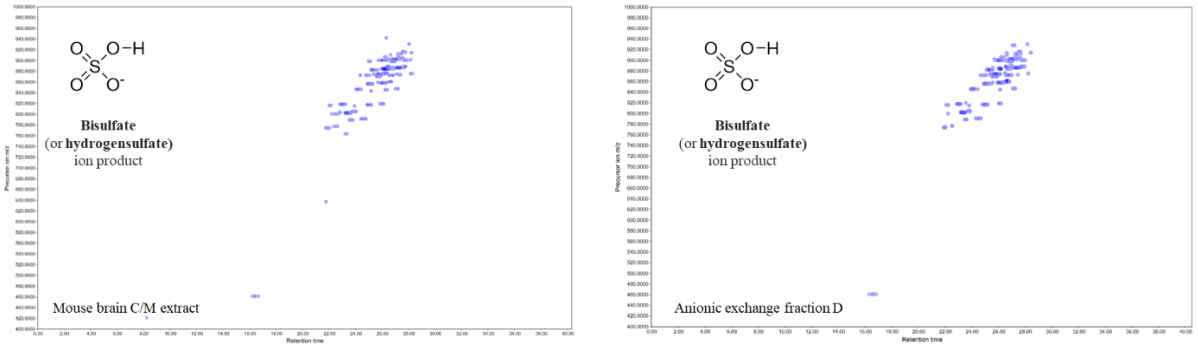

Figure 28 - Comparison of MS/MS scatter plots between the C/M mouse brain extract and fraction D, generated from LC–MS/MS raw data and filtered for ions producing the diagnostic bisulfate fragment (*m/z* 96.958, HSO_4^-) with the "Number of best fragments" set to 95. Each point represents a detected precursor ion, with retention time on the x-axis, precursor *m/z* on the y-axis, and ion intensity on the z-axis.

3.3 Separation of SGDGs from glicerophospholids via silica gel chromatography

Anion-exchange chromatography effectively removed most neutral and weakly interacting lipids, thereby reducing background complexity and facilitating downstream isolation of the target species. To achieve SGDG-containing fractions completely devoid of contaminating glycerophospholipids and suitable for detailed MS/MS structural characterization, fraction D was further purified by normal-phase silica gel chromatography. The fraction was purified by using a linear $CHCl_3/CH_3OH$ gradient (Section III, paragraph 5.13), from $CHCl_3/CH_3OH$ 95:5 to $CHCl_3/CH_3OH/H_2O$ 68:18:2, yielding 11 fractions. Efficient resolution was achieved using a polarity-decreasing gradient, optimized to distinguish sulfolipids from closely eluting glycerophospholipids. The 11 fractions (A–M) were analyzed by thin-layer chromatography (TLC) using $CHCl_3/CH_3OH$ 7:3 and $CHCl_3/CH_3OH/H_2O$ 65:25:4 as mobile phases. The chromatogram and the corresponding fraction weights are reported in **Figure 29**. Guided by the observed banding patterns, fractions from B to H and M were selected for direct-infusion analysis, acquiring full-scan MS spectra in negative ESI mode (Appendix A).

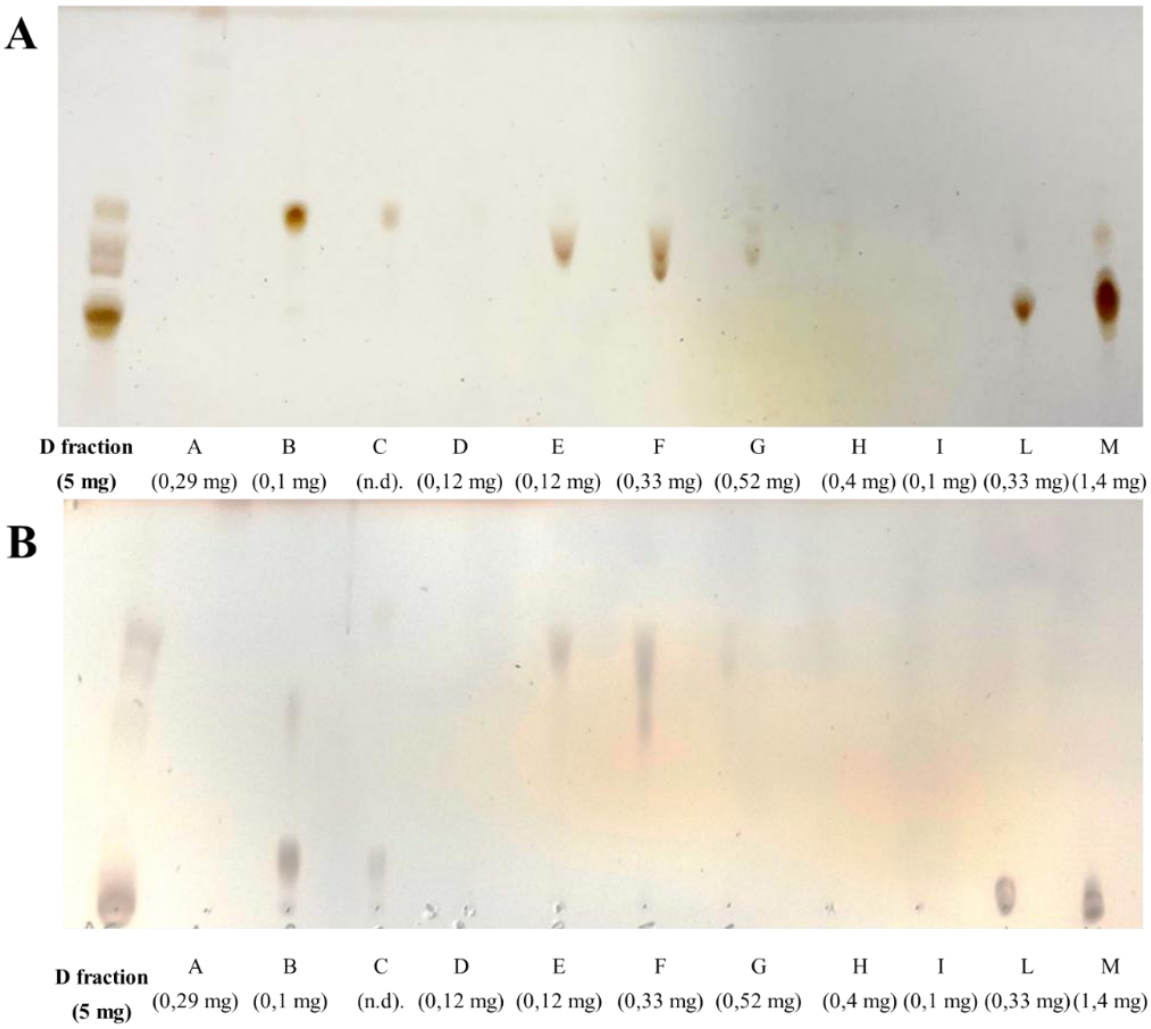

Figure 29 – TLC analysis of fractions A–M compared to anionic exchange D fraction, with weights indicated in parentheses. (A) Fractions were spotted onto silica gel plates and developed using $CHCl_3/CH_3OH$ 7:3 as the mobile phase. (B) Fractions were spotted onto silica gel plates and developed using $CHCl_3$/ CH_3OH /H_2O 65:25:4 as the mobile phase.) TLC eluted in $CHCl_3$: CH_3OH: H_2O (65:25:4; v/v/v). Spots were detected by $Ce(SO4)_2$.

Direct-infusion MS analysis of the collected fractions (Appendix A) revealed that fraction C (**Figure 30**) contained a distinct ion cluster attributable to a pool of SGDGs and seminolipids.

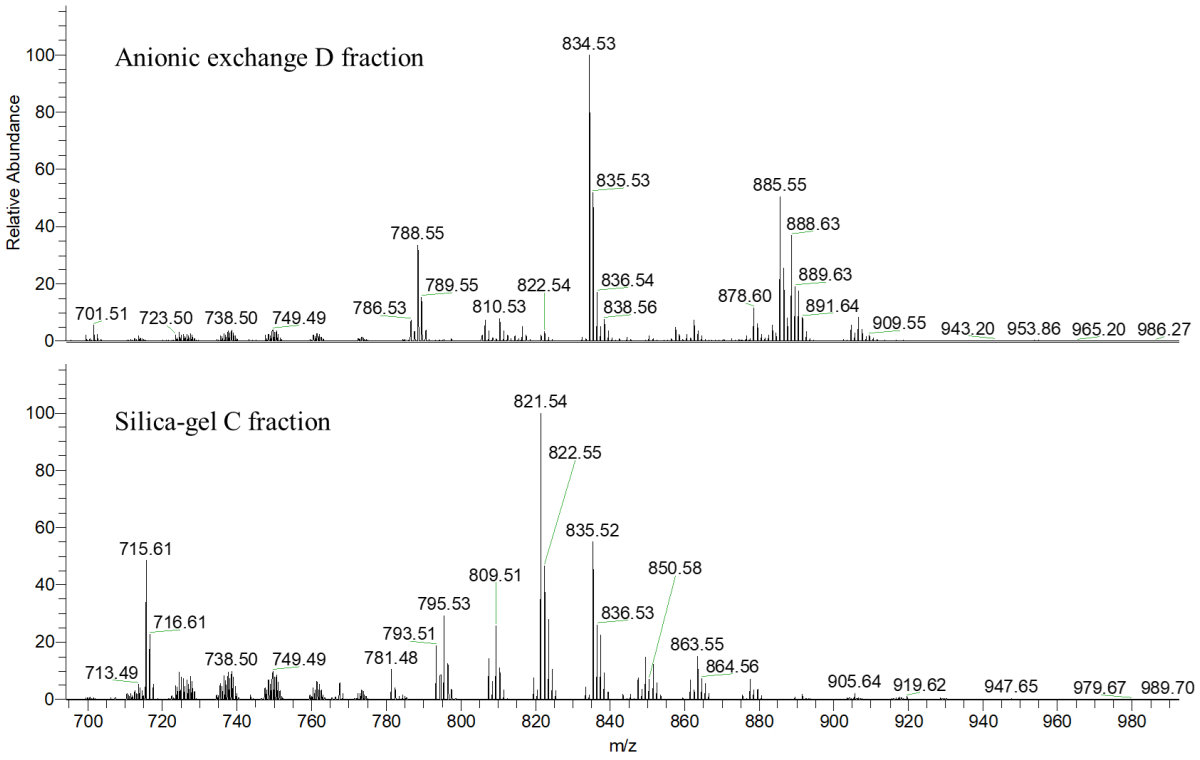

Figure 30 - Negative-mode Full MS comparison (zoomed between *m/z* 700–1000) of the starting anion-exchange fraction D and fraction C obtained after silica gel separation. Fraction D represents the initial lipid mixture, while fraction C shows the selectively enriched species after chromatographic separation.

Comparison with the anionic exchange D fraction unveiled a newly dominant peak at *m/z* 821.5, unambiguously assigned to a seminolipid species bearing 18:1/16:0 acyl chains, previously described in Section 3.1.1 and independently confirmed by direct-infusion analysis (Appendix A). In addition, prominent signals at *m/z* 835.5, 809.5, and 781.5 (along with their isotopic patterns) were consistent with candidate SGDG species. The MS/MS spectrum of the *m/z* 863.5 precursor ion (**Figure 25**; discussed in Section 3.1.1), isolated and subjected to stepwise fragmentation up to an HCD (Higher-energy Collisional Dissociation) energy of 40, revealed the full panel of diagnostic fragments characteristic of SGDGs, while lacking the *m/z* 152.99 ion (**Figure 31**). This absence excluded phospholipid contamination. Direct-infusion MS/MS analysis of all other putative SGDGs, as predicted by MZmine, further gave support to this evidence as no glycerophospholipid-derived fragments were detected (Appendix A). The seminolipids obtained from this pure fraction were also subjected to exhaustive structural characterization, enabling a complete annotation of their molecular species (Appendix A).

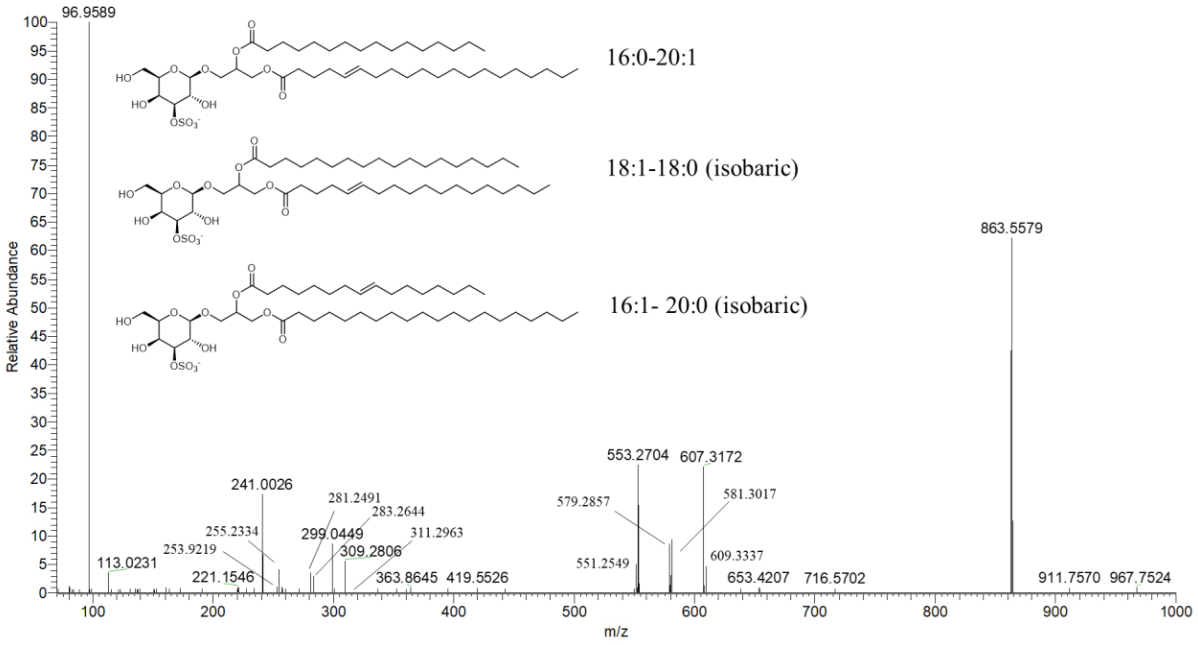

Figure 31 - MS/MS spectrum of the SGDG *m/z* 863.540 [M–H]⁻ from manual inspection of fraction C obtained via silica gel separation, acquired in negative electrospray ionization (ESI⁻) using HCD at 40.0 eV. The spectrum displays M–acyl fragment ions at *m/z* 553.270 and 579.285, corresponding to the sequential loss of 16:0 and 20:1 fatty acyl chains. Fragments from isobaric species further support the SGDG assignment.

Table 8 presents the full compendium of SGDG species identified throughout this approach, along with their corresponding diagnostic fragment ions, thus offering an exhaustive depiction of the molecular heterogeneity and fragmentation signatures characteristic of this lipid class. The MS/MS spectra for all sulfolipid species are provided in Appendix A.

Table 8 - SGDGs identified in the silica gel fraction following MZmine deconvolution. For each species, the table reports the precursor *m/z*, acyl chains composition (type), and the key diagnostic fragment ions.

m/z	TYPE	MS/MS (fragments *m/z*)
781.4788	14:0/16:0	96.9586 – 241.0022 – 255.2330 – 227.2014 – 299.0446 525.2379 – 553.2697
807.4952	16:0/16:1 14:0/18:1 (isobaric)	96.9588 – 241.0023 – 253.2175 – 299.0445 - 255.2333 – 551.2540 – 553.2693 96.9588 – 241.0023 – 227.2012 – 281.2488 –299.0445 - 525.2381 – 579.2851
809.5100	16:0/16:0 14:0/18:0 (isobaric)	96.9587 – 241.0022 – 255.2329 – 299.0447 – 553.2694 96.9587 – 241.0022 – 227.2014 – 281.2490 – 299.0447 – 525.2375 – 581.3010
835.5256	16:0/18:1 16:1/18:0 (isobaric) 14:0/20:1 (isobaric)	96.9587 – 241.0022 – 255.2229 – 281.2486 – 299.0442 – 553.2691 – 579.2847 96.9587 – 241.0022 – 253.2168 – 283.2644 – 551.2539 – 581.3005 96.9587 – 241.0022 – 525.2371 – 607.3167

837.5397	16:0/18:0 (isobaric)	96.9587 – 241.0024 – 255.233 - 283.2646 – 299.0447 – 553.2697 – 581.3019
861.5404	18:1/18:1 16:1/20:1 (isobaric)	96.9589 – 241.0025 – 281.2486 – 299.0442 – 579.2855 96.9589 – 241.0025 – 253.2176 – 551.2535 – 607.3179
863.5591	16:0/20:1 18:0/18:1 (isobaric) 16:1/20:0 (isobaric)	96.9589 – 241.0026 – 255.2334 – 299.0449 - 309.2806 – 553.2704 – 607.3172 96.9589 – 241.0026 – 281.2491 – 283.2644 – 299.0449 – 579.2857 – 581.3017 96.9589 – 241.0026 – 253.9219 – 299.0449 – 311.2963 – 551.2549 – 609.3337
865.6235	16:0/20:0	96.9588 – 241.0026 – 255.2336 – 299.0450 – 553.2700 – 609.3335

Table 9 reports the identified seminolipid species and their isobaric variants, including the corresponding diagnostic fragment ions and fatty acyl chain compositions. The MS/MS spectra for all species are provided in Appendix A.

Table 9 - Seminolipids identified in the *silica gel fraction* following MZmine deconvolution. For each species, the table reports the precursor *m/z*, the acyl chains composition (type), and the key diagnostic fragment ions.

m/z	TYPE	MS/MS (fragments *m/z*)
767.4983	14:0/16:0 16:0/14:0 (isobaric)	96.9586 - 241.0017 - 539.2894 96.9586 – 241.0017 – 511.2581
793.5140	16:1/16:0 16:0/16:1 (isobaric) 14:0/18:1 (isobaric) 18:1/14:0 (isobaric)	96.9586 – 241.0020 – 253.2171 – 299.0442 – 539.2894 96.9586 – 241.0020 – 255.2325 – 299.0442 - 537.2736 96.9586 – 241.0020 – 299.0442 – 565.3045 96.9586 – 241.0442 – 281.2475 – 299.0442 – 511.2578
795.5299	16:0/16:0 14:0/18:0 (isobaric) 18:0/14:0 (isobaric)	96.9586 – 241.0017 – 255.2325 – 299.0436 – 539.2892 96.9586 – 227.2010 – 241.0017 – 299.0436 – 567.3208 96.9586 – 241.0017 – 281.2482 – 299.0436 – 511.2581
821.5453	18:1/16:0 16:0/18:1 (isobaric) 20:1/14:0 (isobaric)	96.9586 – 241.0017 – 281.2481 – 299.0436 – 539.2891 95.9586 – 241.0017 – 255.2328 – 299.0436 – 565.3046 95.9586 – 241.0017 – 299.0436 – 511.2583
823.5602	18:0/16:0 16:0/18:0 (isobaric) 20:0/14:0 (isobaric)	96.9586 – 241.0018 – 283.2639 – 299.0440 – 539.2892 95.9586 – 241.0018 – 255.2323 – 299.0440 – 567.3210 95.9586 – 241.0018 – 299.0440 – 511.2577
849.5767	20:1/16:0 20:0/16:1 (isobaric) 18:0/18:1 (isobaric) 18:1/18:0 (isobaric) 22:1/14:0 (isobaric)	96.9586 – 241.0020 – 299.0438 – 539.2890 96.9586 – 241.0020 – 299.0438 – 537.2736 96.9586 – 241.0020 – 283.2638 – 299.0438 – 565.3077 96.9586 – 241.0020 – 281.2484 – 299.0438 – 567.3207 96.9586 – 241.0020 – 299.0438 – 511.2587

851.5920	20:0/16:0 18:0/18:0 (isobaric) 22:0/14:0 (isobaric)	96.9586 – 241.0016 – 299.0435 – 311.2948 – 539.2893 96.9586 – 241.0016 – 283.2640 – 299.0435 – 567.3218 96.9586 – 241.0016 – 299.0435 – 511.2581
877.6078	22:1/16:0 20:0/18:1 (isobaric)	96.9585 – 241.0014 – 539.2886 96.9585 – 241.0014 – 565.3049

Silica gel purification further enabled also the isolation of highly pure fractions of the sulfatide family. In fractions E–F–G, a dominant signal at *m/z* 888.6 (**Figure 32**) was detected and subjected to direct-infusion MS/MS, allowing assignment to sulfatide 18:1–24. Unlike α-hydroxylated counterparts, this species generated only weak diagnostic ions. Even under high-energy HCD (up to 45), however, the spectrum consistently displayed the canonical fragment at *m/z* 241.0, arising from dehydration of galactose-3-sulfate (259.0 *m/z*), together with its lactone counterpart at *m/z* 257.0. In addition, a hallmark ion at *m/z* 390.4 was observed, originating from C2-C3 sphingosine cleavage with the charge likely retained on the amide nitrogen. Moreover, the fragment ion at *m/z* 522, normally observable even at higher HCD energies in α-hydroxylated sulfatides, was detected under the present conditions (**Figure 33**). This finding highlighted the marked influence of the electron-withdrawing group on the fragmentation behaviour, especially when located along the amide-linked acyl chain. Several members of this lipid family, previously described in the literature, were also detected in the full MS spectra. Among these, the most prominent signals corresponded to molecule with molecular mass at *m/z* 806.5, 822.5, 878.6, and 906.6.

The chemical structure of these compounds was further corroborated after purification by detailed NMR analyses, which confirmed the proposed structural assignments and ensured the accuracy of the molecular identification (data not shown).

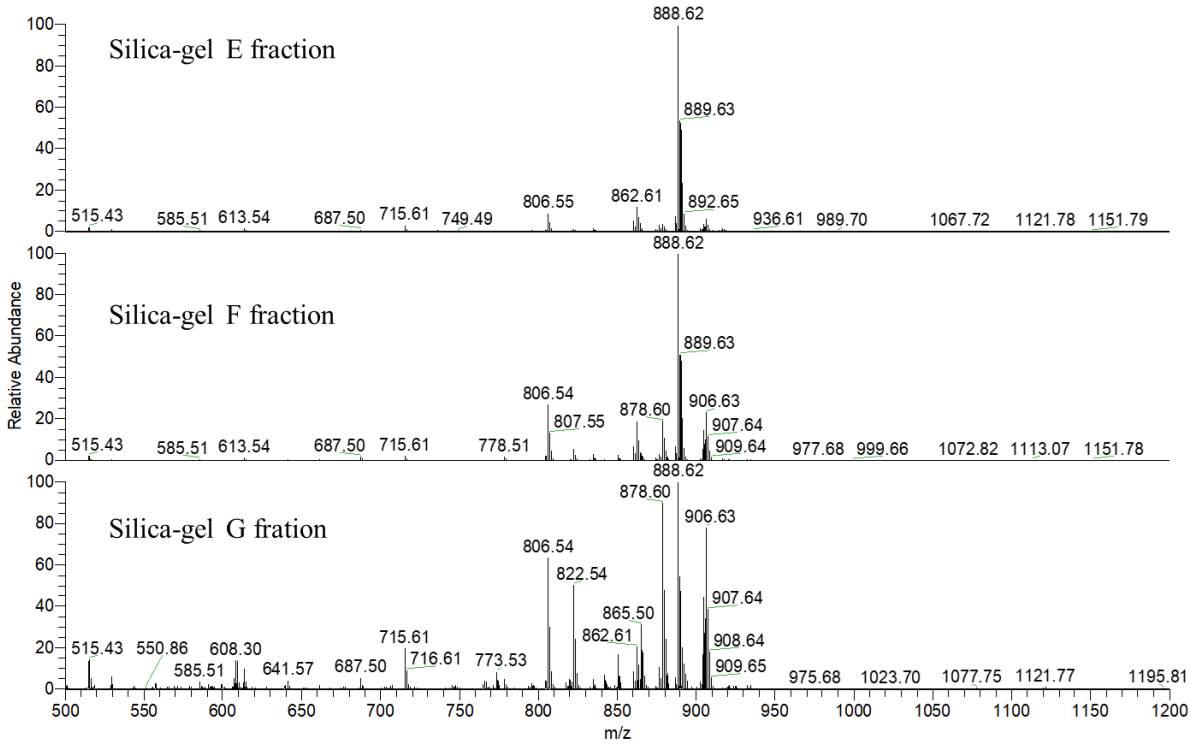

Figure 32 - Negative-mode Full MS comparison (zoomed between *m/z* 500–1200) of fractions E, F, and G obtained after silica gel separation, revealing the presence of prominent ions attributable to sulfatide species.

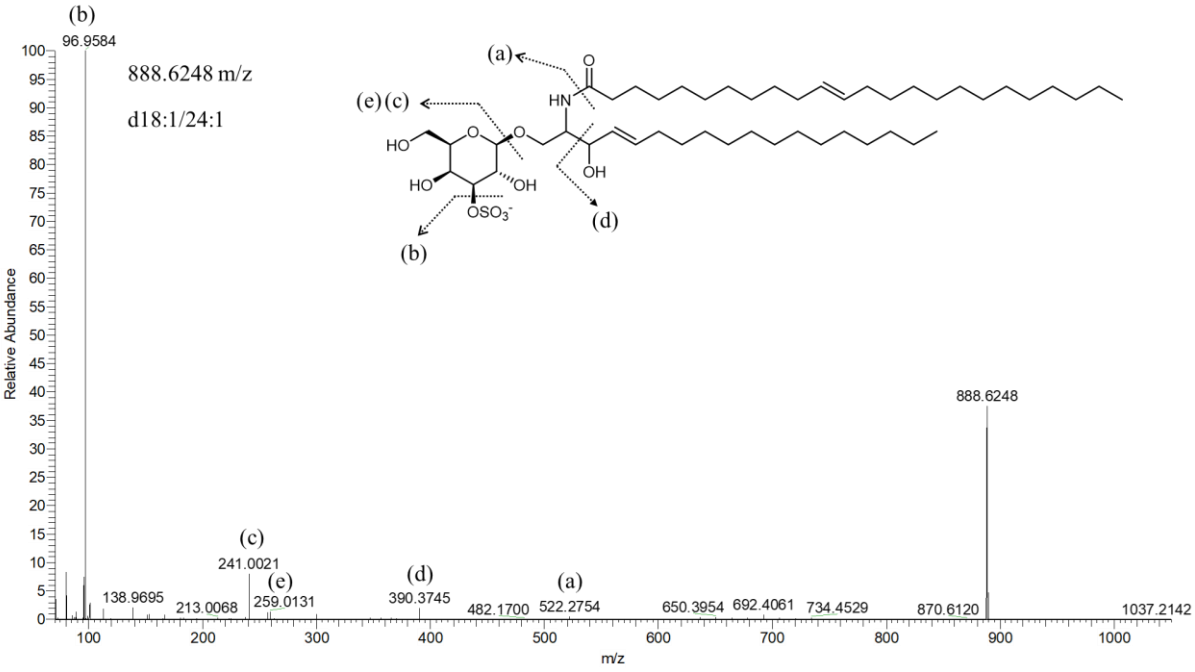

Figure 33 - MS/MS spectrum of the sulfatide *m/z* 888.6248540 $[M–H]^-$ from manual inspection of fraction F obtained via silica gel separation, acquired in negative electrospray ionization (ESI^-) using HCD at 45.0 eV.

Chapter 4

Biological activity of mouse brain sulfolipids

4.1 Development of an experimental platform for assessing TREM2 activity

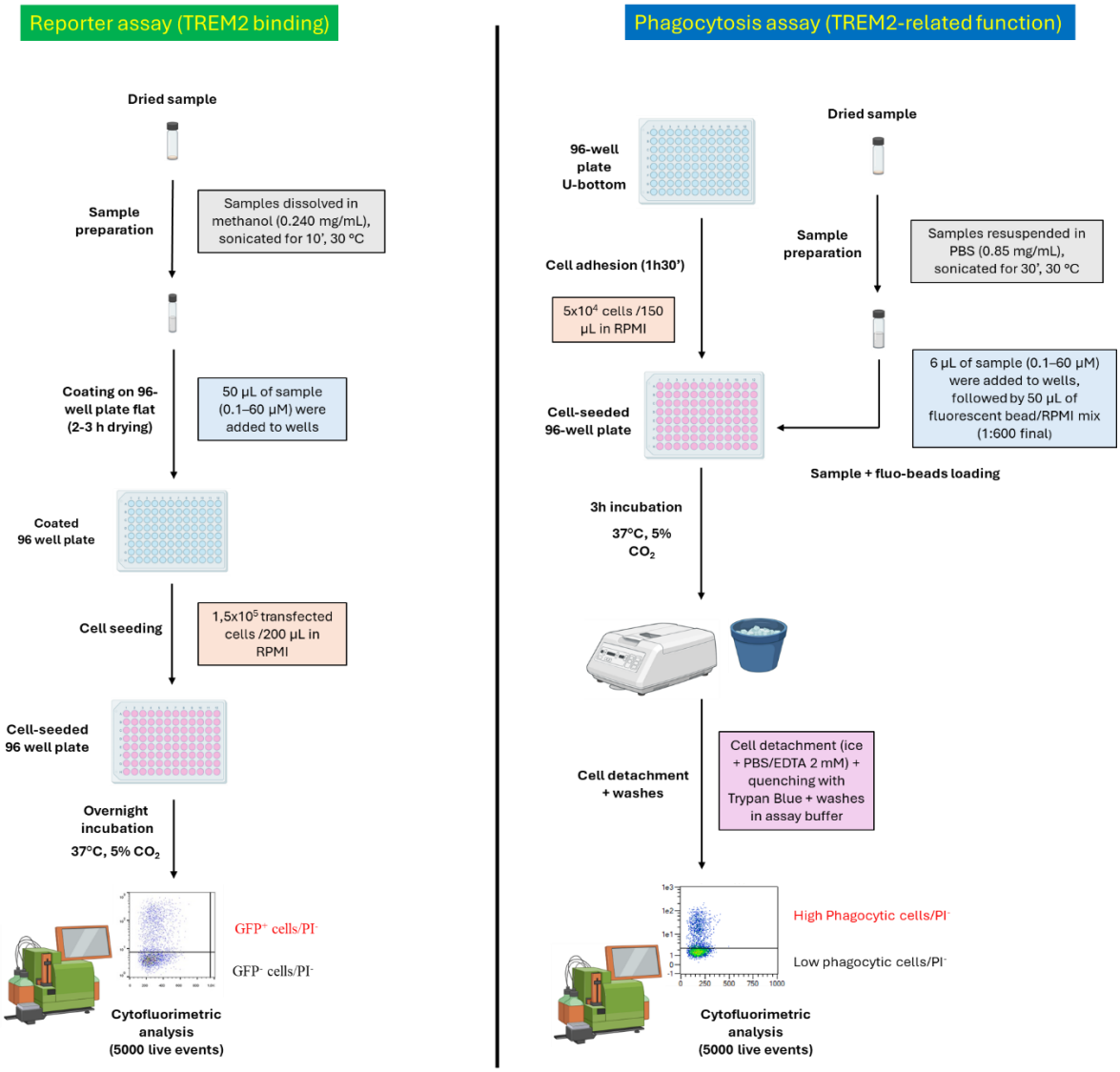

Figure 34 - Schematic overview of the integrated experimental platform for assessing TREM2 agonist activity. The system combines a TREM2 reporter assay in 2B4 immortalized cell line, designed to quantify receptor-mediated signalling activation by measure of GFP^+ cells, with a phagocytosis assay conducted in the immortalized murine microglial BV2 cell line, with quantification of engulfment of IgG FITC beads. This

integrated approach enabled a comprehensive evaluation of both proximal receptor activation events and downstream TREM2-dependent functional outcomes.

An integrated biological assay platform was developed to investigate the potential of the identified sulfolipids as putative TREM2 agonists. This experimental approach coupled the analysis of the receptor activation, determined through a cellular TREM2 reporter assay[39], with the measure of a TREM2 linked function, as the phagocytosis test in the immortalized murine microglial BV2 cell line.
The entire procedure was defined by two protocols for the *in vitro* selection of small lipidic molecules for the TREM2 activity that are reported in the **Figure 34**.

4.2 Sulfolipids bioassay on TREM2 reporter cell line

The anion-exchange fractions derived from the mouse brain extracts (Section II, paragraph 3.2.1) were evaluated in the TREM2 reporter system at 10, 30, and 60 µg/mL. MAs [53], SULF A [50], and PSs [101] were used as positive controls at 30 µg/mL (**Figure 35**) since are three reported TREM2 putative ligands (53, 50, 101). Receptor activation in this assay was quantified as the percentage of GFP^+ cells.
Fraction D exhibited a significative and dose-dependent activity at 30 and 60 µg/mL. Lipidomic analysis revealed that this fraction was qualitatively composed of PSs, PIs, and sulfolipids. Interestingly, fraction A was also active, eliciting a response at 10 µg/mL and reaching a maximum at 30 µg/mL. Its lipid content is dominated by ceramides, PEs, and MGDGs. The observed activity may reflect the enrichment in PEs, a class of phospholipids previously described alongside PSs as putative TREM2 agonists [101].

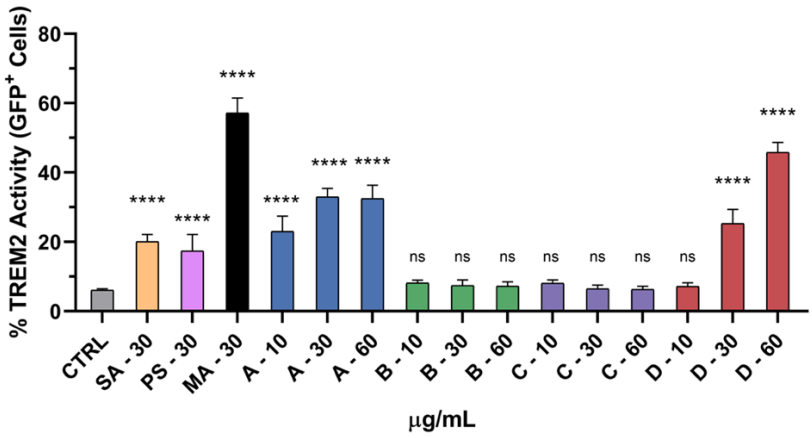

Figure 35 - 2B4 human TREM2/DAP12 reporter cells stimulated with anionic exchange fractions from brain extracts at the indicated concentrations. SULF A (SA), PS (PS) and Mycolic acid (MA) 30 µg/mL were used as positive control. TREM2 activity (GFP expression) was assessed after overnight incubation by flow cytometry. Data represent the mean of technical duplicates from three independent experiments (n = 3). Statistical analysis: ordinary one-way ANOVA, ****$p \leq 0.0001$ versus CTRL (vehicle).

The MZmine deconvolution of anionic exchange fraction D revealed a sulfolipid profile closely resembling the one observed in the brain extract. In addition to PSs and PIs, this fraction contained the three distinct pools of sulfolipids described above, namely sulfatides, SGDGs, and seminolipids. Among these, sulfatides are essential structural constituents of the myelin and, therefore, represent the predominant class in the brain. On the other hand, SGDGs and seminolipids share pronounced chemical similarity with the TREM2 ligand SULF A [51], as the presence of a sulfur-bearing, charged glycosyl headgroup attached to an acylated glycerol backbone. We prioritized these two classes for functional evaluation in our bioassay platform.

Since the abundance of both families is considerably low in mouse brain and their chemical similarity renders their separation technically challenging, two synthetic analogues, namely SGDG 16:0/16:0 S (809.51 m/z, M–H) and seminolipid 18:0/16:0 R (823.56 m/z, M–H), of each class were synthesized (Section III, paragraph 5.14) and evaluated in the TREM2 reporter assay across a 0.1–75 μM concentration range (**Figure 36A**). Their activity was compared to TREM2 agonist SULF A, a commercial pool of PSs and commercial MAs (**Figure 36A-B**). Consistent with previous reports, MAs robustly activated TREM2 signaling, showing approximately 50% of GFP^+ cells already at 10 μg/mL. The synthetic SGDG displayed minimal receptor activity, reaching approximately 12% GFP^+ cells, comparable to PSs but markedly lower than SULF A, which elicited about 30% GFP^+ cells at 60 μM (**Figure 36B**). In contrast, the synthetic seminolipid exhibited robust, dose-dependent receptor engagement, exceeding the response induced by SULF A (**Figure 36B**).

4.3 Sulfolipid effect on microglial phagocytosis

The physiological role of these molecules in the mouse brain was assessed by their impact on microglial phagocytosis, a key functional readout involved in TREM2 signaling [11]. Phagocytosis was measured in the immortalized murine microglial cell line BV2 using fluorescently labeled opsonized beads (IgG-FITC), internalized via the FcRγ receptor [102]. The proportion of cells actively engaging in phagocytosis was quantified by flow cytometry after three hours of incubation (Section III, section 5.15). Following classification into low- and high-phagocytic subsets, analyses were restricted to the high-phagocytic population (**Figure 34**).

The activity of the two synthetic molecules was assessed in comparison with SULFA A, PSs and MAs in the concentration range starting from 0.1 to 60 μM (**Figure 36C**). Both SULF A and PS enhanced microglial phagocytosis in a dose-dependent manner, increasing the proportion of highly phagocytic cells by approximately 20% relative to baseline, whereas MAs failed to elicit any detectable effect.

SGDG showed no significative effect. Seminolipid, on the other hand, displayed activity comparable to SULF A and PS, producing an even stronger response at 60 µM (**Figure 36C**).

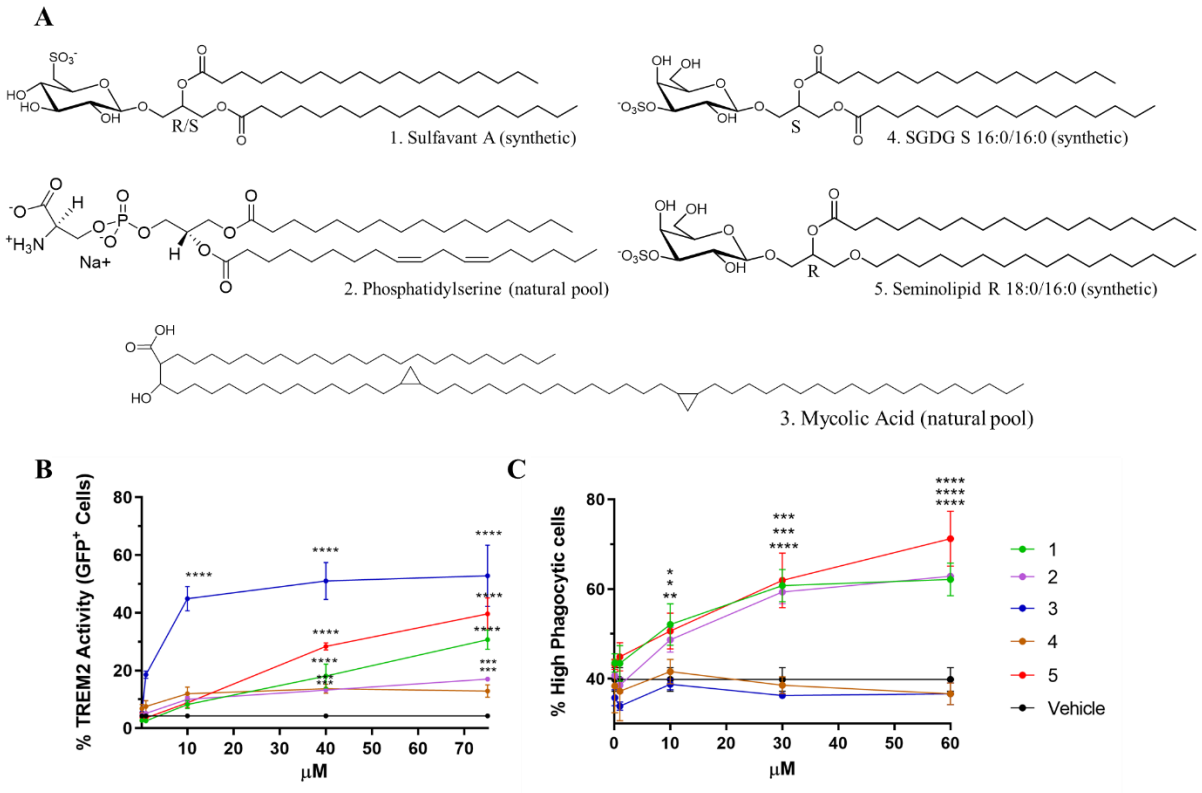

Figure 36 – **Biological properties of mouse brain sulfolipids**. (A) Chemical structures of synthetic SULF A, SGDG S 16:0/16:0, seminolipid R 18:0/16:0, and a representative member from a pool of PSs and MAs. (B) Dose-dependent curves of hTREM2/DAP12 reporter cells treated with synthetic seminolipid 18:0/16:0 and SGDG 16:0/16:0, compared to SULF A, PSs and MAs at the indicated concentrations. GFP-based TREM2 activation was assessed by flow cytometry after overnight incubation considering GFP^+ cells. Data represent mean ± range from three independent experiments (n = 3). Statistical analysis was performed by ordinary one-way ANOVA, ***p ≤ 0.001, ****p ≤ 0.0001 versus vehicle. (C) Phagocytosis assay in the murine BV2 microglial cells. Seminolipid R 18:0/16:0, SGDG S 16:0/16:0, SULF A, PSs and MAs phagocytic activity was expressed as the percentage of high-phagocytic cells, following 3-hour incubation at indicated concentrations. Data represent the mean of technical duplicates from three independent experiments (n = 3) Statistical analysis was performed by ordinary one-way ANOVA, *p ≤ 0.05, **p ≤ 0.01, ***p ≤ 0.001, ****p ≤ 0.0001 versus vehicle.

DISCUSSION

The overarching goal of this PhD project was to advance the mechanistic understanding of TREM2 activation by small molecules, with particular focus on the molecular logic that governs receptor engagement, adaptor communication, and physiological modulation. In the absence of well-defined endogenous ligands and given the complexity of TREM2 signalling, this work pursued two complementary aims in (1) dissecting the architecture of receptor–adaptor communication through biochemical perturbation of the TREM2-DAP12 axis, and (2) interrogating physiological mechanisms in mammalian systems to identify endogenous lipid mediators capable of modulating TREM2 under biologically relevant conditions. Together, these approaches provide an integrated framework for resolving ligand-dependent mechanisms of TREM2 activation.

The molecular interface between TREM2 and its signalling adaptor DAP12 is a critical step that enables phosphorylation-dependent downstream cascades [103]. Peptides capable of modulating this interaction offer a promising, yet underexplored, opportunity to probe TREM2 signalling with high spatial and temporal precision. In this context, the DAP12-affine peptide IA9-K (IFLIKILAA) is capable of interfering with the TREM2–DAP12 interaction in a sequence-specific manner, and was evaluated as a mechanistic tool, revealing that its inhibitory capacity strongly depends on its counterion. Moreover, the trifluoroacetate (TFA) form robustly inhibited TREM2 activation in a dose-dependent manner, whereas the hydrochloride (HCl) variant displayed markedly reduced activityThis counterion effect recapitulates and extends observations made for other SCHOOL peptides. Biophysical analyses shed light on the structural basis for these functional differences. Circular dichroism spectra acquired in variable TFE/H_2O environments showed that both peptide forms adopt predominantly β-structured conformations in aqueous solutions and undergo partial unfolding under more hydrophobic conditions and displaying incipient α-helical features, although IA9-K/HCl showed impaired recovery of β-structuring. Oriented CD experiments further demonstrated that only IA9-K/TFA undergoes a transition from surface association to bilayer insertion, adopting a carpet-like arrangement at higher peptide densities; IA9-K/HCl, in contrast, remained surface-confined. NMRtist-based structural predictions corroborated these findings by showing that chloride stabilizes compact, membrane-impaired folds, whereas TFA stabilizes extended conformations compatible with membrane penetration. These mechanistic insights have two important implications. First, they establish IA9-K as a chemical biology

tool capable of selectively perturbing the TREM2–DAP12 interface in a tunable manner. Because the peptide acts downstream of ligand binding but upstream of intracellular phosphorylation, it provides a unique opportunity to dissect ligand-dependent signalling logic and to distinguish between effects attributable to ligand binding, receptor clustering, or adaptor engagement. Second, they open opportunities for pharmacological applications. Modulating adaptor engagement offers a strategy to fine-tune TREM2 signalling rather than simply activating or inhibiting the receptor. Peptides such as IA9-K, once optimally formulated, could be developed as modulators of TREM2-dependent inflammatory states, either dampening maladaptive responses (e.g., chronic neuroinflammation) or enhancing beneficial ones (e.g., phagocytic clearance). The counterion-dependent behaviour identified here provides a rational starting point for optimizing therapeutic peptide formulations that achieve precise pharmacodynamic profiles. Taken together, these findings enrich our mechanistic understanding of TREM2-DAP12 communication and establish peptide-based perturbation as a powerful strategy for dissecting and ultimately manipulating receptor signalling.

The second major objective was to investigate whether sulfur-containing brain lipids could serve as endogenous modulators of TREM2. Guided by the receptor's preference for anionic lipidic structures and the previous identification of Sulfavant A as a synthetic agonist, this project focused on uncovering structurally distinct endogenous molecules capable of modulating TREM2 in mammalian systems. An untargeted LC–MS/MS workflow supported by MZmine deconvolution enabled the detection of low-abundance sulfolipids that conventional database-guided tools failed to annotate. Three major classes of 3-O-sulfogalactolipids were identified: sulfatides, sulfo-galactosyl-diacylglycerols (SGDGs), and seminolipids, with SGDGs and seminolipids undergoing subsequent structural validation. This semi-untargeted approach, which leverages characteristic mass fragmentation behaviour, proved particularly effective for retrospective interrogation of complex lipidomes. To evaluate biological relevance, an integrated bioassay platform was developed to assess TREM2-dependent activity of purified sulfolipid families. A striking divergence emerged as SGDGs elicited minimal activation, whereas seminolipid triggered robust, dose-dependent TREM2 engagement and enhanced phagocytic activity, comparable to Sulfavant A and much higher than phosphatidylserine. Importantly, seminolipid activity cannot be attributed to structural similarity with Sulfavant A. Rather, its distinct glycosylated architecture suggests that it activates TREM2 through a fundamentally different molecular interaction. This finding highlights seminolipid as a novel and biologically meaningful endogenous TREM2 modulator, distinct from synthetic agonists and uniquely positioned to inform physiological models of receptor activation.

Recent studies reporting a sharp age-dependent decline of SGDGs and seminolipids in the mouse brain [104] lend further significance to these findings. The reduction of seminolipid with aging, as

demonstrated here to be a potent TREM2 activator, suggests a mechanistic link between sulfolipid metabolism, microglial responsiveness, and age-related vulnerabilities relevant to neurodegenerative diseases. The results of this project therefore reinforce the emerging concept that endogenous sulfolipid–TREM2 interactions may represent a physiologically meaningful signalling axis, with seminolipid playing a central role.

CONCLUSIONS

By combining biochemical perturbation of receptor-adaptor communication with physiologically grounded exploration of brain-derived lipids, this work advances our understanding of the ligand-dependent mechanisms governing TREM2 activation. IA9-K is established as a chemically and structurally tunable tool, potentially pharmaceutically relevant, for interrogating and modulating TREM2-DAP12 signalling. In parallel, seminolipid amd sulfurlipid metabolism emerge as a previously underappreciated, structurally distinct endogenous modulator capable of shaping TREM2-dependent microglial responses. Together, these findings provide mechanistic clarity, identify promising molecular tools, and unveil new endogenous ligands that expand our understanding of TREM2 signalling in brain physiology and disease.

Section III: Materials and method

Chapter 5

5.1 Chemicals and reagents

Sulfavant A [105], Phosphatidylserine (P0474, Sigma-Aldrich), Mycolic Acid (M4537, Sigma-Aldrich)

5.2 Animals, Ethical statements and brain sampling

All animal experiments were performed in accordance with the ARRIVE guidelines to ensure transparent and ethical reporting of bioscience research involving laboratory animals. Procedures were approved under the European Union Directive 2010/63/EU and the Italian Legislative Decree No. 26/2014 (authorization Nos. 307/2018-PR E58D.8 and 783/2020). C57BL/6 mice (Charles River Laboratories, Wilmington, MA, USA) were housed under controlled conditions (12 h light/dark cycle, lights on at 06:00; ambient temperature 20–22 °C; humidity ~50%) with ad libitum access to chow and water. Mice were sacrificed at 8–10 weeks of age by CO_2 inhalation followed by cervical dislocation (ZT4–ZT6). Every effort was made to minimize animal suffering and to reduce the number of animals used. Whole murine brains were quickly removed from the skull and 177 immediately frozen in a dish plate and put in a box over dry ice. 178 Frozen tissues were stored at −80 °C until extraction.

5.3 Peptides synthesis

Fmoc-protected amino acids, Fmoc-Rink-amide MBHA, and coupling reagents (HBTU, HOBt, and HATU) were purchased from Irish Biotech (Marktredwitz, Germay). DMF, DIPEA, and solvents were obtained from Sigma-Aldrich (Milan, Italy). Peptides were synthesized by manual solid phase on a Wang resin, preloaded with the first Ala residue (Fmoc-Ala-Wang, 0.68 mmol/g loading), using Fmoc chemistry in a 0.112 mmol scale. HATU activation employed a three-fold molar excess (0.4 mmol) of Fmoc-amino acids in DMF for each coupling cycle. Coupling times were 45 min. Fmoc deprotection was performed using a 5% w/v piperazine solution in DMF in presence of 2% DBU. The cleavage from the resin was performed by treatment with TFA-triisopropylsilane-H_2O (95:3:2 v/v). The peptide, dissolved in HFIP/TFE 1:5 v/v, was purified by preparative Reverse Phase HPLC using a Shimadzu LC-

8 (Shimadzu, Kyoto, Japan) system equipped with a Phenomenex Juppiter 5 µ, 300 Å, 250x21.2 mm, C5 column (Phenomenex, Torrance, CA, USA). The column was perfused at a flow rate of 12 mL/min with a mobile phase containing solvent A (0.05% TFA in water) and a 28-36% in 55 min linear gradient of solvent B (0.05% TFA in acetonitrile/water, 9:1 by vol.). The fractions containing the desired products were collected and lyophilized to constant weight. Analytical HPLC was performed on a Shimadzu LC-10 instrument fitted with a Jupiter C5, 10µ, 250x4.6 mm column (Phenomenex, Torrance, CA) using the above solvent system (solvents A and B), flow rate of 1 mL/min, detection at 216 nm. The molecular weight of the compound was determined by LC-ESI-MS on an Agilent Infinity II system.

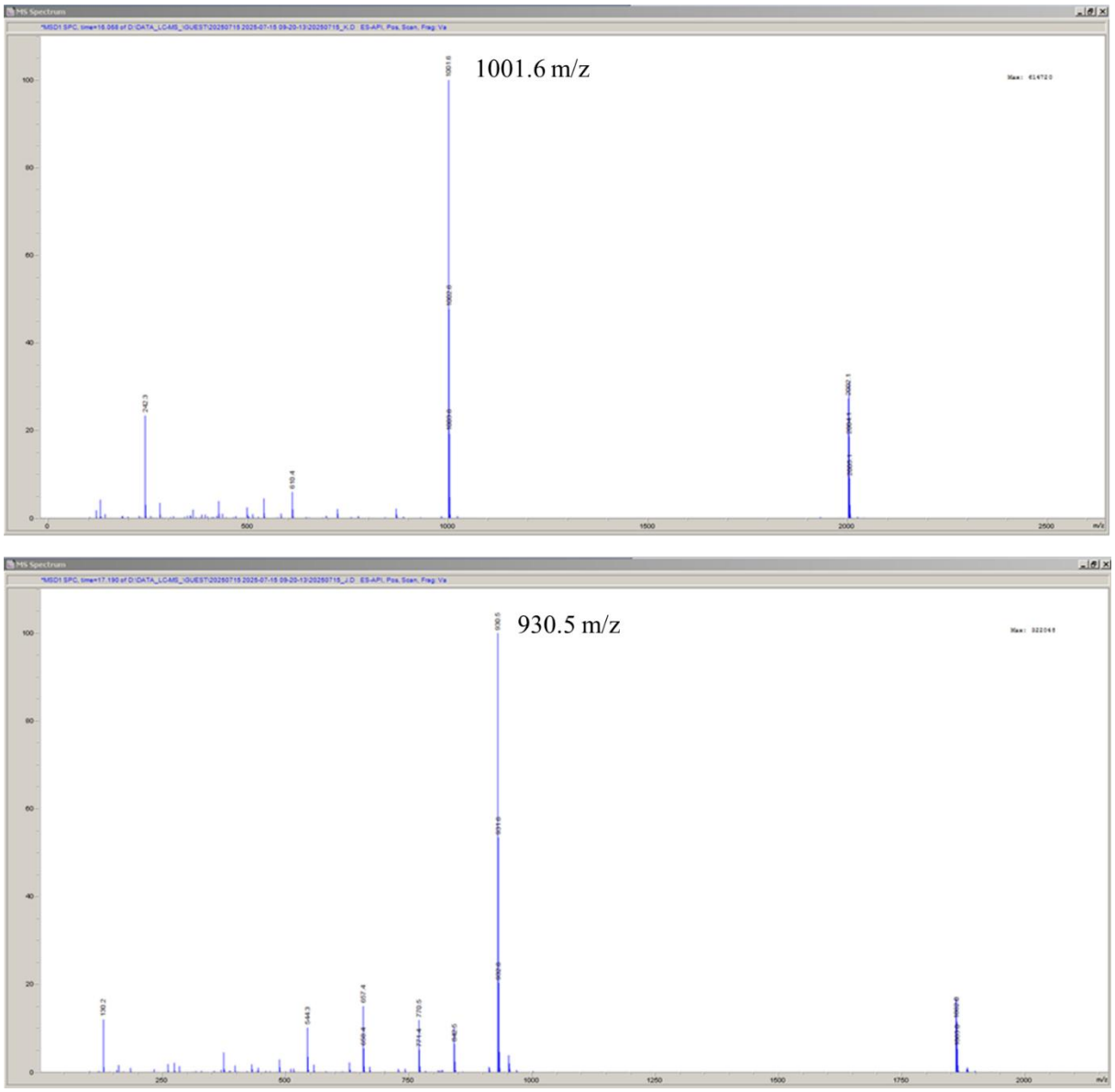

Figure 36 – Peptides LC-ESI-MS analysis (A) IA9-K (H-IFLIKILAA-OH) calculated $[M+H]^+$: 1001.3 *m/z*; found: $[M+H]^+$: 1001.6 *m/z*; (B) IA9-G (H-IFLIGILAA-OH) calculated $[M+H]^+$: 930.2 *m/z*; found: $[M+H]^+$: 930.5 *m/z*.

5.4 TREM2 cellular reporter system

2B4 mouse T cell hybridoma cells stably transfected with enhanced green fluorescent protein (eGFP) under NFAT consensus sequences and human TREM2/DAP12 cDNA were kindly provided by Prof. Marco Colonna (Washington University in St. Louis). Stable clones were selected with G418 (1 mg/mL) and maintained in RPMI-1640 medium (Gibco) supplemented with 10% fetal bovine serum (Gibco). Cells were cultured for up to 20 passages, maintaining a maximum density of 1×10^6 cells/mL. For activity assays, 2×10^5 cells were seeded in flat-bottom 96-well plates in 200 µL of medium and incubated overnight. Test compounds were dissolved in methanol (0.24 mg/mL) and coated onto the wells using 50 µL of the respective solution at the indicated concentrations. Peptides (Sigma-Aldrich) were dissolved in DMSO/PBS (1:1, v/v) and added to each well (4 µL; final concentration 2%). After overnight incubation, reporter cell activation was assessed using a MACSQuant® Analyzer 16 flow cytometer (Miltenyi Biotec) by quantifying the percentage of GFP^+ cells (5,000 events, propidium iodide–negative). Raw data were processed and analyzed using Prism 8 (GraphPad Software).

5.5 FLIM-FRET system

1 ug/mL IA9-K wad added to HMC3 immortalized human microglial cell line transfected with the vectors TREM2-mTurquoise and DAP12-YPET for the analysis of the protein interaction by a FRET/FLIM coupled system analysis (manuscript in preparation). Fluorescence lifetime images were acquired using the FLIM upgrade kit (Picoquant, Berlin, Germany) for the Nikon 1AR confocal laser scanning microscope. Fluorescence of mTurquoise2 was excited using a pulsed laser source (PDL 828 Sepia II, Picoquant) at a wavelength of 444 nm and a repetition rate of 20 Mhz. Single photons and their arrival times were detected (PicoHarp300, 483/35 filter) using time correlated single photon counting (TCSPC) method.

5.6 Circular Dichroism in TFE/H_2O mixtures

Peptides were dissolved in 2,2,2-trifluoroethanol (TFE) at a concentration of 0.5 mg/mL and subsequently diluted in Milli-Q water/TFE to achieve the desired solvent conditions to a concentration of 0.1 mg/mL. The CD spectra were recorded on a Jasco J-1500 dichrograph using the Spectra Manager software (Jasco, Tokyo, Japan). CD spectra were recorded in a 1 mm quartz cuvette thermostated at 25°C. Spectra were acquired over the 180–260 nm range with a data pitch of 0.5 nm, a scanning speed of 50 nm/min, digital integration time of 1 sec and a bandwidth of 1.0 nm.

5.7 Oriented Circular Dichroism (OCD) in solid-supported phospholipid layer

Peptide stock solutions were prepared in $CHCl_3/CH_3OH$ (1:1, v/v) at a concentration of 2.44 mg mL^{-1}, and lipid stock solutions (DMPG:DMPC, 1:3 mol/mol) were prepared in $CHCl_3/CH_3OH$ (1:1, v/v) at 10 mg mL^{-1}. Lipids and peptides were mixed to obtain lipid-to-peptide molar ratios (L/P) of 15:1 and 60:1. Aliquots of 24 µL (3x 8 µL) of each sample were deposited onto fused silica or CaF_2 support, the solvent was allowed to evaporate at ambient conditions and then removed under reduced pressure for 3 hours to form thin films. The samples were then allowed to equilibrate in a sealed container for 48 h using a saturated K_2SO_4 solution to maintain relative high humidity (a_w=0.99 for a saturated K_2SO_4 solution in water). An in-house built cell was employed (ICB-CNR laboratories of Padova, Italy): it accommodates two fused silica windows (one with the deposited peptide/lipid sample, the second to create a sealed chamber) and contains a small reservoir for taking up an aqueous salt solution for humidifying the sample. The incident light beam is perpendicular to these windows, and between scans the cell is rotated around the beam direction, and the geometry of the cell was studied to maintain the sample at the same distance from the detector when flipping the cell front-to-back. Spectra were recorded over the 180–260 nm wavelength range at two rotation angles (0° and 90°) on the front face, then flipped to acquire the measurement from the back face at the same 0° position. Scanning speed was 50 nm min^{-1}, digital integration time was 1 sec, and bandwidth was 1 nm.

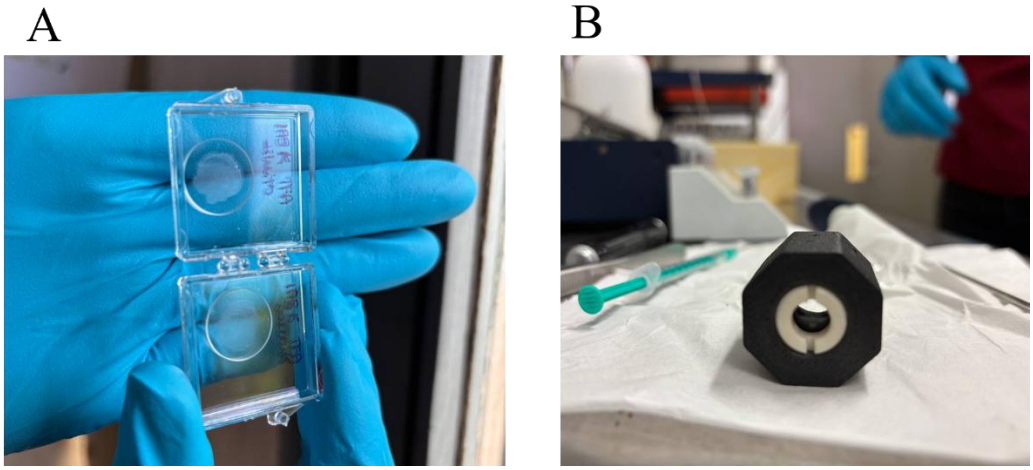

Figure 37 – **OCD in-house system.** (A) Peptide/lipid samples dissolved in $CHCl_3/CH_3OH$ (1:1, v/v) and deposited onto a CaF_2 substrate. (B) 3D-printed octagonal cell with two fused-silica windows and a small reservoir for aqueous salt solution to humidify the sample

5.8 3D-structure prediction via NMRtist

NMR spectra were acquired using a Bruker Avance DMX 600 MHz spectrometer (Bruker Corp., Billerica, MA, USA), operating at 599.90 MHz for 1H at 298 K. Peptides were dissolved at 0.5 mM in DMSO-d_6 and analyzed at 298 K on a Bruker spectrometer using standard COSY, TOCSY, and ROESY pulse sequences. Data were processed with TopSpin and further analyzed through NMRtist, Bruker's AI-based platform for automated spectral interpretation and 3D structure determination, yielding ensembles of the 20 lowest-energy conformers for each peptide [83].

5.9 Bligh and Dyer method

Brains from two-month-old female wild-type mice were extracted with methanol (Merck Life Science S.r.l., Milan, Italy) and homogenized using a Precellys Evolution system equipped with a Cryolys Evolution cooling unit (Bertin Italia, Genoa, Italy) at 6200 rpm (3 × 30 s cycles) and 6 °C. Homogenates were centrifuged at 3750 rpm for 10 min at 4 °C, and the supernatants collected. The remaining pellets were re-extracted following a slightly modified Bligh and Dyer protocol: pellets were resuspended in 2 mL of methanol and 1 mL of chloroform ($CHCl_3/CH_3OH$ 1:2, v/v), and the supernatants pooled. Biphasic extraction was then performed by adding 2 mL of methanol, 1 mL of chloroform, and 0.8 mL of Milli-Q water ($CHCl_3/CH_3OH/H_2O$ 1:2:0.8, v/v/v), followed by adjustment to $CHCl_3/CH_3OH$ /H_2O 2:2:0.8 (v/v/v) to achieve complete phase separation. The organic layer was collected, dried under reduced pressure at ≤24 °C, and further evaporated under a nitrogen stream. A second extraction of the remaining aqueous phase was performed using the same solvent ratio, and the combined organic fractions were evaporated to dryness, weighed, and stored at −80 °C.

5.10 Anion exchange chromatography

The mouse brain raw extracts were subjected to anionic exchange chromatography by using CHROMABOND® NH2 cartridges (6 mL/500 mg, Macherey-Nagel, Düren, Germany). Sample preparation, column conditioning, and the eluents used are summarized as follows:

Sample preparation	Column activation and conditioning	Elution gradient
Sample is dissolved in 1mL of $CHCl_3/CH_3OH$ 9:1 (*v/v*) and dried on silica gel	5mL of CH_3OH 5mL of H_2O 5mL of HCl 0.1M 5mL of H_2O 5mL of CH_3OH 5mL of $CHCl_3/CH_3OH$ 9:1 (*v/v*)	10mL of $CHCl_3/CH_3OH$ 9:1 (*v/v*) 10mL of $CHCl_3/CH_3OH$ 8:2 (*v/v*) 10mL of $CHCl_3/CH_3OH$ 75:25 (*v/v*) 10mL of $CHCl_3/CH_3OH$ 8:2 (*v/v*) + 100mM CH_3COONH_4+2% NH_3

5.11 LC-MS/MS analysis

Mouse brain extracts and the anion-enriched fractions were analyzed by HRESI-MS/LC-MS/MS using a Q-Exactive™ Hybrid Quadrupole-Orbitrap™ mass spectrometer (Thermo Scientific, Waltham, MA, USA) coupled to an 1290 Infinity UPLC system (Agilent Technologies, Santa Clara, CA, USA) equipped with an ESI source operated in negative mode. Separation was performed on a Phenomenex Luna C18 column (150 × 2.6 mm, 5 µm) using water containing 0.005% NH4OH/CH3COOH (pH 8, solvent A) and methanol (solvent B). The gradient was run from 70:30 A/B to 100% B over 30 min at 0.3 mL min−1. HRESI parameters were spray voltage 3.0 kV, capillary temperature 320 °C, sheath gas 40, auxiliary gas 25. The Q-Exactive™ was operated in data-dependent acquisition mode with a full-MS scan at 70,000 resolution, AGC target 1 × 10^6, maximum injection time 100 ms, and *m/z* range 150–2000. dd-MS2 scans were acquired at 17,500 resolution, AGC target 1 × 10^5, maximum injection time 75 ms, isolation window 1.0 *m/z*, stepped normalized collision energies of 35, 42, and 50, and *m/z* range 70–1500. Raw LC-MS/MS data were processed for lipid identification and relative quantification using LipidSearch v5 (Thermo Scientific), following the manufacturer's recommended workflow.

5.12 MZmine raw data deconvolution

Raw LC-MS data were first converted to mzML format using ProteoWizard [106] and subsequently imported into MZmine v4.5.0 [86] for deconvolution. Mass detection was performed with the following parameters: scan filter, retention time, autorange; MS level, all; polarity, any; spectrum type, any; IMS scan type, all; mass detector, exact mass; noise level, 1.0 × 10^1. MS/MS scatter plots were generated to identify sulfate-containing compounds, using retention time as the x-axis, precursor *m/z* as the y-axis, and product ion intensity as the z-axis. MSn scans (≥2) were included, with *m/z* tolerance set to 0.0050 *m/z* or 2 ppm. Intensities filtering, number of best fragments 95 and Base Peak percent % 10. Diagnostic fragmentation filtering was applied using the product ion *m/z* 96.958 ($HSO4^-$) for sulphated lipids and *m/z* 80.963 ($HSO3^-$) for sulphonated lipids. The resulting precursor ions merged list were exported to Excel for MS/MS manually inspection (Thermo Xcalibur Qual Browser).

5.13 Silica gel chromatography

D fraction obtained from anion-exchange chromatography was further purified by silica gel column chromatography using a stepwise $CHCl_3$/CH_3OH gradient (95:5, 20 mL; 9:1, 32 mL; 88:12, 40 mL; 8:2, 20 mL; 7:3, 20 mL; and $CHCl_3$/CH_3OH/H_2O 68:18:2, 20 mL), yielding 11 subfractions. The metabolite distribution within each fraction was monitored by thin-layer chromatography (TLC) using chloroform/methanol (7:3, v/v) and chloroform/methanol/water (65:25:4, v/v/v) as solvent systems.

TLC plates were visualized with $Ce(SO_4)_2$ Fractions C and E–G were further analyzed by ^1H NMR spectroscopy (Bruker DRX 600 MHz, Bruker BioSpin, Fällanden, Switzerland) using $CD_3OD/CDCl_3$ (δ 3.34 and 7.26 ppm) and by direct infusion high-resolution (HR) ESI-MS/MS on a Q-Exactive™ Hybrid Quadrupole-Orbitrap™ mass spectrometer (Thermo Scientific, Waltham, MA, USA) operating in negative ion mode. The HRESI source parameters were as follows: spray voltage 3.00 V; capillary temperature 320 °C; sheath gas flow rate 12; auxiliary gas 0. Mass Spectrometer was operated with one Full-MS scan at a resolution of 70.000, AGC target 1e6, Maximum injection time (IT) 50ms and a scan range of 150-2000 *m/z*; dd-MS2 was performed with MS-MS with an isolation window 1.0 *m/z* and a scan range of 70-1500 *m/z*.

5.14 Synthesis of sulfolipids analogues

General Experimental Procedures.

NMR spectra were recorded on a Bruker Avance-400 (400.13 MHz) and on a Bruker DRX-600 equipped with a TXI CryoProbe in $CDCl_3$ and in $CDCl_3$:CD_3OD 1:1 (δ values are referred to $CHCl_3$ and CH_3OH at 7.26 and 3.34 ppm respectively). HR-MS spectra were acquired by a Q-Exactive Hybrid Quadrupole-Orbitrap mass spectrometer (Thermo Scientific). TLC plates (Kieselgel 60 F_{254}) and silica gel powder (Kieselgel 60, 0.063–0.200 mm) were from Merck. All the reagents were purchased from Sigma-Aldrich and used without any further purification

Final product - (R)-1-O-hexadecyl-2-O-stearoyl-3-O-β-[(3-O-oxysulfonyl)-D-galactopyranosyl]-glycerol (Seminolipid, R 18:0/16:0)

^1H NMR (400 MHz, $CDCl_3/CD_3OD$ 1/1): δ 5.18 (1H,m, H-2), 4.30 (1H, d, *J* = 7.9 Hz H-1'), 4.23 (1H, bd, *J* = 3.0 Hz, H-4'), 4.20 (1H, dd, *J* = 3.0, 10.3 Hz, H-3'), 3.92 (1H, dd, *J* = 5.8, 10.8 Hz, H-1a), 3.86-3.68 (4H, m, H-2', H-6'a-b, H-1b), 3.60 (2H, m, H-3), 3.54-3.38 (3H, m, overlapped, H-5', O*C*H_2CH_2), 2.31 (2H, m, α-methylene), 1.69-1.58 (4H, m, β-methylene), 1.43-1.29 (acyl chain), 0.94 (6H, overlapped, $2CH_3$); ^{13}C NMR (100 MHz, $CDCl_3$): δ 172.5, (*C*OCH_3, acyl ester), 104.2 (CH, C1'), 80.9 (CH, C3'), 75.0 (CH, C5') 72.1 (CH, C2), 71.6 (CH_2, O*C*H_2CH_2), 69.7 (CH_2, C3), 69.1 (CH, C2'), 68.1 (CH_2, C1), 67.3 (CH, C4'), 61.6 (*C*H_2OH, C6'), 34.5 (CH_2, α-methylene of stearoyl portion), 32.3−24.0 (CH_2, methylenes of aliphatic portion), 20.0-14.0 (CH_3, methyls of aliphatic portion). HRESIMS *m/z* 823.5624, $[M - H]^-$ (calcd for $C_{43}H_{83}O_{12}S^-$, 823.5611).

Final product - 1,2-O-palmitoyl-3-O-β-[(3-O-oxysulfonyl)-D-galactopyranosyl]-sn-glycerol (SGDG, S 16:0/16:0)

^{1}H NMR (400 MHz, $CDCl_3/CD_3OD$ 1/1): δ 5.27 (1H, m, H-2), 4.43(1H, dd, J= 3.1, 12.1 Hz, H-1a), 4.35 (1H, d, *J* = 7.9 Hz H-1'), 4.26-4.19 (3H, overlapped, H-3', H4', H-1b), 3.93 (1H, dd, J=5.4, 10.9 Hz, H-3a), 3.82 (1H, dd, J=5.4, 10.9 Hz, H-3b), 3.78-3.72 (3H, overlapped, H-6'a-b, H5'), 3.54 (1H, bt, J= 6.1 Hz, H-2'), 2.31 (4H, m, α-methylene), 1.62-1.55 (4H, overlapped, β-methylene), 1.33-1.20 (48H, overlapped, acyl chain), 0.87 (6H, overlapped, $2CH_3$). As reported in the literature, the NMR spectrum contains trace of signals of the *R* epimer [107]. HRESIMS *m/z* 809.5098, $[M-H]^-$ (calcd for $C_{41}H_{77}O_{13}S^-$, 809.5090).

5.15 BV2 Phagocytosis assay

Cells (5×10^4 per well) were seeded in 96-well plates in 150 µL of complete RPMI medium and allowed to adhere for 1.5 h at 37 °C in a humidified incubator (5% CO_2). Dry samples were resuspended in PBS to a final concentration of 0.85 mg/mL and sonicated for 30 min at 30 °C. Subsequently, 6 µL of each solution at the desired concentration was added to the wells. Notably, MA samples were applied in coating following the same procedure used in the reporter assay. After sample addition, 50 µL of RPMI containing IgG-FITC–coated beads (Cayman Chemical) diluted 1:150 were added to achieve a final bead concentration of 1:600. Cells were incubated for 3 h under standard culture conditions. Following incubation, the medium was carefully removed, and cells were washed with 200 µL of PBS containing 2 mM EDTA, then incubated on ice for 10 min to facilitate detachment. Cells were gently pipetted to complete detachment and centrifuged at 400 × g for 5 min at 4 °C. The supernatant was discarded, and the pellet was treated with 25 µL of Trypan/Assay Buffer (1:10) for 2 min to quench. After adding 150 µL of Assay Buffer, cells were centrifuged again at 400 × g for 5 min at 4 °C. The supernatant was removed, and cells were washed with 200 µL of Assay Buffer to remove residual Trypan, followed by centrifugation. Finally, cells were resuspended in 100 µL of Assay Buffer and stained with 1 µL of propidium iodide (1:10 dilution) for 5 min to assess viability. Samples were immediately analyzed by flow cytometry. Vehicle control cells were divided into low- and high-phagocytic populations, and the percentage of high-phagocytic cells was quantified using Prism 8 (GraphPad Software).

Reference

1. Colonna M, Wang Y. TREM2 variants: New keys to decipher Alzheimer disease pathogenesis. Nat Rev Neurosci. 2016 Apr 1;17(4):201–7.

2. Keren-Shaul H, Spinrad A, Weiner A, Matcovitch-Natan O, Dvir-Szternfeld R, Ulland TK, et al. A Unique Microglia Type Associated with Restricting Development of Alzheimer's Disease. Cell. 2017 Jun 15;169(7):1276-1290.e17.

3. Yeh FL, Hansen D V., Sheng M. TREM2, Microglia, and Neurodegenerative Diseases. Vol. 23, Trends in Molecular Medicine. Elsevier Ltd; 2017. p. 512–33.

4. Ulland TK, Song WM, Huang SCC, Ulrich JD, Sergushichev A, Beatty WL, et al. TREM2 Maintains Microglial Metabolic Fitness in Alzheimer's Disease. Cell. 2017 Aug 10;170(4):649-663.e13.

5. Lin M, Yu JX, Zhang WX, Lao FX, Huang HC. Roles of TREM2 in the Pathological Mechanism and the Therapeutic Strategies of Alzheimer's Disease. Vol. 11, Journal of Prevention of Alzheimer's Disease . Serdi-Editions; 2024. p. 1682–95.

6. Shirotani K, Hatta D, Wakita N, Watanabe K, Iwata N. The role of TREM2 N-glycans in trafficking to the cell surface and signal transduction of TREM2. J Biochem. 2022 Dec 1;172(6):347–53.

7. Guerreiro R, Wojtas A, Bras J, Carrasquillo M, Rogaeva E, Majounie E, et al. TREM2 Variants in Alzheimer's Disease . New England Journal of Medicine. 2013 Jan 10;368(2):117–27.

8. Saeb D, Lietzke EE, Fuchs DI, Aldrich EC, Bruce KD, Sprenger KG. The flexible stalk domain of sTREM2 modulates its interactions with brain-based phospholipids. Elife. 2025 Sep 10;13.

9. Turnbull IR, Gilfillan S, Cella M, Aoshi T, Miller M, Piccio L, et al. Cutting Edge: TREM-2 Attenuates Macrophage Activation. The Journal of Immunology. 2006 Sep 15;177(6):3520–4.

10. Liu Y, Theil S, Ibach M, Walter J. DAP12 interacts with RER1 and is retained in the secretory pathway before assembly with TREM2. Cellular and Molecular Life Sciences. 2024 Dec 1;81(1).

11. Hsieh CL, Koike M, Spusta SC, Niemi EC, Yenari M, Nakamura MC, et al. A role for TREM2 ligands in the phagocytosis of apoptotic neuronal cells by microglia. J Neurochem. 2009 May;109(4):1144–56.

12. Thornton P, Sevalle J, Deery MJ, Fraser G, Zhou Y, Ståhl S, et al. TREM 2 shedding by cleavage at the H157-S158 bond is accelerated for the Alzheimer's disease-associated H157Y variant . EMBO Mol Med. 2017 Oct;9(10):1366–78.

13. Suárez-Calvet M, Kleinberger G, Araque Caballero MÁ, Brendel M, Rominger A, Alcolea D, et al. sTREM 2 cerebrospinal fluid levels are a potential biomarker for microglia activity in early-stage Alzheimer's disease and associate with neuronal injury markers . EMBO Mol Med. 2016 May;8(5):466–76.

14. Mishra S, Swain PS, Pati S, Dehury B. Extracellular domain of TREM2 possess two distinct ligand recognition sites: Insights from machine-learning guided docking and all-atoms molecular dynamics simulations. Heliyon. 2025 Jan 15;11(1).

15. Greven JA, Wydra JR, Greer RA, Zhi C, Price DA, Svoboda JD, et al. Biophysical mapping of TREM2-ligand interactions reveals shared surfaces for engagement of multiple Alzheimer's disease ligands. Molecular Neurodegeneration . 2025 Dec 1;20(1).

16. McMillan IO, Liang L, Su G, Song X, Drago K, Yang H, et al. TREM2 on microglia cell surface binds to and forms functional binary complexes with heparan sulfate modified with 6-O-sulfation and iduronic acid. Journal of Biological Chemistry. 2024 Sep 1;300(9).

17. Sudom A, Talreja S, Danao J, Bragg E, Kegel R, Min X, et al. Molecular basis for the loss-of-function effects of the Alzheimer's disease-associated R47H variant of the immune receptor TREM2. Journal of Biological Chemistry. 2018 Aug 10;293(32):12634–46.

18. Byrne NJ, Lee AC, Kostas J, Reid JC, Partridge AT, So SS, et al. Development of a robust crystallization platform for immune receptor TREM2 using a crystallization chaperone strategy. 2020.

19. Yeh FL, Wang Y, Tom I, Gonzalez LC, Sheng M. TREM2 Binds to Apolipoproteins, Including APOE and CLU/APOJ, and Thereby Facilitates Uptake of Amyloid-Beta by Microglia. Neuron. 2016 Jul 20;91(2):328–40.

20. Paradowska-Gorycka A. U1-RNP and TLR receptors in the pathogenesis of mixed connective tissue disease: Part I. The U1-RNP complex and its biological significance in the pathogenesis of mixed connective tissue disease. Reumatologia. 2015;53(2):94–100.

21. Zhong Z, Ulmschneider M, Lorenz CD. Understanding the binding mechanisms of Alzheimer risk factor TREM2 in lipid bilayer using multi-scale molecular dynamics simulations [Internet]. 2024. Available from: http://biorxiv.org/lookup/doi/10.1101/2024.03.08.584168

22. Steiner A, Schlepckow K, Brunner B, Steiner H, Haass C, Hagn F. γ-Secretase cleavage of the Alzheimer risk factor TREM 2 is determined by its intrinsic structural dynamics . EMBO J. 2020 Oct 15;39(20).

23. Cantoni C, Bollman B, Licastro D, Xie M, Mikesell R, Schmidt R, et al. TREM2 regulates microglial cell activation in response to demyelination in vivo. Acta Neuropathol. 2015 Feb 18;129(3):429–47.

24. Jay TR, Miller CM, Cheng PJ, Graham LC, Bemiller S, Broihier ML, et al. TREM2 deficiency eliminates TREM2+ inflammatory macrophages and ameliorates pathology in Alzheimer's disease mouse models. Journal of Experimental Medicine. 2015 Mar 9;212(3):287–95.

25. Damisah EC, Hill RA, Rai A, Chen F, Rothlin C V, Ghosh S, et al. Astrocytes and microglia play orchestrated roles and respect phagocytic territories during neuronal corpse removal in vivo [Internet]. 2020. Available from: https://www.science.org

26. Wei W, Zhang L, Xin W, Pan Y, Tatenhorst L, Hao Z, et al. TREM2 regulates microglial lipid droplet formation and represses post-ischemic brain injury. Biomedicine and Pharmacotherapy. 2024 Jan 1;170.

27. Poliani PL, Wang Y, Fontana E, Robinette ML, Yamanishi Y, Gilfillan S, et al. TREM2 sustains microglial expansion during aging and response to demyelination. Journal of Clinical Investigation. 2015 May 1;125(5):2161–70.

28. Winfree RL, Seto M, Dumitrescu L, Menon V, De Jager P, Wang Y, et al. TREM2 gene expression associations with Alzheimer's disease neuropathology are region-specific: implications for cortical versus subcortical microglia. Acta Neuropathol. 2023 Jun 1;145(6):733–47.

29. Butovsky O, Weiner HL. Microglial signatures and their role in health and disease. Vol. 19, Nature Reviews Neuroscience. Nature Publishing Group; 2018. p. 622–35.

30. Masuda T, Sankowski R, Staszewski O, Böttcher C, Amann L, Sagar, et al. Spatial and temporal heterogeneity of mouse and human microglia at single-cell resolution. Nature. 2019 Feb 21;566(7744):388–92.

31. Krasemann S, Madore C, Cialic R, Baufeld C, Calcagno N, El Fatimy R, et al. The TREM2-APOE Pathway Drives the Transcriptional Phenotype of Dysfunctional Microglia in Neurodegenerative Diseases. Immunity. 2017 Sep 19;47(3):566-581.e9.

32. Haure-Mirande JV, Audrain M, Ehrlich ME, Gandy S. Microglial TYROBP/DAP12 in Alzheimer's disease: Transduction of physiological and pathological signals across TREM2. Vol. 17, Molecular Neurodegeneration. BioMed Central Ltd; 2022.

33. McQuade A, Kang YJ, Hasselmann J, Jairaman A, Sotelo A, Coburn M, et al. Gene expression and functional deficits underlie TREM2-knockout microglia responses in human models of Alzheimer's disease. Nat Commun. 2020 Dec 1;11(1).

34. Filipello F, Morini R, Corradini I, Zerbi V, Canzi A, Michalski B, et al. The Microglial Innate Immune Receptor TREM2 Is Required for Synapse Elimination and Normal Brain Connectivity. Immunity. 2018 May 15;48(5):979-991.e8.

35. Mazaheri F, Snaidero N, Kleinberger G, Madore C, Daria A, Werner G, et al. TREM 2 deficiency impairs chemotaxis and microglial responses to neuronal injury . EMBO Rep. 2017 Jul;18(7):1186–98.

36. Diaz-Aparicio I, Paris I, Sierra-Torre V, Plaza-Zabala A, Rodríguez-Iglesias N, Márquez-Ropero M, et al. Microglia actively remodel adult hippocampal neurogenesis through the phagocytosis secretome. Journal of Neuroscience. 2020 Feb 12;40(7):1453–82.

37. Dantas PH dos S, Costa VAF, Felice AG, Sousa EG, de Oliveira Matos A, de Castro Soares S, et al. Exploring the orphan immune receptor TREM2 and its non-protein ligands: In silico characterization. Chem Phys Lipids. 2025 Jan 1;266.

38. Kober DL, Brett TJ. TREM2-Ligand Interactions in Health and Disease. Vol. 429, Journal of Molecular Biology. Academic Press; 2017. p. 1607–29.

39. Wang Y, Cella M, Mallinson K, Ulrich JD, Young KL, Robinette ML, et al. TREM2 lipid sensing sustains the microglial response in an Alzheimer's disease model. Cell. 2015 Mar 15;160(6):1061–71.

40. Zhao Y, Wu X, Li X, Jiang LL, Gui X, Liu Y, et al. TREM2 Is a Receptor for β-Amyloid that Mediates Microglial Function. Neuron. 2018 Mar 7;97(5):1023-1031.e7.

41. Fioretto L, Ziaco M, Nuzzo G, Albiani F, Saponaro M, Carbone D, et al. Small molecules as ligands in the tuning of immune regulatory receptors. Vol. 16, Frontiers in Immunology. Frontiers Media SA; 2025.

42. Daws MR, Sullam PM, Niemi EC, Chen TT, Tchao NK, Seaman WE. Pattern Recognition by TREM-2: Binding of Anionic Ligands. The Journal of Immunology. 2003 Jul 15;171(2):594–9.

43. Quan DN, Cooper MD, Potter JL, Roberts MH, Cheng H, Jarvis GA. TREM-2 binds to lipooligosaccharides of Neisseria gonorrhoeae and is expressed on reproductive tract epithelial cells. Mucosal Immunol. 2008;1(3):229–38.

44. Cannon JP, O'Driscoll M, Litman GW. Specific lipid recognition is a general feature of CD300 and TREM molecules. Immunogenetics. 2012 Jan;64(1):39–47.

45. Kawabori M, Kacimi R, Kauppinen T, Calosing C, Kim JY, Hsieh CL, et al. Triggering receptor expressed on myeloid cells 2 (TREM2) deficiency attenuates phagocytic activities of microglia and exacerbates ischemic damage in experimental stroke. Journal of Neuroscience. 2015;35(8):3384–96.

46. Charles JF, Humphrey MB, Zhao X, Quarles E, Nakamura MC, Aderem A, et al. The innate immune response to Salmonella enterica serovar typhimurium by macrophages is dependent on TREM2-DAP. Infect Immun. 2008 Jun;76(6):2439–47.

47. Atagi Y, Liu CC, Painter MM, Chen XF, Verbeeck C, Zheng H, et al. Apolipoprotein E is a ligand for triggering receptor expressed on myeloid cells 2 (TREM2). Journal of Biological Chemistry. 2015 Oct 23;290(43):26043–50.

48. Lessard CB, Malnik SL, Zhou Y, Ladd TB, Cruz PE, Ran Y, et al. High-affinity interactions and signal transduction between Aβ oligomers and TREM 2 . EMBO Mol Med. 2018 Nov;10(11).

49. Phongsisay V, Iizasa E, Hara H, Yamasaki S. 3-O-sulfo-β-d-galactose moiety of endogenous sulfoglycolipids is a potential ligand for immunoglobulin-like receptor LMIR5. Mol Immunol. 2015 Feb 1;63(2):595–9.

50. Gallo C, Manzo E, Barra G, Fioretto L, Ziaco M, Nuzzo G, et al. Sulfavant A as the first synthetic TREM2 ligand discloses a homeostatic response of dendritic cells after receptor engagement. Cellular and Molecular Life Sciences [Internet]. 2022 Jul 20;79(7):369. Available from: https://link.springer.com/10.1007/s00018-022-04297-z

51. Barra G, Gallo C, Carbone D, Ziaco M, Dell'Isola M, Affuso M, et al. The immunoregulatory effect of the TREM2-agonist Sulfavant A in human allogeneic mixed lymphocyte reaction. Front Immunol. 2023;14.

52. Wang H, Liu D, Zhou X. Effect of Mycolic Acids on Host Immunity and Lipid Metabolism. Vol. 25, International Journal of Molecular Sciences. Multidisciplinary Digital Publishing Institute (MDPI); 2024.

53. Iizasa E, Chuma Y, Uematsu T, Kubota M, Kawaguchi H, Umemura M, et al. TREM2 is a receptor for non-glycosylated mycolic acids of mycobacteria that limits anti-mycobacterial macrophage activation. Nat Commun. 2021 Dec 1;12(1).

54. Xue T, Ji J, Sun Y, Huang X, Cai Z, Yang J, et al. Sphingosine-1-phosphate, a novel TREM2 ligand, promotes microglial phagocytosis to protect against ischemic brain injury. Acta Pharm Sin B. 2022 Apr 1;12(4):1885–98.

55. Deczkowska A, Weiner A, Amit I. The Physiology, Pathology, and Potential Therapeutic Applications of the TREM2 Signaling Pathway. Vol. 181, Cell. Cell Press; 2020. p. 1207–17.

56. Lee-Gosselin A, Jury-Garfe N, You Y, Dabin L, Soni D, Dutta S, et al. TREM2-Deficient Microglia Attenuate Tau Spreading In Vivo. Cells. 2023 Jun 1;12(12).

57. Mai Z, Wei W, Yu H, Chen Y, Wang Y, Ding Y. Molecular recognition of the interaction between ApoE and the TREM2 protein. Transl Neurosci. 2022 Jan 1;13(1):93–103.

58. Gallo C, Verrillo L, Manzo E, Cauzzi E, La Barbera L, Sabatino G, De Paolis M.L, et al. Microglial clereance, neuroprotection and cognitive recovery via a novel synthetic sulfolipid in Alzheimer's disease. Molecular Neurodegeneration. 2025 (in press)

59. Schauer SP, Cho CH, Novikova G, Roth GA, Lee J, Sharma AD, et al. Primate cerebrospinal fluid CHI3L1 reflects brain TREM2 agonism. Alzheimer's and Dementia. 2024 Sep 1;20(9):5861–88.

60. Schlepckow K, Monroe KM, Kleinberger G, Cantuti-Castelvetri L, Parhizkar S, Xia D, et al. Enhancing protective microglial activities with a dual function TREM 2 antibody to the stalk region . EMBO Mol Med. 2020 Apr 7;12(4).

61. van Lengerich B, Zhan L, Xia D, Chan D, Joy D, Park JI, et al. A TREM2-activating antibody with a blood–brain barrier transport vehicle enhances microglial metabolism in Alzheimer's disease models. Nat Neurosci. 2023 Mar 1;26(3):416–29.

62. Long H, Simmons A, Mayorga A, Burgess B, Nguyen T, Budda B, et al. Preclinical and first-in-human evaluation of AL002, a novel TREM2 agonistic antibody for Alzheimer's disease. Alzheimer's Research and Therapy . 2024 Dec 1;16(1).

63. Alector Presents Baseline Characteristics for INVOKE-2 Phase 2 Clinical Trial of AL002 at the Alzheimer's Association International Conference® 2024 (AAIC®) [Internet]. 2024. Available from: www.alector.com.

64. Mirescu C. Characterization of the first TREM2 small molecule agonist, VG-3927, for clinical development in Alzheimer's disease. Alzheimer's & Dementia. 2024 Dec;20(S6).

65. Yuan S, El Gaamouch F, Cho S, Kuncewicz K, Nada H, Gabr MT. Discovery of a Small Molecule TREM2 Agonist with Improved In Vitro Pharmacokinetic Profile and Validated Target Engagement. ACS Med Chem Lett. 2025 Aug 14;16(8):1634–40.

66. Cho S, Kaur B, Lam K, Gaamouch F El, Kuncewicz K, Doering NP, et al. Structure-Based Virtual Screening Identifies TREM2-Targeted Small Molecules that Enhance Microglial Phagocytosis [Internet]. 2025. Available from: http://biorxiv.org/lookup/doi/10.1101/2025.08.23.671917

67. Cho S, Gaamouch F El, Upadhyay S, Nada H, Kuncewicz K, Gabr MT. As48, a First-in-Class Dual-Function TREM2 Modulator: Receptor Activation and Shedding Inhibition [Internet]. 2025. Available from: http://biorxiv.org/lookup/doi/10.1101/2025.08.23.671919

68. Jiao Y, Yang L, Wang R, Song G, Fu J, Wang J, et al. Drug Delivery Across the Blood–Brain Barrier: A New Strategy for the Treatment of Neurological Diseases. Vol. 16, Pharmaceutics. Multidisciplinary Digital Publishing Institute (MDPI); 2024.

69. Ulrich JD, Ulland TK, Colonna M, Holtzman DM. Elucidating the Role of TREM2 in Alzheimer's Disease. Vol. 94, Neuron. Cell Press; 2017. p. 237–48.

70. Sigalov AB. SCHOOL of nature: ligand-independent immunomodulatory peptides. Vol. 25, Drug Discovery Today. Elsevier Ltd; 2020. p. 1298–306.

71. Sigalov AB. Inhibition of TREM-2 Markedly Suppresses Joint Inflammation and Damage in Experimental Arthritis. Int J Mol Sci. 2022 Aug 1;23(16).

72. Zhong J, Xing X, Gao Y, Pei L, Lu C, Sun H, et al. Distinct roles of TREM2 in central nervous system cancers and peripheral cancers. Cancer Cell. 2024 Jun 10;42(6):968-984.e9.

73. Dello Russo C, Cappoli N, Coletta I, Mezzogori D, Paciello F, Pozzoli G, et al. The human microglial HMC3 cell line: Where do we stand? A systematic literature review. Vol. 15, Journal of Neuroinflammation. BioMed Central Ltd.; 2018.

74. Datta R, Heaster TM, Sharick JT, Gillette AA, Skala MC. Fluorescence lifetime imaging microscopy: fundamentals and advances in instrumentation, analysis, and applications. J Biomed Opt. 2020 May 13;25(07):1.

75. Götz A, Scharnagl C. Dissecting conformational changes in app's transmembrane domain linked to ε-efficiency in familial Alzheimer's disease. PLoS One. 2018 Jul 1;13(7).

76. Micsonai A, Wien F, Murvai N, Nyiri MP, Balatoni B, Lee YH, et al. BeStSel: Analysis site for protein CD spectra - 2025 update. Nucleic Acids Res. 2025 Jul 7;53(W1):W73–83.

77. Reed J, Reed TA. A Set of Constructed Type Spectra for the Practical Estimation of Peptide Secondary Structure from Circular Dichroism. Vol. 254, ANALYTICAL BIOCHEMISTRY. 1997.

78. Wu Y, Huang HW, Olah GA. Method of oriented circular dichroism.

79. Bürck J, Wadhwani P, Fanghänel S, Ulrich AS. Oriented Circular Dichroism: A Method to Characterize Membrane-Active Peptides in Oriented Lipid Bilayers. Acc Chem Res. 2016 Feb 16;49(2):184–92.

80. Bürck J, Roth S, Wadhwani P, Afonin S, Kanithasen N, Strandberg E, et al. Conformation and membrane orientation of amphiphilic helical peptides by oriented circular dichroism. Biophys J. 2008 Oct 15;95(8):3872–81.

81. Yao Y, Ugras TJ, Meyer T, Dykes M, Wang D, Arbe A, et al. Extracting Pure Circular Dichroism from Hierarchically Structured CdS Magic Cluster Films. ACS Nano. 2022 Dec 27;16(12):20457–69.

82. Schweigardt F, Strandberg E, Wadhwani P, Reichert J, Bürck J, Cravo HLP, et al. Membranolytic Mechanism of Amphiphilic Antimicrobial β-Stranded [KL]n Peptides. Biomedicines. 2022 Sep 1;10(9).

83. Klukowski P, Riek R, Guntert P. NMRtist: An online platform for automated biomolecular NMR spectra analysis. Bioinformatics. 2023 Feb 1;39(2).

84. Canadian Journal of Biochemistry and Physiology Issued by THE NATIONAL RESEARCH COUNCIL OF CANADA A RAPID METHOD OF TOTAL LIPID EXTRACTION AND PURIFICATION1.

85. Breil C, Abert Vian M, Zemb T, Kunz W, Chemat F. “Bligh and Dyer” and Folch methods for solid–liquid–liquid extraction of lipids from microorganisms. Comprehension of solvatation mechanisms and towards substitution with alternative solvents. Int J Mol Sci. 2017 Apr 1;18(4).

86. Schmid R, Heuckeroth S, Korf A, Smirnov A, Myers O, Dyrlund TS, et al. Integrative analysis of multimodal mass spectrometry data in MZmine 3. Vol. 41, Nature Biotechnology. Nature Research; 2023. p. 447–9.

87. McMullin DR, Hoogstra S, McDonald KP, Sumarah MW, Renaud JB. Natural Product Discovery with LC-MS/MS Diagnostic Fragmentation Filtering: Application for Microcystin Analysis. Journal of Visualized Experiments. 2019 May 1;2019(147).

88. Nuzzo G, Gallo C, D’Ippolito G, Manzo E, Ruocco N, Russo E, et al. UPLC–MS/MS identification of sterol sulfates in marine diatoms. Mar Drugs. 2019;17(1).

89. Okazaki Y, Otsuki H, Narisawa T, Kobayashi M, Sawai S, Kamide Y, et al. A new class of plant lipid is essential for protection against phosphorus depletion. Nat Commun. 2013;4.

90. Popov RS, Ivanchina N V., Silchenko AS, Avilov SA, Kalinin VI, Malyarenko T V., et al. A Mass Spectrometry Database for Sea Cucumber Triterpene Glycosides. Metabolites. 2023 Jul 1;13(7).

91. Ma Y, Kind T, Yang D, Leon C, Fiehn O. MS2Analyzer: A software for small molecule substructure annotations from accurate tandem mass spectra. Anal Chem. 2014 Sep 28;86(21):10724–31.

92. Jackson SN, Wang HYJ, Woods AS. In Situ Structural Characterization of Glycerophospholipids and Sulfatides in Brain Tissue Using MALDI-MS/MS. J Am Soc Mass Spectrom. 2007 Jan;18(1):17–26.

93. Hsu FF, Turk J. Studies on sulfatides by quadrupole ion-trap mass spectrometry with electrospray ionization: Structural characterization and the fragmentation processes that include an unusual internal galactose residue loss and the classical charge-remote fragmentation. J Am Soc Mass Spectrom. 2004 Apr;15(4):536–46.

94. Hořejší K, Holčapek M. Unraveling the complexity of glycosphingolipidome: the key role of mass spectrometry in the structural analysis of glycosphingolipids. Vol. 416, Analytical and Bioanalytical Chemistry. Springer Science and Business Media Deutschland GmbH; 2024. p. 5403–21.

95. Goto-Inoue N, Hayasaka T, Zaima N, Setou M. The specific localization of seminolipid molecular species on mouse testis during testicular maturation revealed by imaging mass spectrometry. Glycobiology. 2009;19(9):950–7.

96. Alvarez JG, Storey BT, Hemling ML, Grob RL. High-resolution proton nuclear magnetic resonance characterization of seminolipid from bovine spermatozoa. J Lipid Res. 1990;31(6):1073–81.

97. Flynn TJ, Deshmukh~ DS, Rao GS, Pieringer RA. BIOCHEMICAL AND BIOPHYSICAL RESEARCH COMMUNICATIONS SULFOGALACTOSYL DIACYLGLYCEROL: OCCURRENCE AND BIOSYNTHESIS OF A NOVEL LIPID IN RAT BRAIN. Vol. 65. 1975.

98. Osetrova M, Tkachev A, Mair W, Guijarro Larraz P, Efimova O, Kurochkin I, et al. Lipidome atlas of the adult human brain. Nature Communications . 2024 Dec 1;15(1).

99. Pi J, Wu X, Feng Y. Fragmentation patterns of five types of phospholipids by ultra-high-performance liquid chromatography electrospray ionization quadrupole time-of-flight tandem mass spectrometry. Analytical Methods. 2016 Feb 14;8(6):1319–32.

100. Fischer J, Treblin M, Sitz T, Rohn S. Development of a targeted HPLC-ESI-QqQ-MS/MS method for the quantification of sulfolipids from a cyanobacterium, selected leafy vegetables, and a microalgae species. Available from: https://doi.org/10.1007/s00216-021-03164-3

101. Shirotani K, Hori Y, Yoshizaki R, Higuchi E, Colonna M, Saito T, et al. Aminophospholipids are signal-transducing TREM2 ligands on apoptotic cells. Sci Rep. 2019 Dec 1;9(1).

102. Sobota A, Strzelecka-Kiliszek A, Gładkowska E, Yoshida K, Mrozińska K, Kwiatkowska K. Binding of IgG-Opsonized Particles to FcγR Is an Active Stage of Phagocytosis That Involves Receptor Clustering and Phosphorylation. The Journal of Immunology. 2005 Oct 1;175(7):4450–7.

103. Li L, Zheng X, Ma H, Zhu M, Li X, Sun X, et al. TREM2 in Neurodegenerative Diseases: Mechanisms and Therapeutic Potential. Vol. 14, Cells. Multidisciplinary Digital Publishing Institute (MDPI); 2025.

104. Tan D, Konduri S, Erikci Ertunc M, Zhang P, Wang J, Chang T, et al. A class of anti-inflammatory lipids decrease with aging in the central nervous system. Nat Chem Biol. 2023 Feb 1;19(2):187–97.

105. Ziaco M, Fioretto L, Nuzzo G, Fontana A, Manzo E. Short gram-scale synthesis of sulfavant A. Org Process Res Dev. 2020 Nov 20;24(11):2728–33.

106. Kessner D, Chambers M, Burke R, Agus D, Mallick P. ProteoWizard: Open source software for rapid proteomics tools development. Bioinformatics. 2008;24(21):2534–6.

107. Manzo E, Gallo C, Fioretto L, Nuzzo G, Barra G, Pagano D, et al. Diasteroselective Colloidal Self-Assembly Affects the Immunological Response of the Molecular Adjuvant Sulfavant. ACS Omega. 2019 Apr 30;4(4):7807–14.

Appendix A

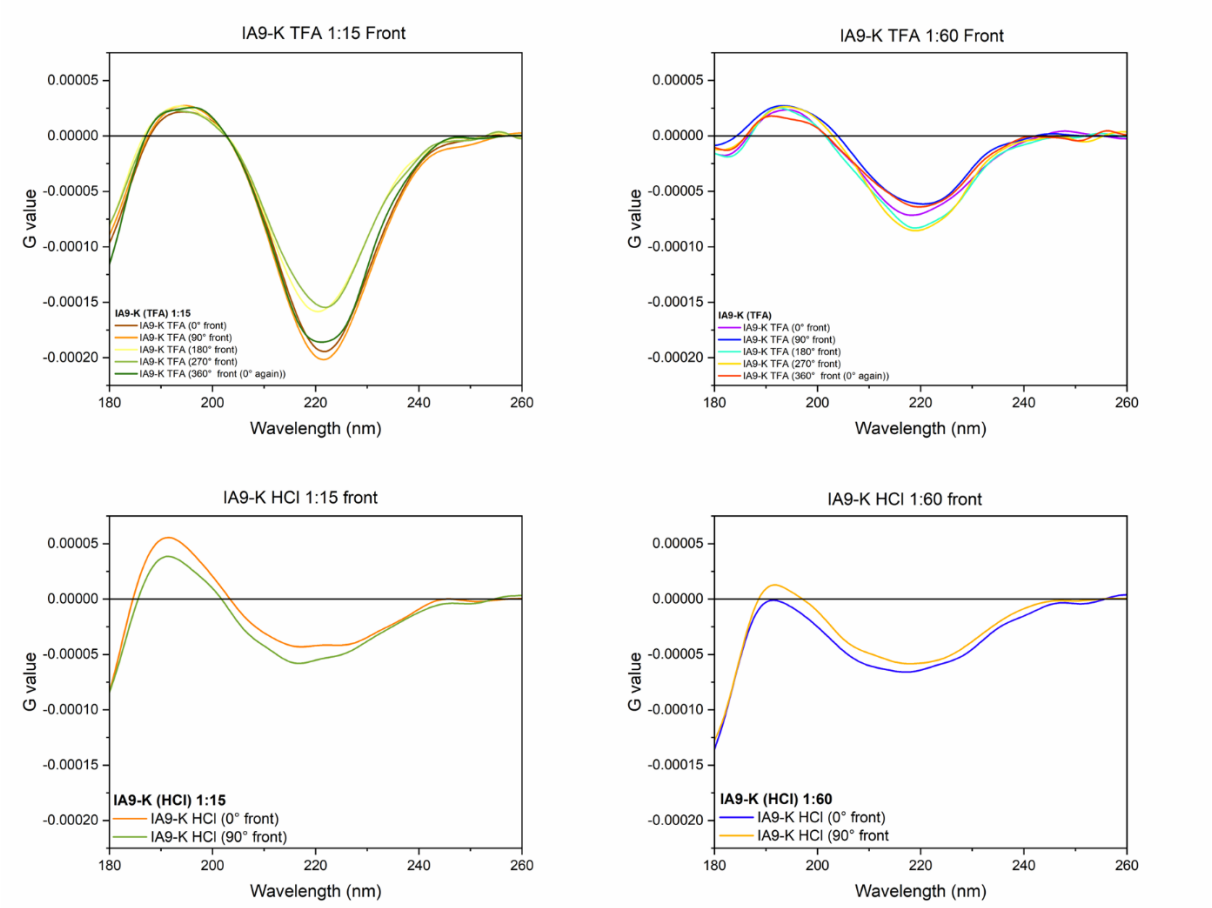

Figure 38 - Oriented circular dichroism (OCD) of IA9-K/TFA, IA9-K/HCl synthetic peptides recorded in DMPG/DMPC 1:3 at a 0-90° angle. Peptides were dissolved in $CHCl_3/CH_3OH$ (1:1, v/v) at a final concentration of 2.44 mg/mL. Spectra were collected in the 180–260 nm range and normalized as G-value.

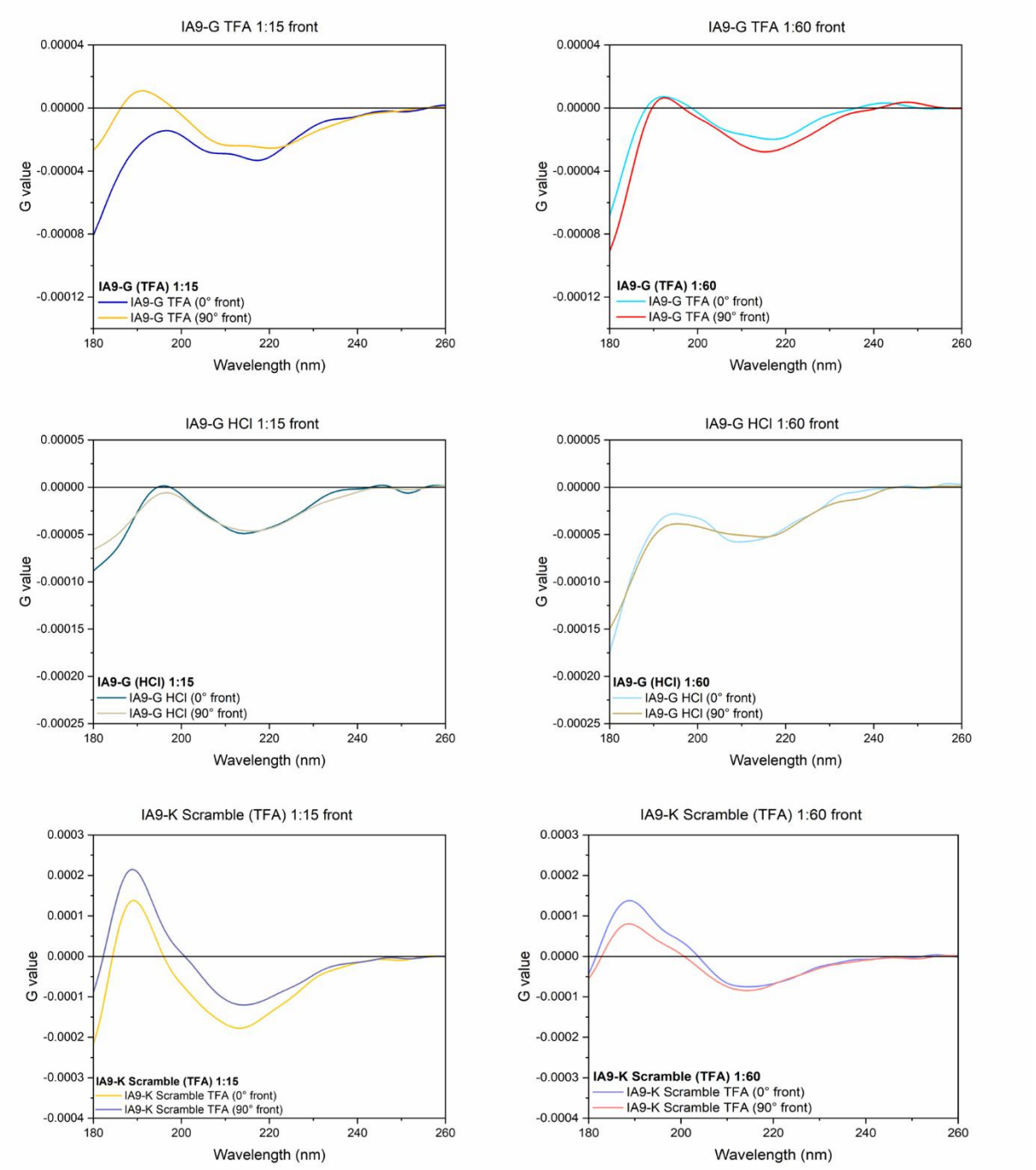

Figure 39 - Oriented circular dichroism (OCD) of IA9-K/TFA, IA9-K/HCl synthetic peptides recorded in DMPG/DMPC 1:3 at a 0-90° angle. Peptides were dissolved in $CHCl_3/CH_3OH$ (1:1, v/v) at a final concentration of 2.44 mg/mL. Spectra were collected in the 180–260 nm range and normalized as G-value.

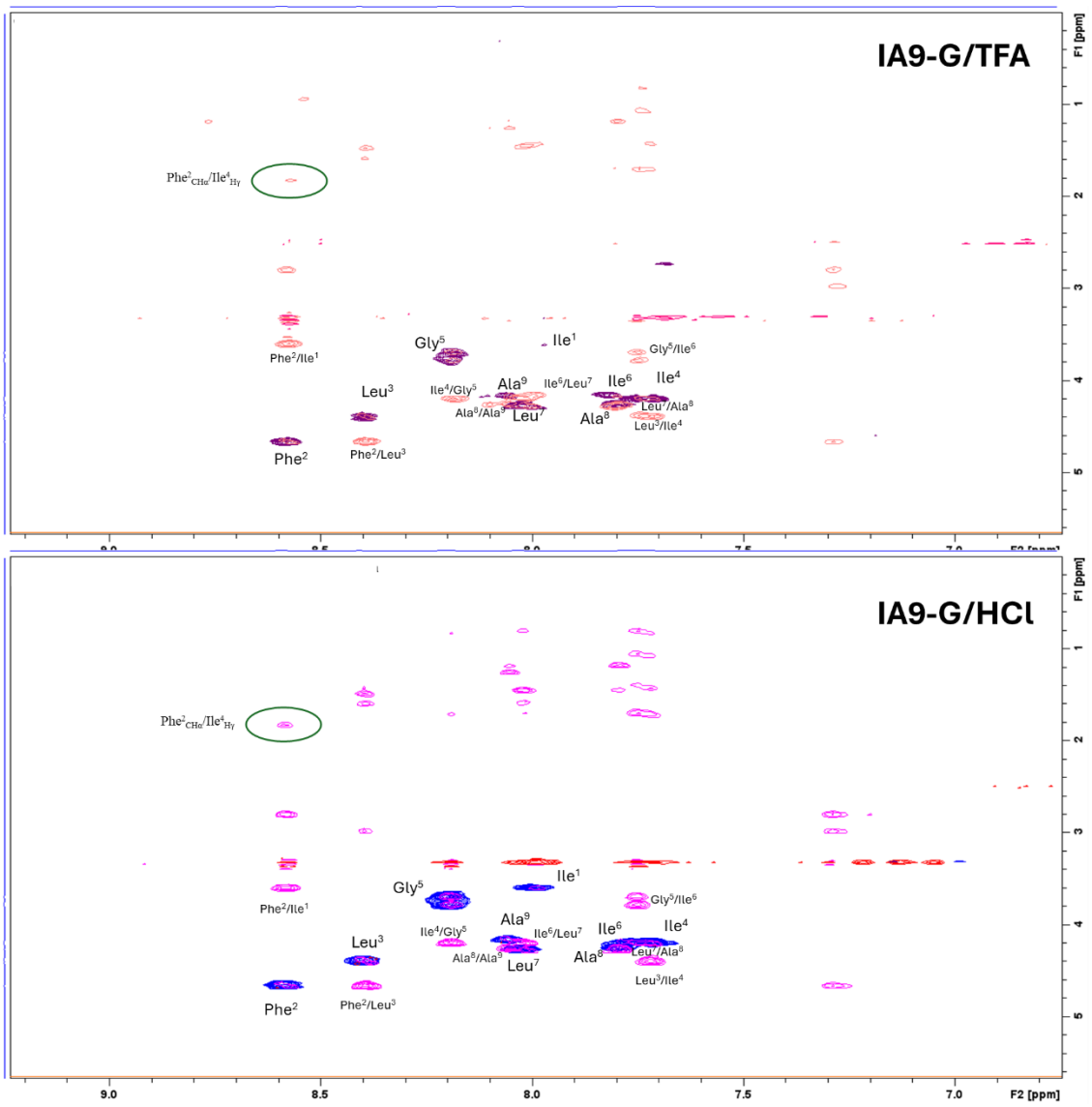

Figure 40 - Amide-resonance detail of COSY (purple in the upper panel, and blue in the lower panel) and ROESY (red in the upper panel, and magenta in the lower panel) 2D-NMR spectra of IA9-G peptides in 100% DMSO-D$_6$.

Precursor ions list (96.958 m/z)

425.26	863.56
465.30	864.62
641.41	865.57
767.50	866.58
778.51	874.61
781.48	876.59
793.51	877.61
795.53	878.60
804.53	879.62
806.50	880.62
807.49	886.61
808.56	887.56
809.51	888.62
819.53	890.64
820.52	892.62
821.54	902.60
822.54	904.62
823.56	905.64
835.53	906.63
847.56	908.65
849.58	910.60
850.57	912.62
851.59	914.64
860.55	918.67
861.54	919.62
862.61	920.65
	932.65
	934.67
	946.58

Figure 41 - Merged list of precursor ions obtained using the diagnostic fragment filter at 96.958 *m/z* in MZmine (Base Peak 20%, 95 best fragments).

Sulfatides

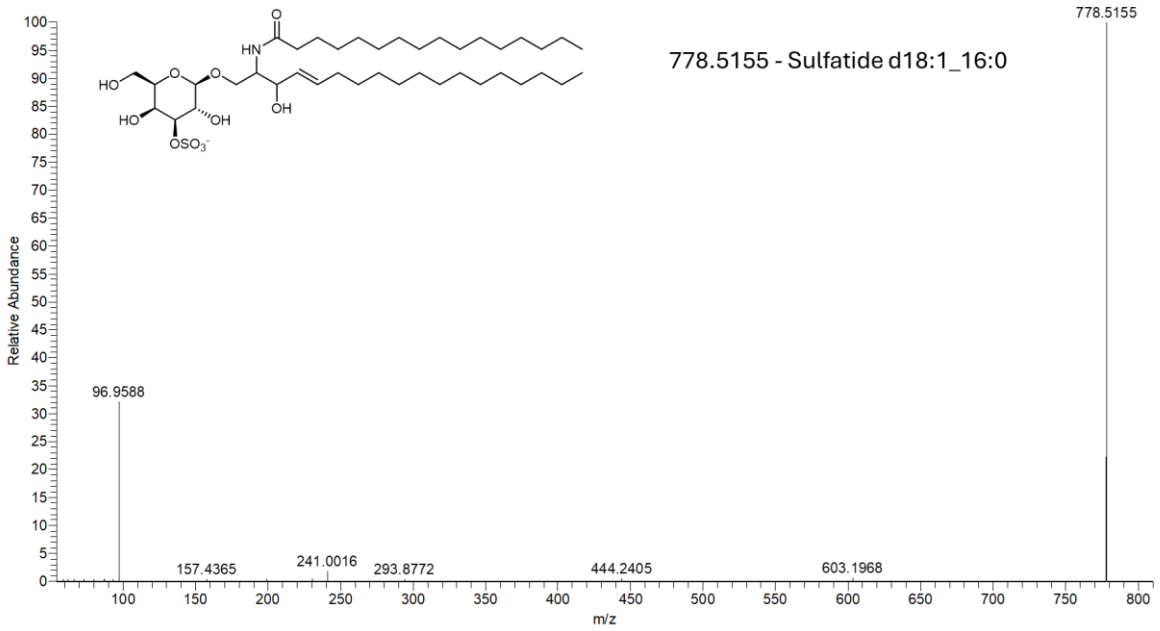

Figure 42 - MS/MS spectrum of sulfatide *m/z* 778.516 $[M–H]^-$ from mouse brain extract acquired in negative electrospray ionization (ESI–) using HCD at 35.0 eV.

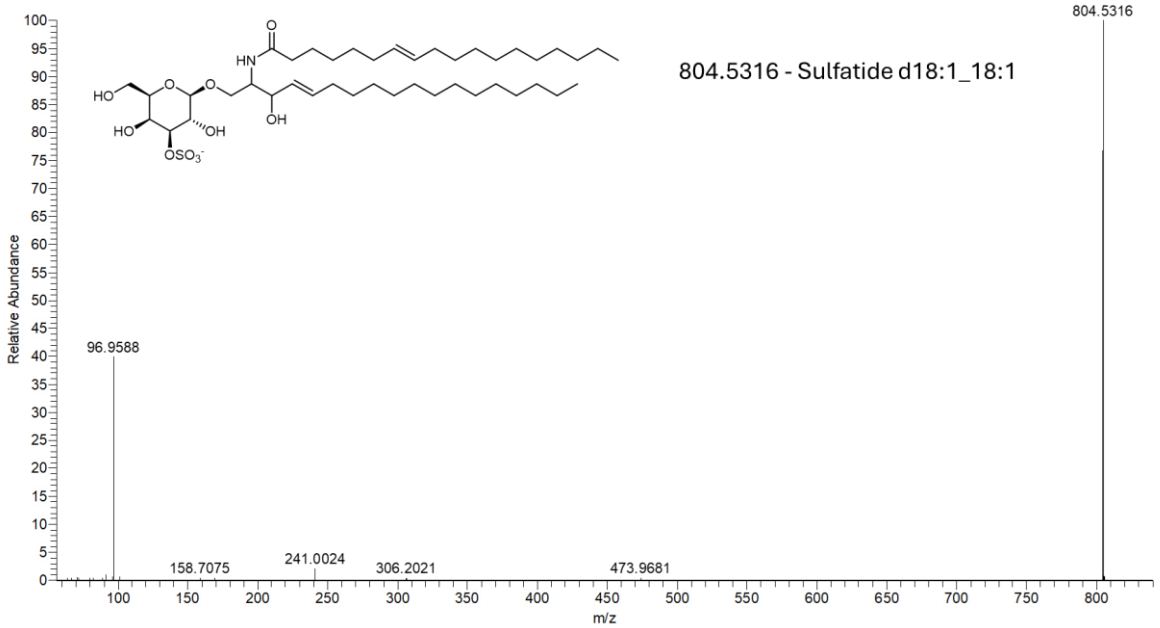

Figure 43 - MS/MS spectrum of sulfatide *m/z* 804.532 $[M–H]^-$ from mouse brain extract acquired in negative electrospray ionization (ESI–) using HCD at 35.0 eV.

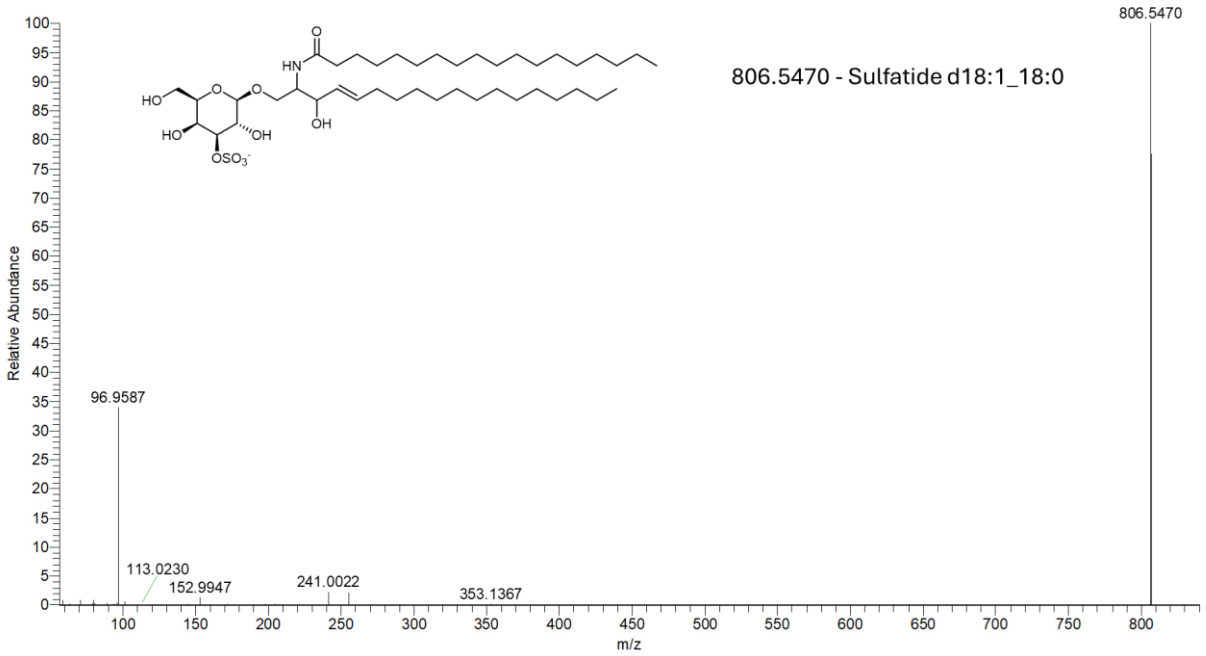

Figure 44 - MS/MS spectrum of sulfatide *m/z* 806.550 [M–H]⁻ from mouse brain extract acquired in negative electrospray ionization (ESI–) using HCD at 35.0 eV.

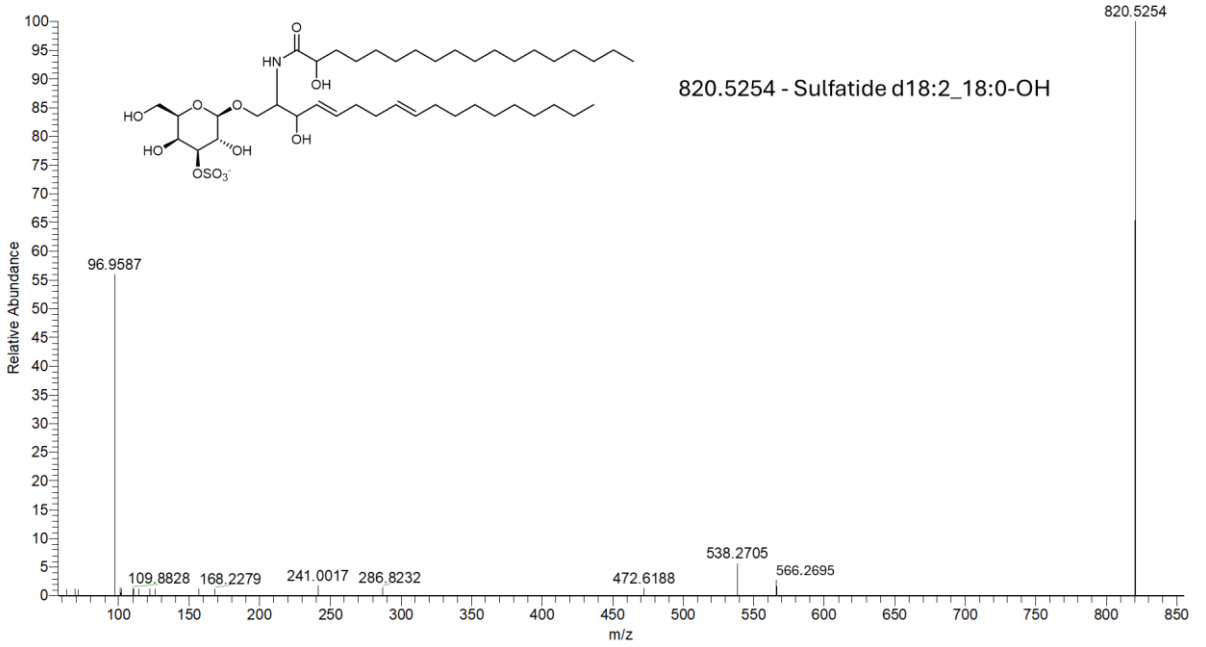

Figure 45 - MS/MS spectrum of sulfatide *m/z* 820.525 [M–H]⁻ from mouse brain extract acquired in negative electrospray ionization (ESI–) using HCD at 35.0 eV.

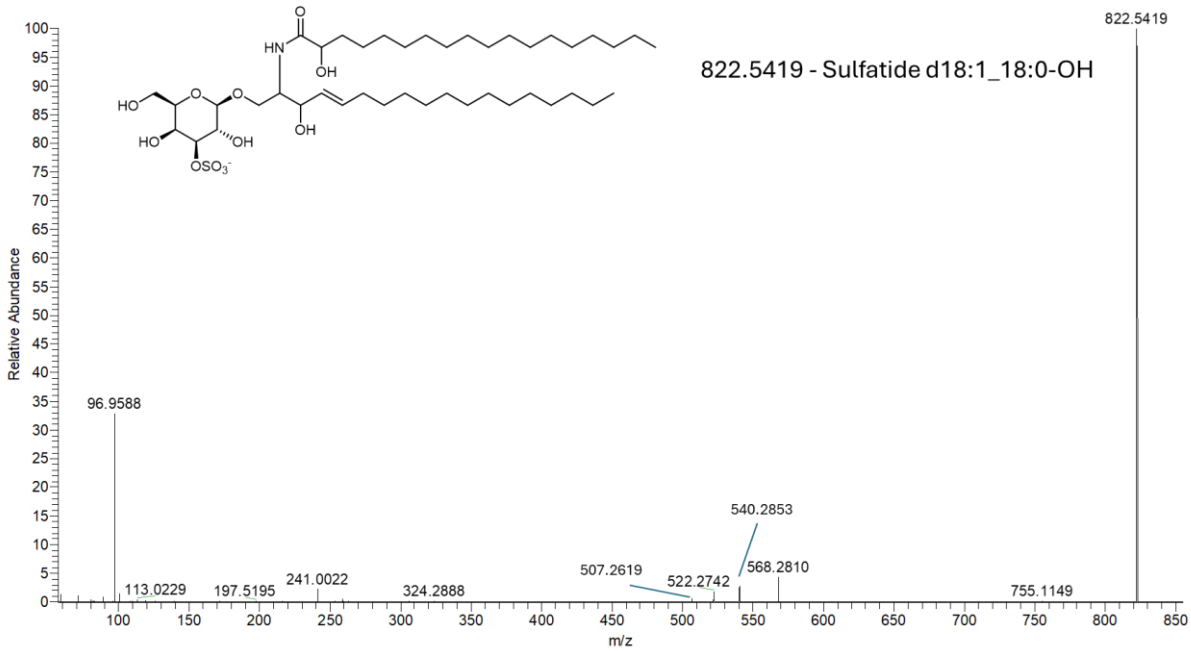

Figure 46 - MS/MS spectrum of sulfatide *m/z* 822.542 $[M–H]^-$ from mouse brain extract acquired in negative electrospray ionization (ESI–) using HCD at 35.0 eV.

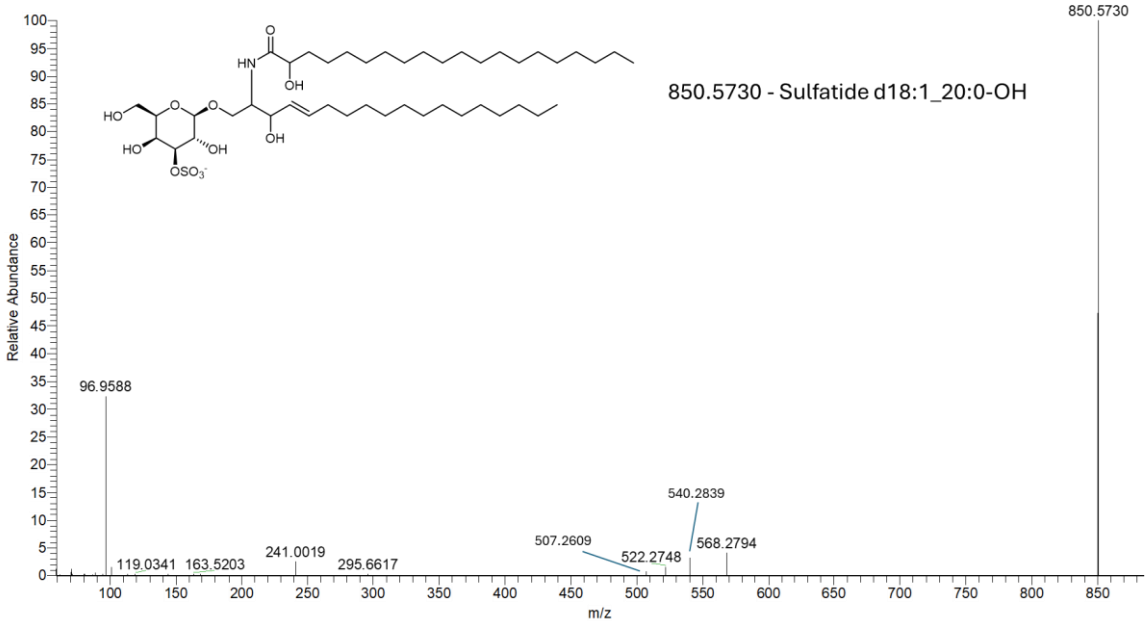

Figure 47 - MS/MS spectrum of sulfatide *m/z* 850.573 $[M–H]^-$ from mouse brain extract acquired in negative electrospray ionization (ESI–) using HCD at 35.0 eV.

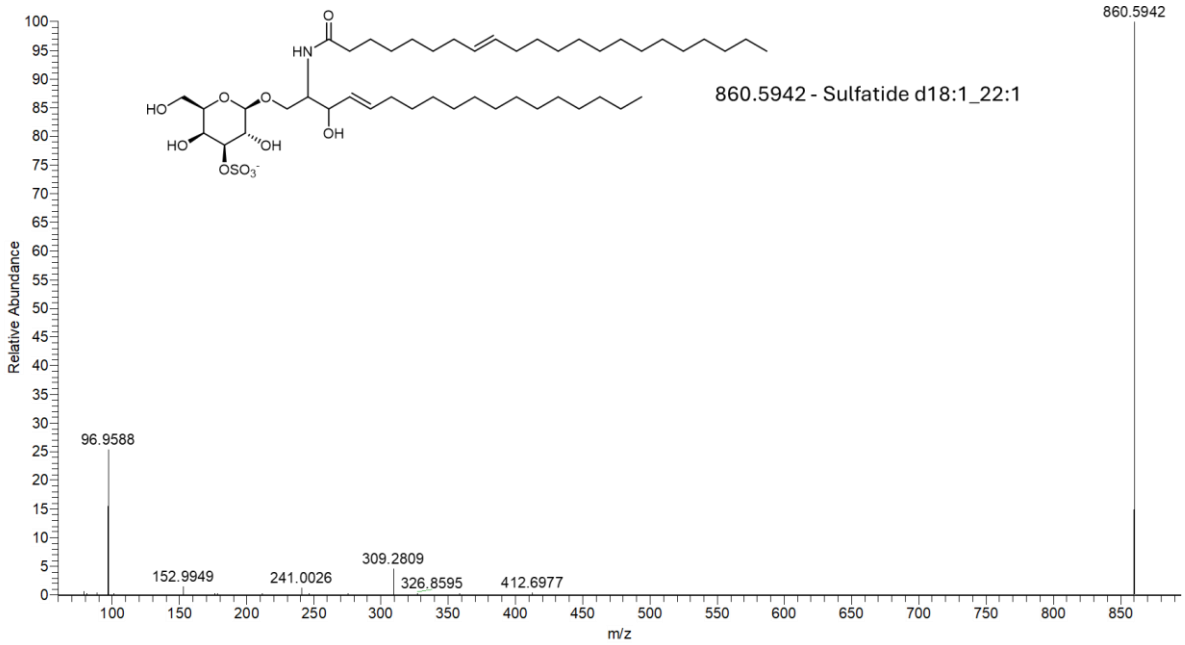

Figure 48 - MS/MS spectrum of sulfatide *m/z* 860.594 [M–H]⁻ from mouse brain extract acquired in negative electrospray ionization (ESI–) using HCD at 35.0 eV.

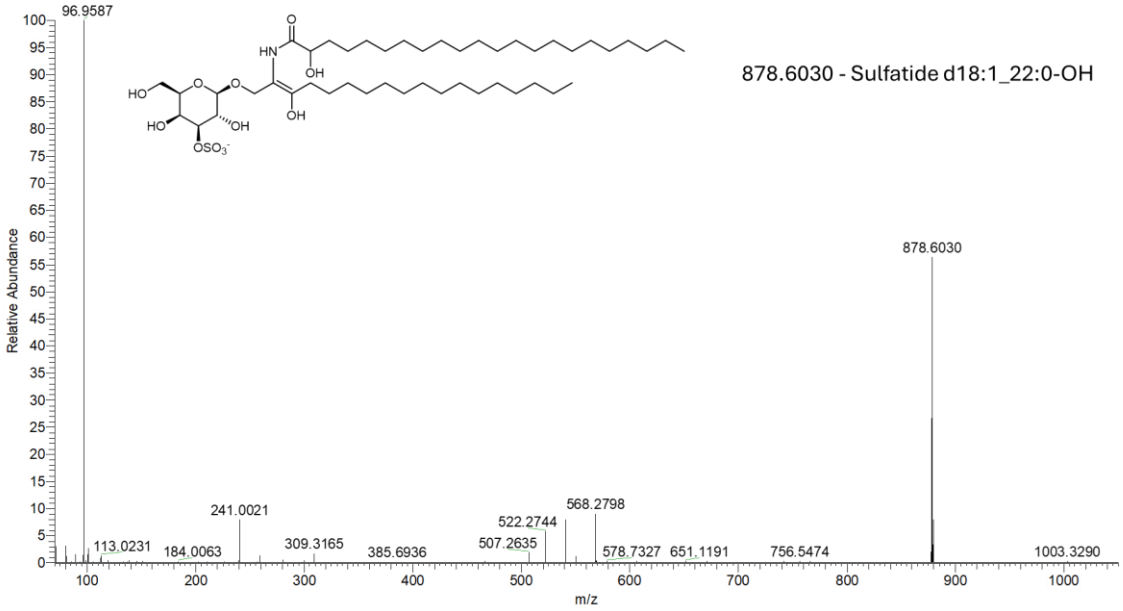

Figure 49 - MS/MS spectrum of the sulfatide *m/z* 878.6030 [M–H]- from manual inspection of fraction F obtained via silica gel separation, acquired in negative electrospray ionization (ESI⁻) using HCD at 42.0 eV.

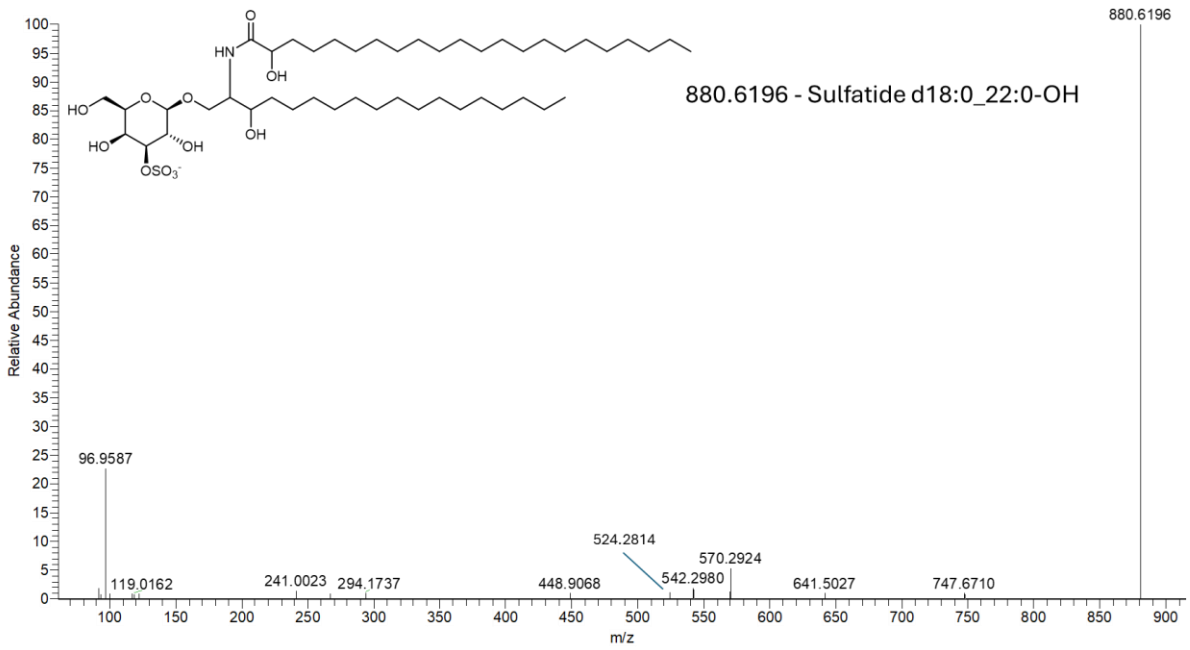

Figure 50 - MS/MS spectrum of sulfatide *m/z* 880.620 $[M–H]^-$ from mouse brain extract acquired in negative electrospray ionization (ESI–) using HCD at 35.0 eV.

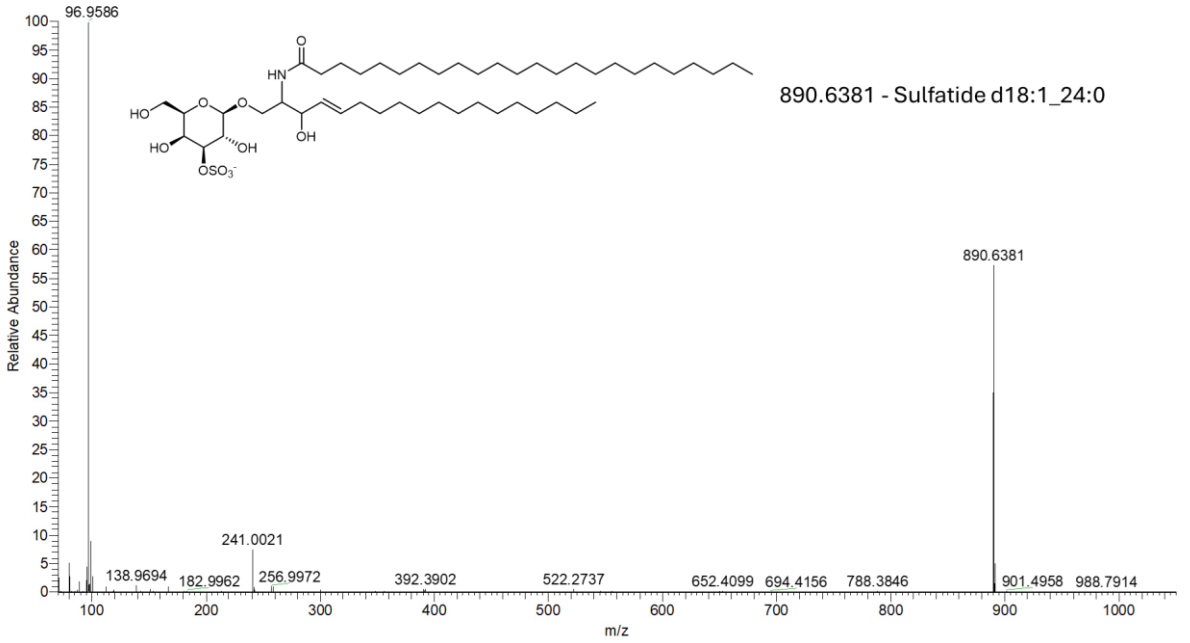

Figure 51 - MS/MS spectrum of sulfatide *m/z* 890.638 $[M–H]^-$ from mouse brain extract acquired in negative electrospray ionization (ESI–) using HCD at 35.0 eV.

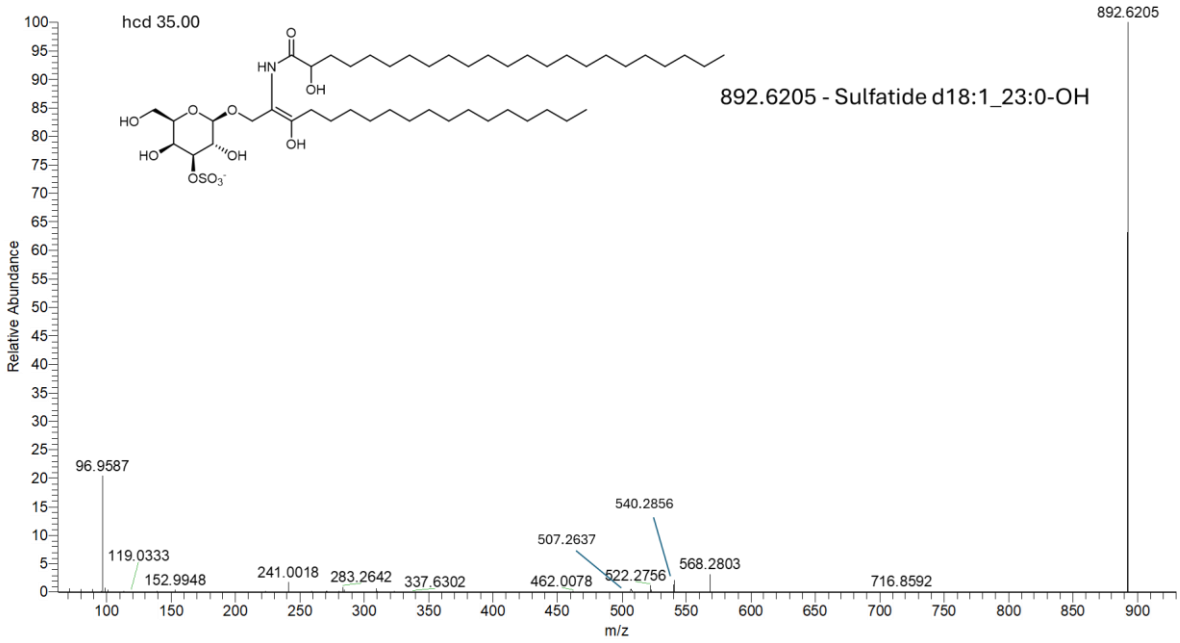

Figure 52 - MS/MS spectrum of sulfatide *m/z* 882.620 [M–H]⁻ from mouse brain extract acquired in negative electrospray ionization (ESI–) using HCD at 35.0 eV.

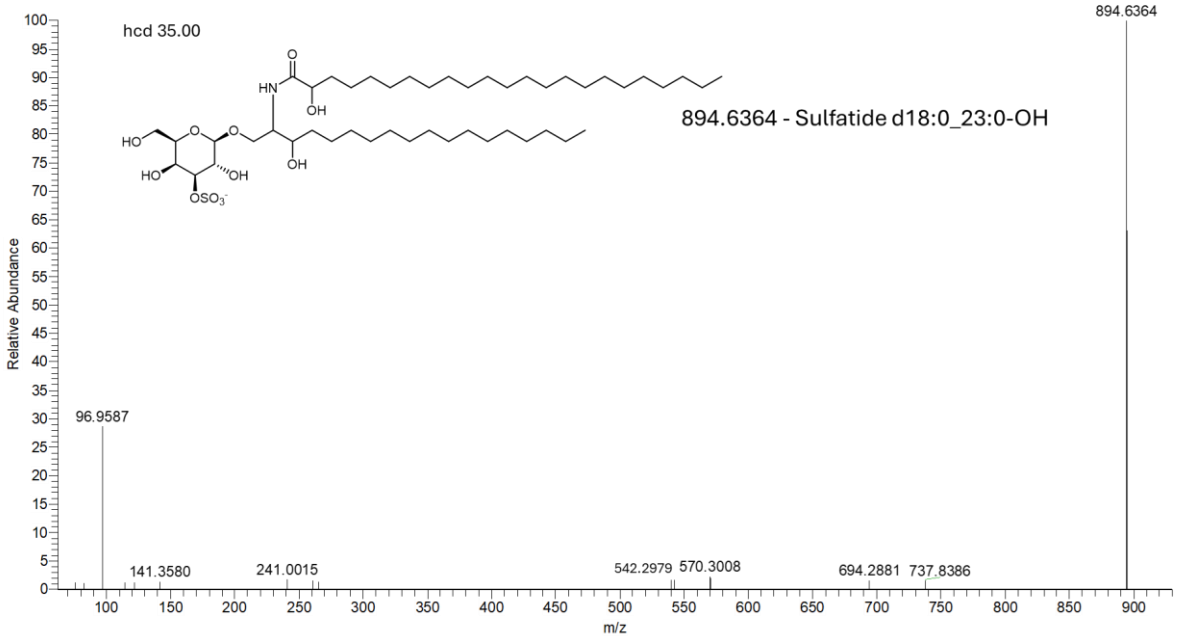

Figure 53 - MS/MS spectrum of sulfatide *m/z* 894.636 [M–H]⁻ from mouse brain extract acquired in negative electrospray ionization (ESI–) using HCD at 35.0 eV.

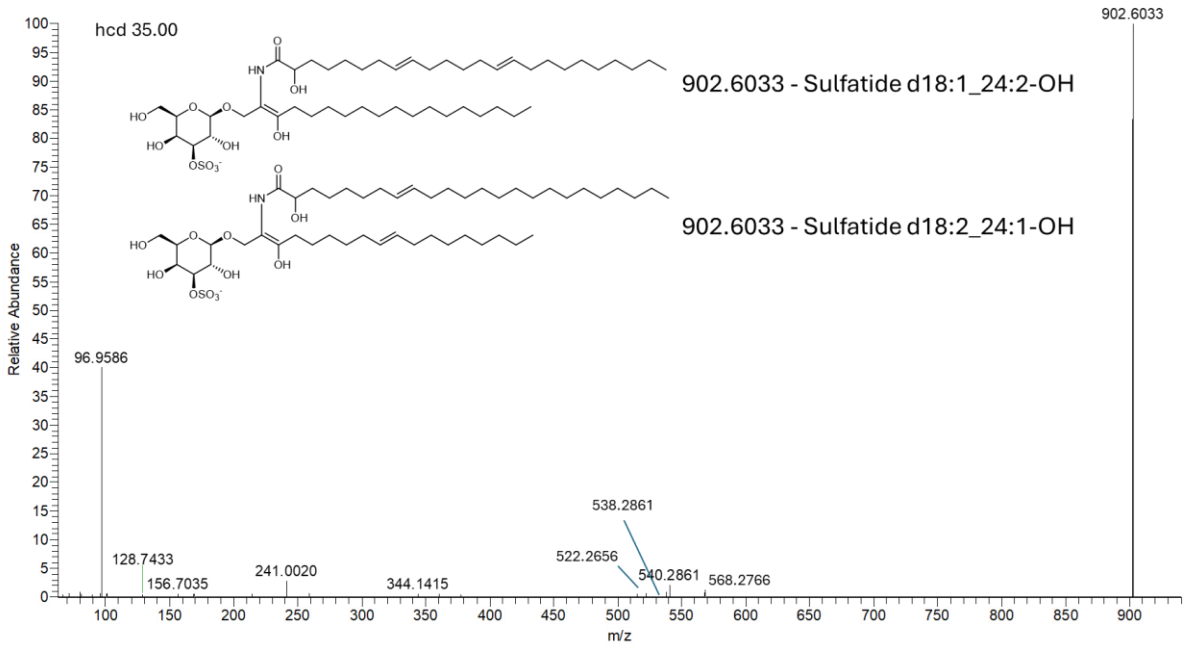

Figure 54 - MS/MS spectrum of sulfatide *m/z* 902.603 [M–H]⁻ from mouse brain extract acquired in negative electrospray ionization (ESI–) using HCD at 35.0 eV.

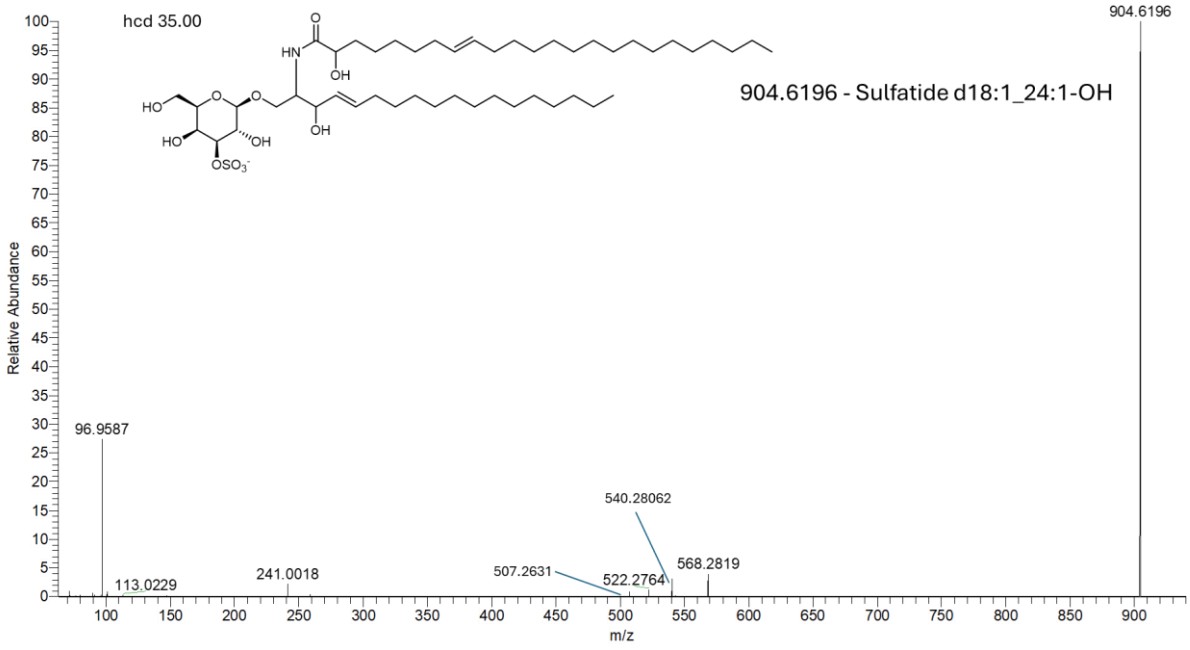

Figure 55 - MS/MS spectrum of sulfatide *m/z* 904.620 [M–H]⁻ from mouse brain extract acquired in negative electrospray ionization (ESI–) using HCD at 35.0 eV.

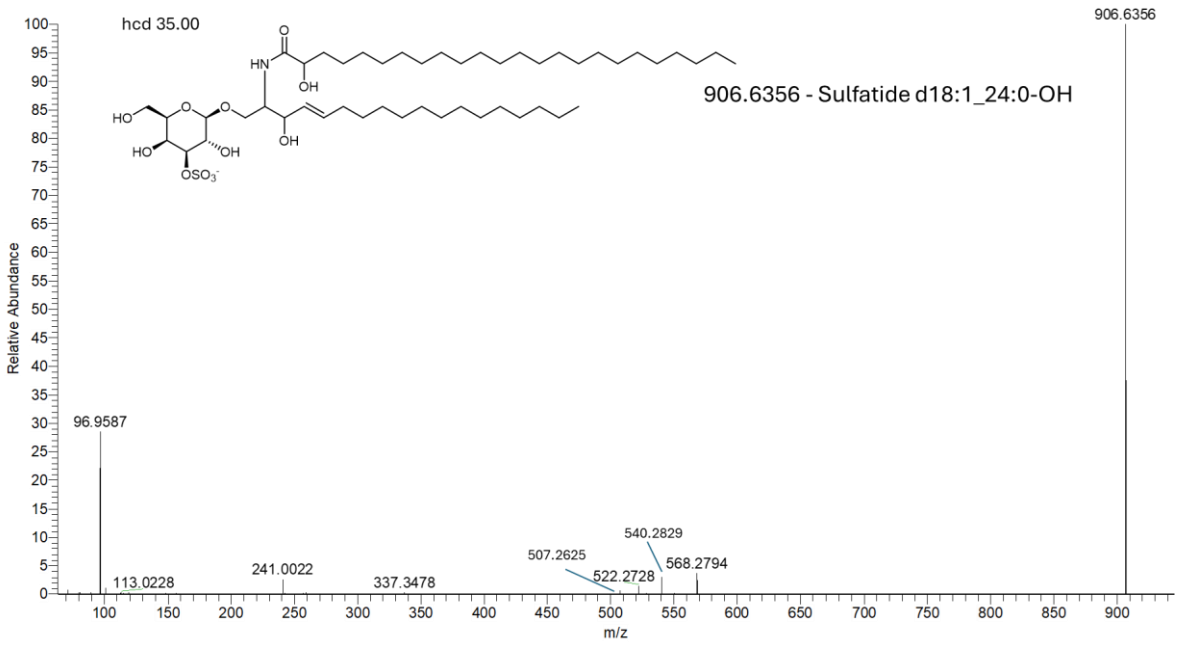

Figure 56 - MS/MS spectrum of sulfatide *m/z* 906.636 $[M–H]^-$ from mouse brain extract acquired in negative electrospray ionization (ESI–) using HCD at 35.0 eV.

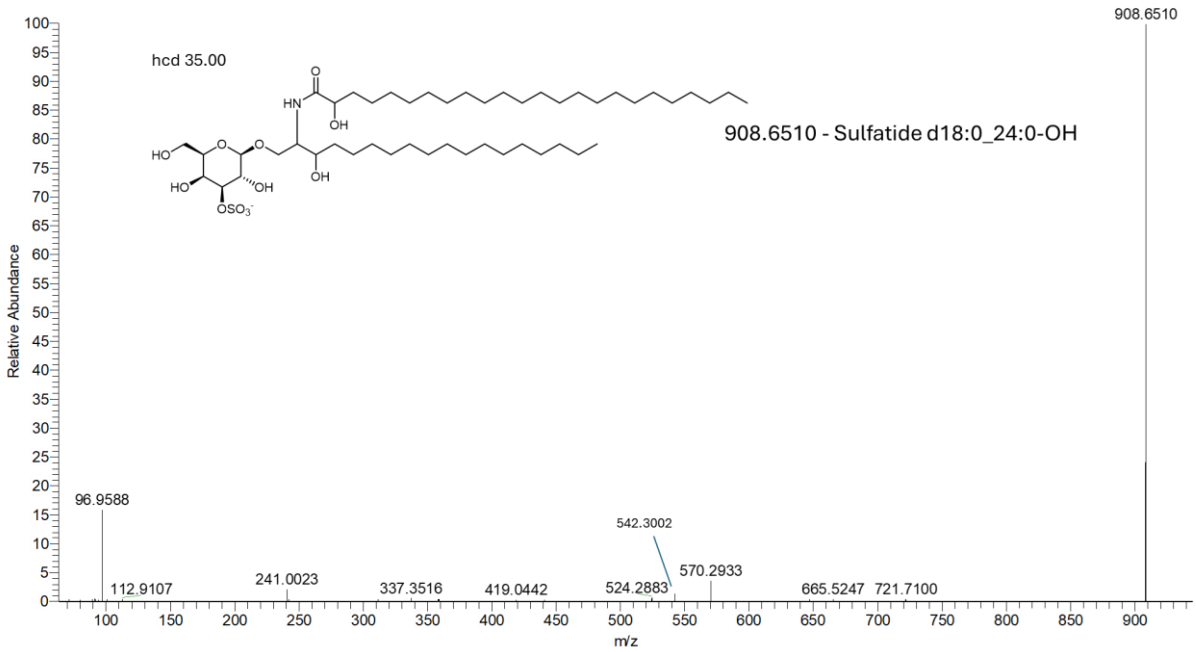

Figure 57 - MS/MS spectrum of sulfatide *m/z* 908.651 $[M–H]^-$ from mouse brain extract acquired in negative electrospray ionization (ESI–) using HCD at 35.0 eV.

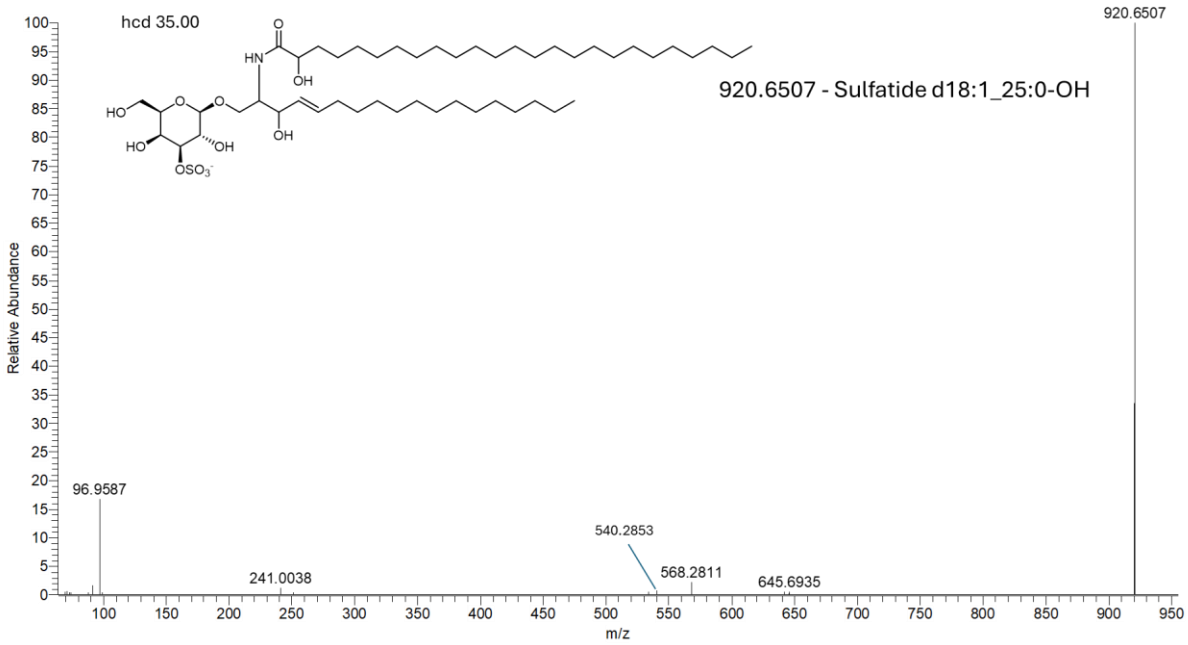

Figure 58 - MS/MS spectrum of sulfatide *m/z* 920.651 [M–H]⁻ from mouse brain extract acquired in negative electrospray ionization (ESI–) using HCD at 35.0 eV.

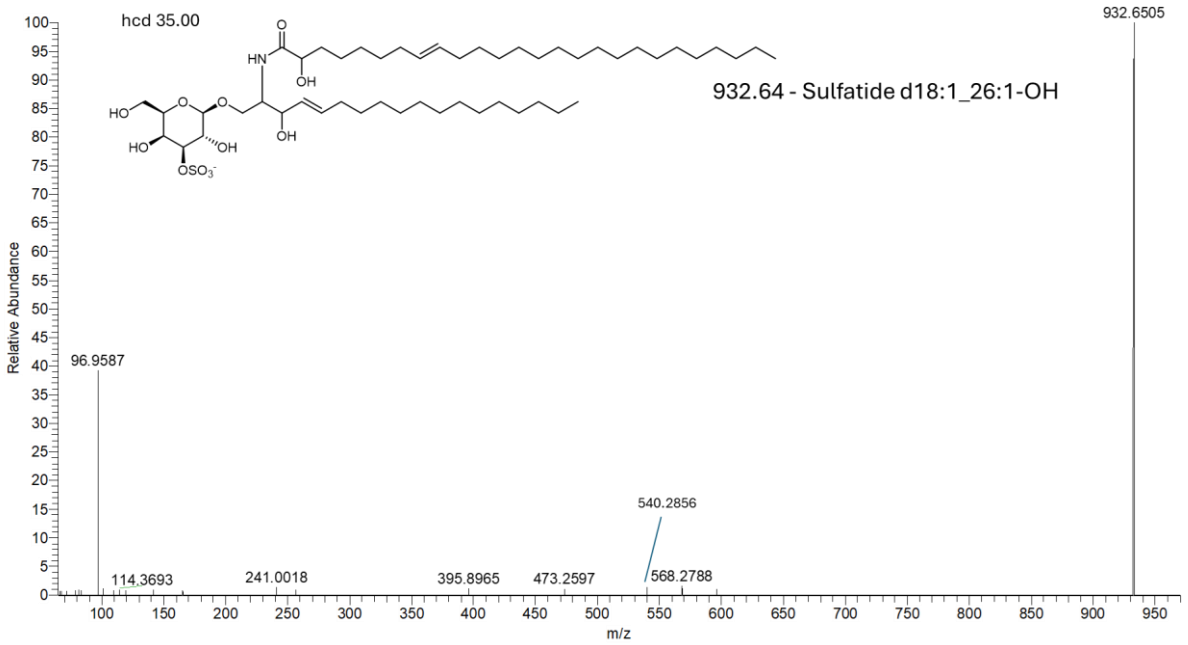

Figure 59 - MS/MS spectrum of sulfatide *m/z* 932.650 [M–H]⁻ from mouse brain extract acquired in negative electrospray ionization (ESI–) using HCD at 35.0 eV.

Seminolipids

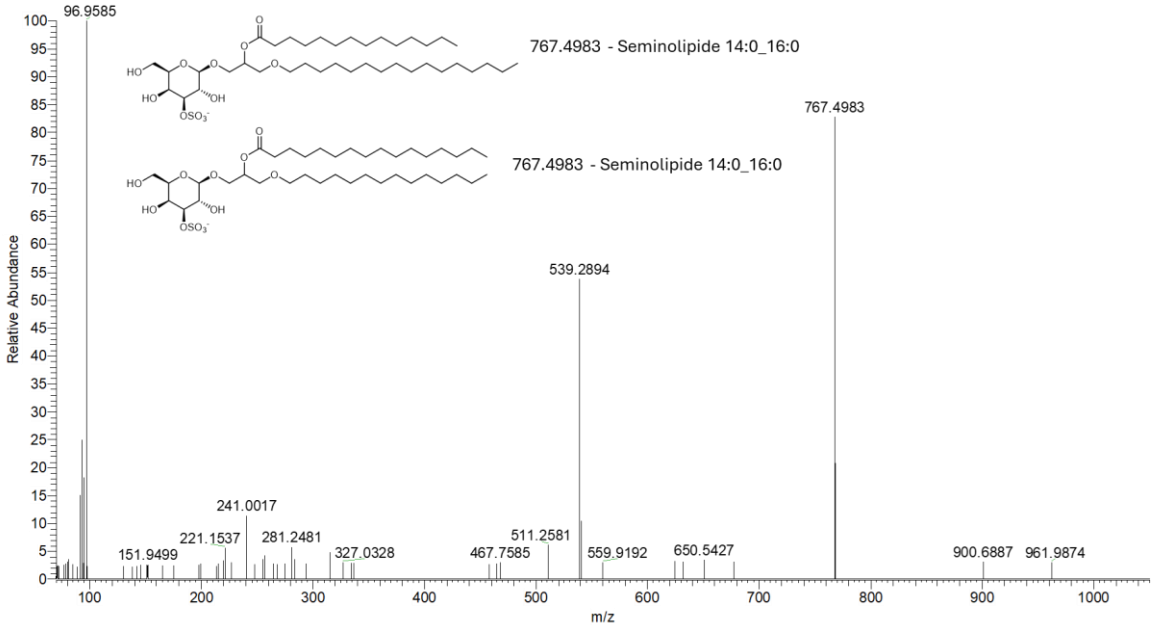

Figure 60 - MS/MS spectrum of the seminolipid *m/z* 767.498 [M–H]- from manual inspection of fraction C obtained via silica gel separation, acquired in negative electrospray ionization (ESI^-) using HCD at 41.0 eV.

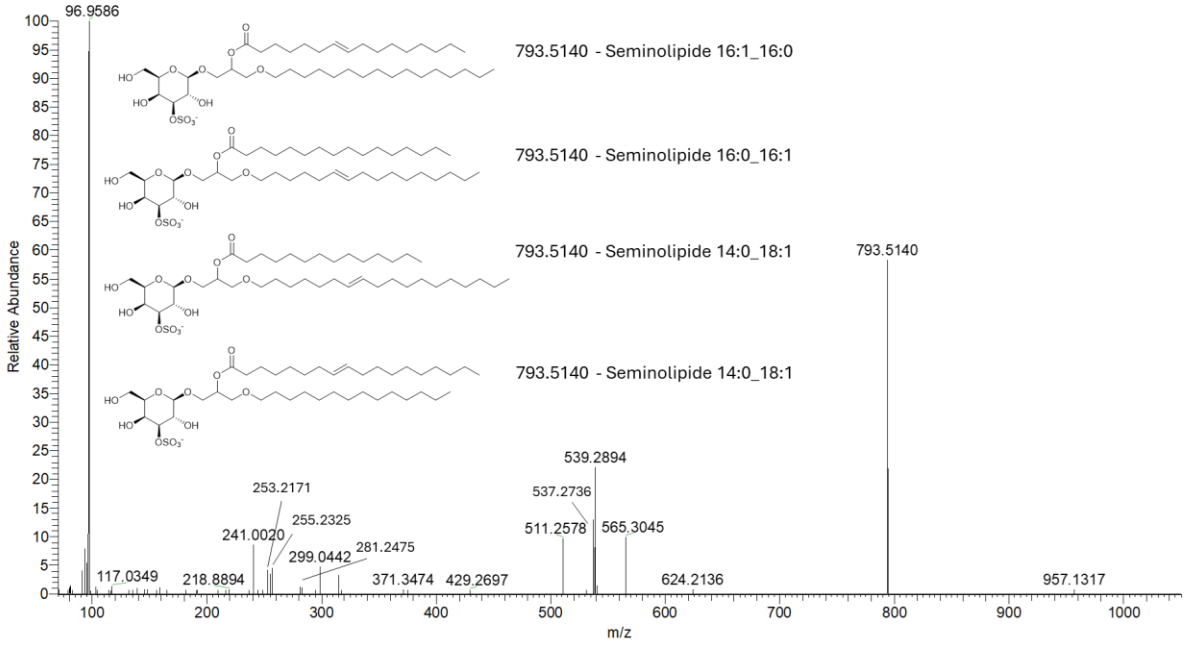

Figure 61 - MS/MS spectrum of the seminolipid *m/z* 793.514 [M–H]- from manual inspection of fraction C obtained via silica gel separation, acquired in negative electrospray ionization (ESI^-) using HCD at 41.0 eV.

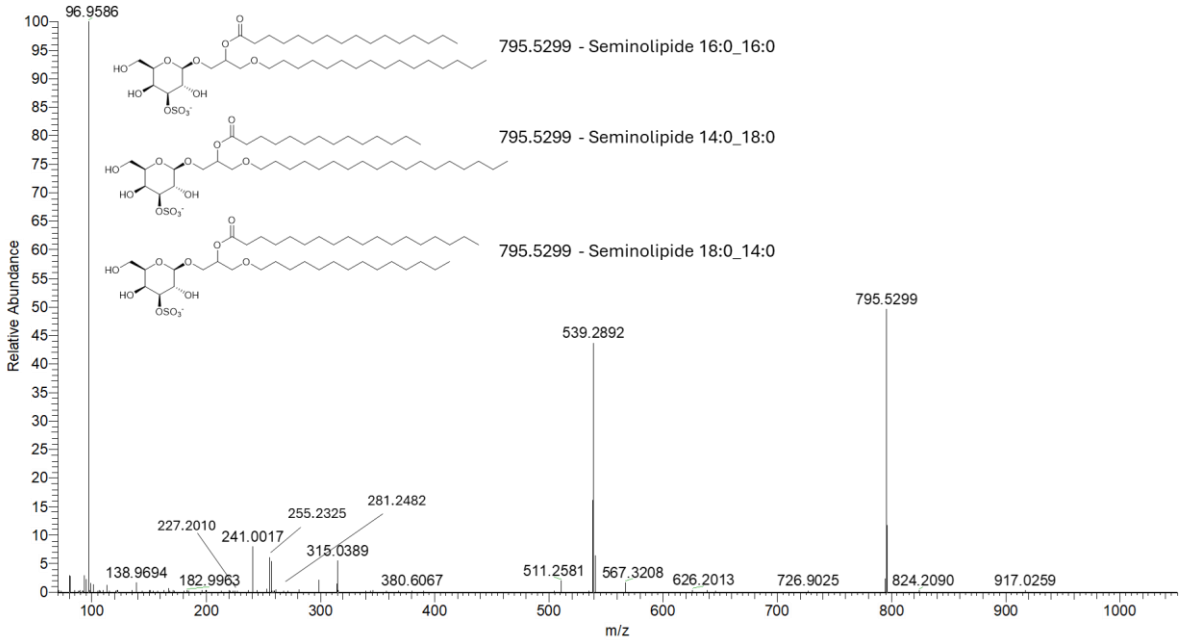

Figure 62 - MS/MS spectrum of the seminolipid *m/z* 795.530 [M–H]- from manual inspection of fraction C obtained via silica gel separation, acquired in negative electrospray ionization (ESI^-) using HCD at 42.0 eV.

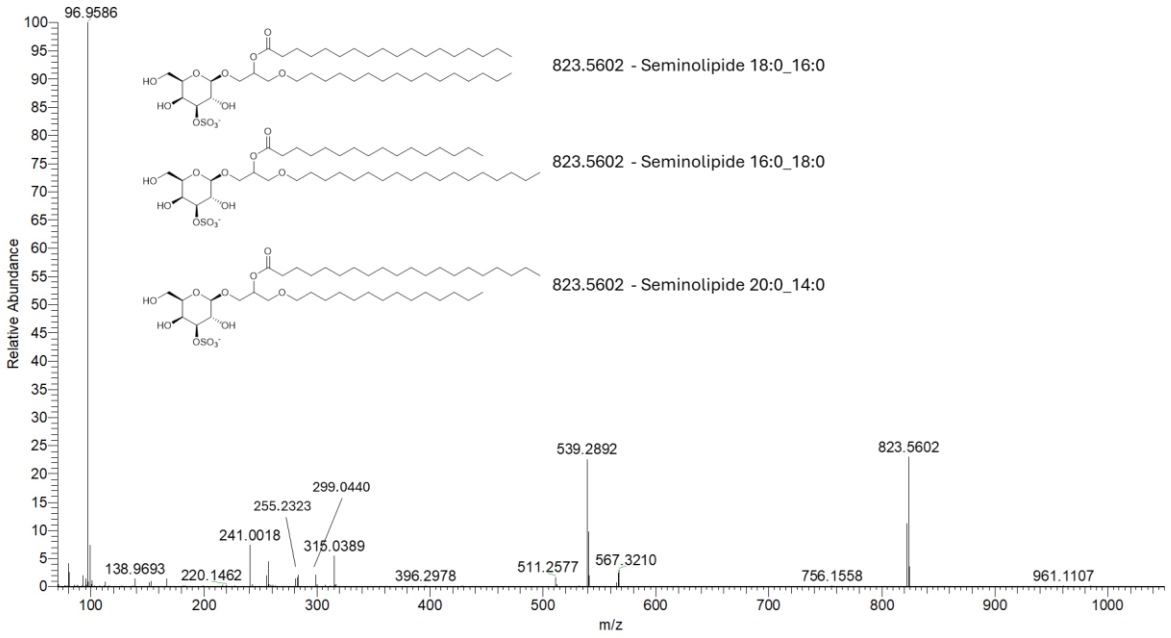

Figure 63 - MS/MS spectrum of the seminolipid *m/z* 823.560 [M–H]- from manual inspection of fraction C obtained via silica gel separation, acquired in negative electrospray ionization (ESI^-) using HCD at 40.0 eV.

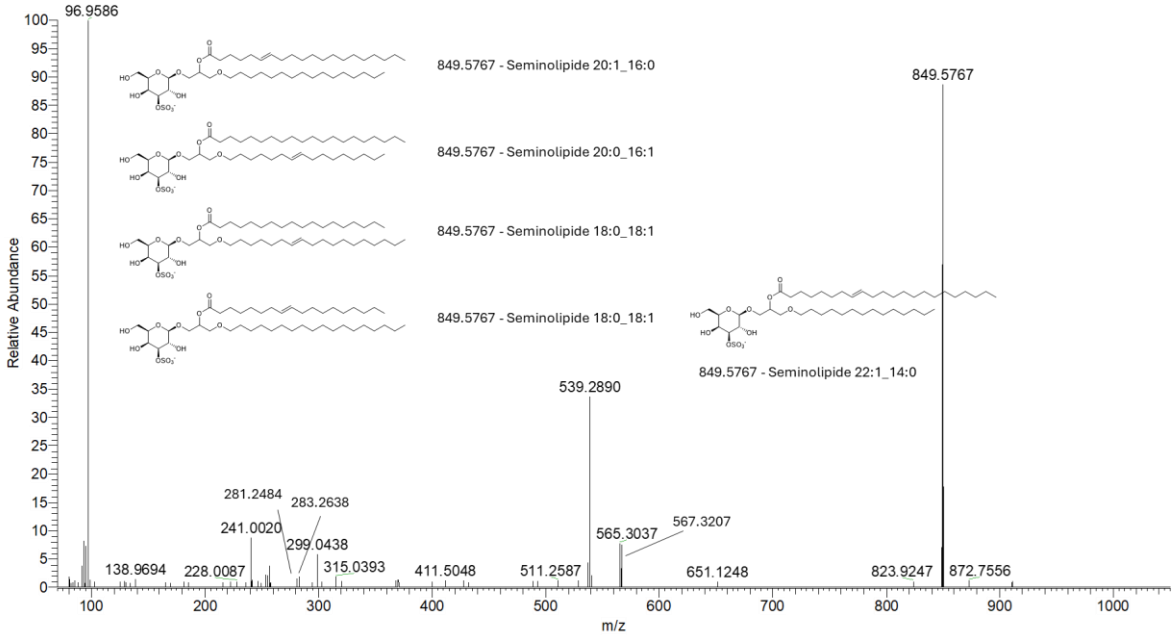

Figure 64 - MS/MS spectrum of the seminolipid *m/z* 849.577 [M–H]- from manual inspection of fraction C obtained via silica gel separation, acquired in negative electrospray ionization (ESI^-) using HCD at 40.0 eV.

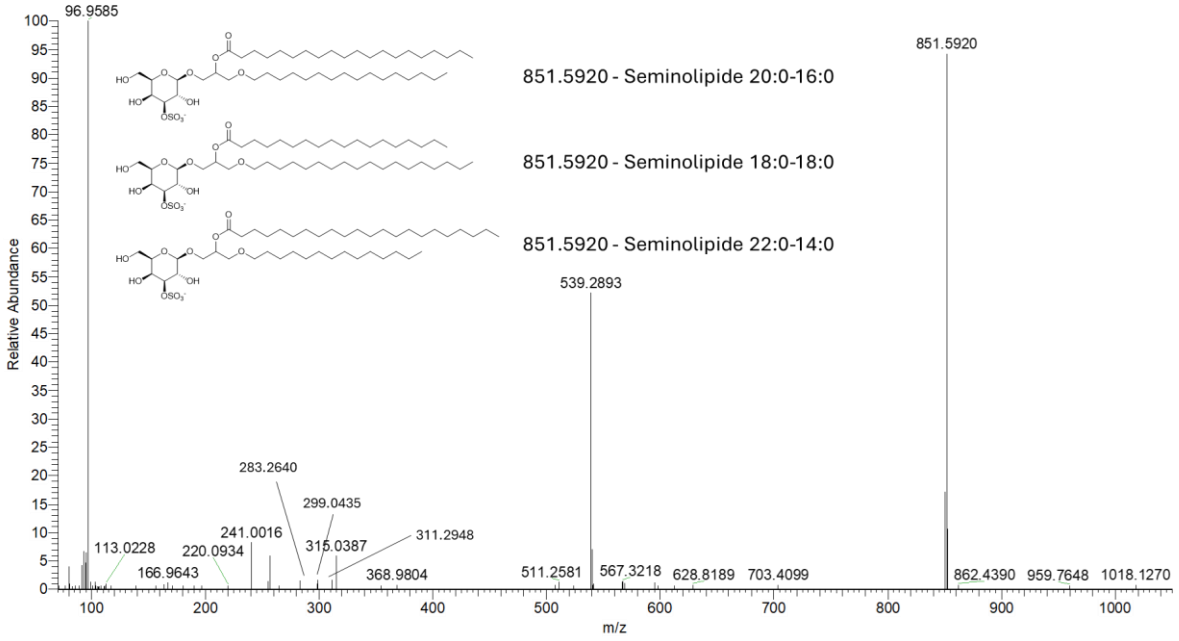

Figure 65 - MS/MS spectrum of the seminolipid *m/z* 851.577 [M–H]- from manual inspection of fraction C obtained via silica gel separation, acquired in negative electrospray ionization (ESI^-) using HCD at 40.0 eV.

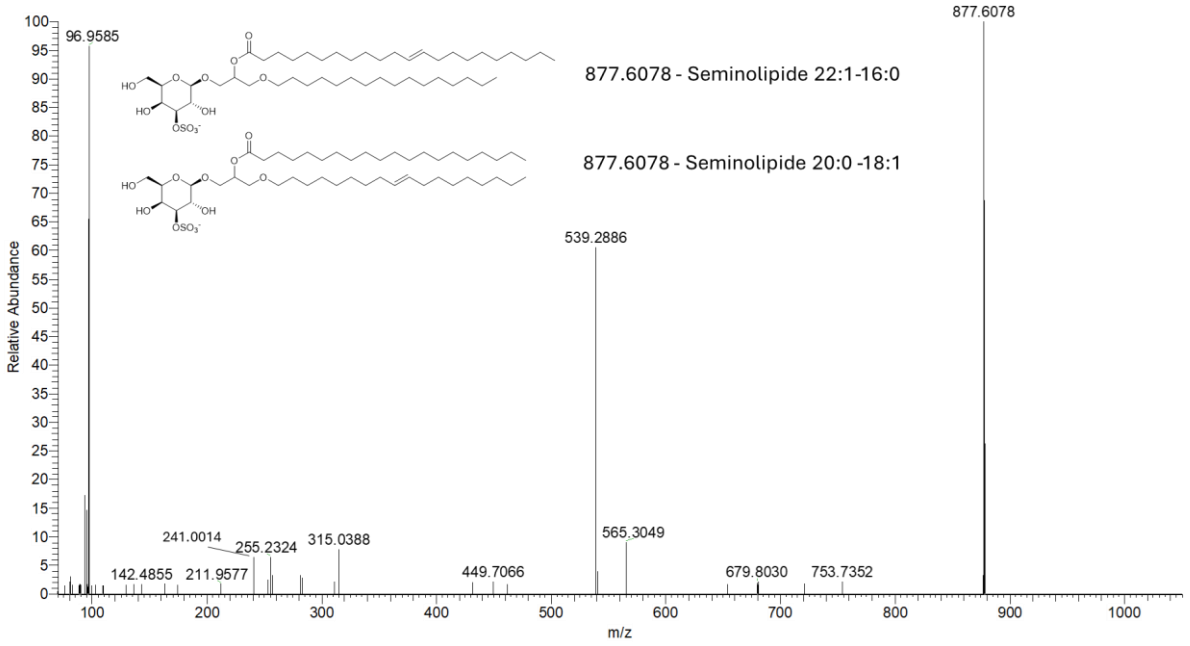

Figure 66 - MS/MS spectrum of the seminolipid *m/z* 851.577 [M–H]- from manual inspection of fraction C obtained via silica gel separation, acquired in negative electrospray ionization (ESI^-) using HCD at 40.0 eV.

SGDGs

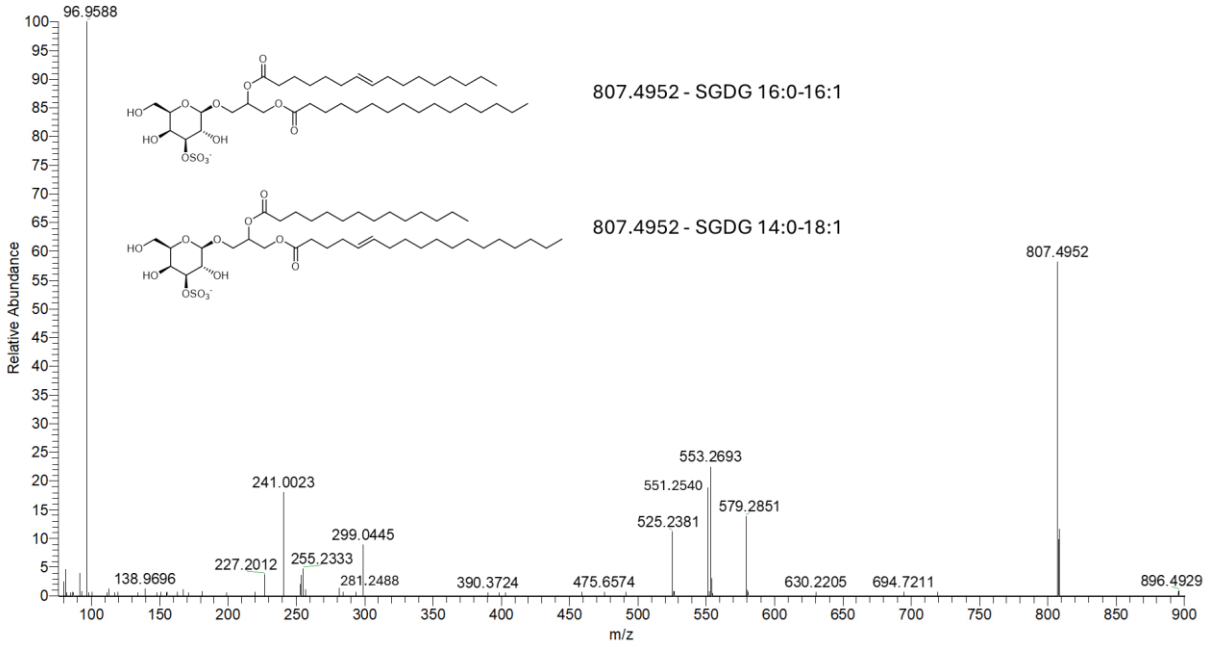

Figure 67 - MS/MS spectrum of the SGDG *m/z* 807.495 [M–H]- from manual inspection of fraction C obtained via silica gel separation, acquired in negative electrospray ionization (ESI^-) using HCD at 40.0 eV.

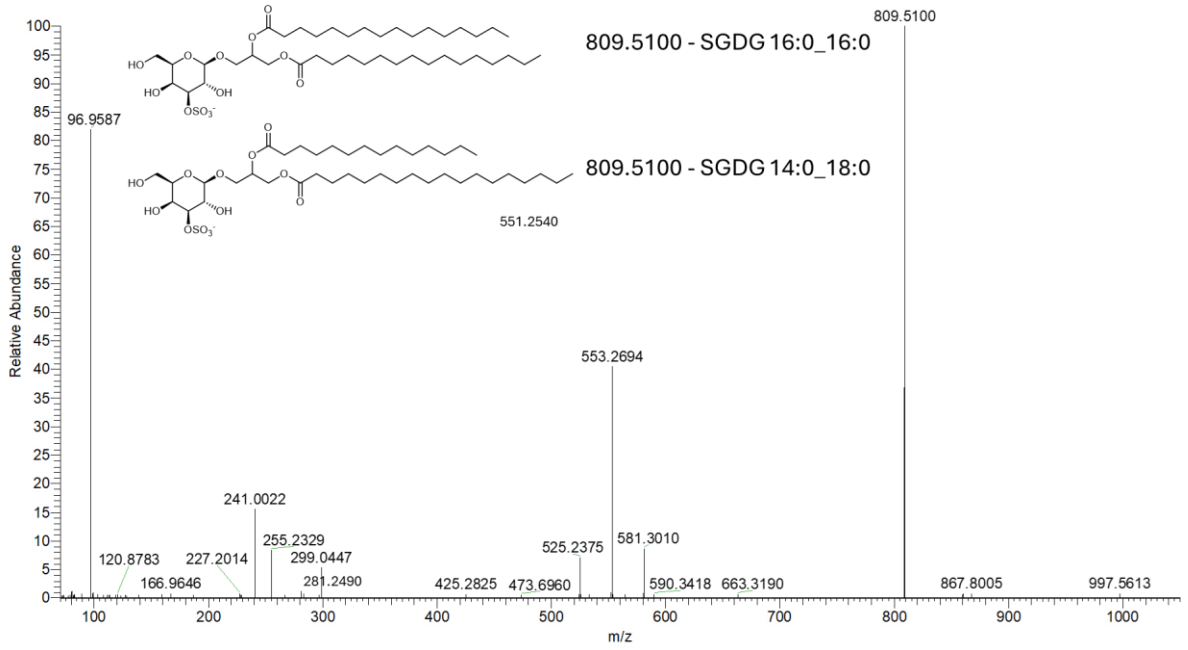

Figure 68 - MS/MS spectrum of the SGDG *m/z* 809.510 [M–H]- from manual inspection of fraction C obtained via silica gel separation, acquired in negative electrospray ionization (ESI^-) using HCD at 40.0 eV.

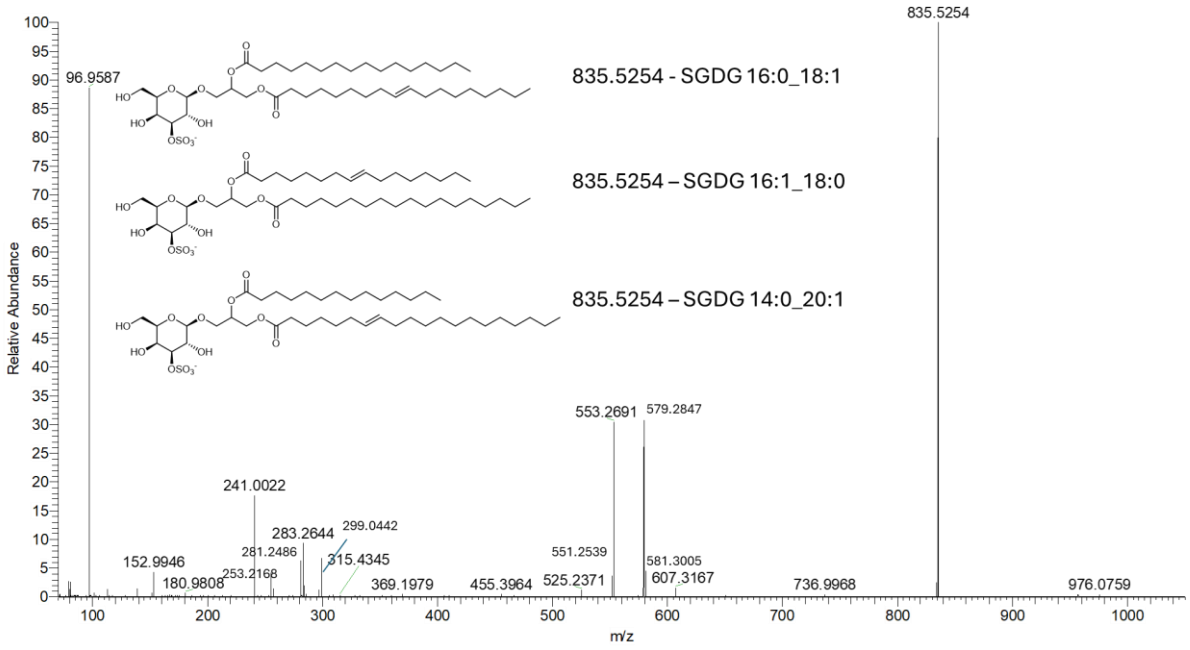

Figure 69 - MS/MS spectrum of the SGDG *m/z* 835.525 [M–H]- from manual inspection of fraction C obtained via silica gel separation, acquired in negative electrospray ionization (ESI^-) using HCD at 40.0 eV.

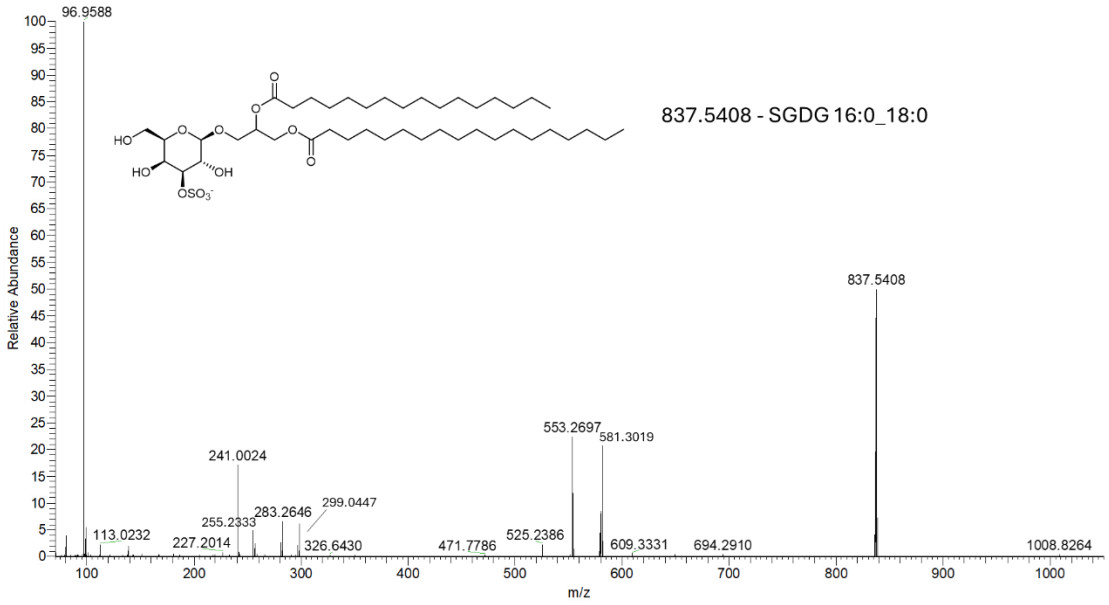

Figure 70 - MS/MS spectrum of the SGDG *m/z* 837.541 [M–H]- from manual inspection of fraction C obtained via silica gel separation, acquired in negative electrospray ionization (ESI^-) using HCD at 40.0 eV.

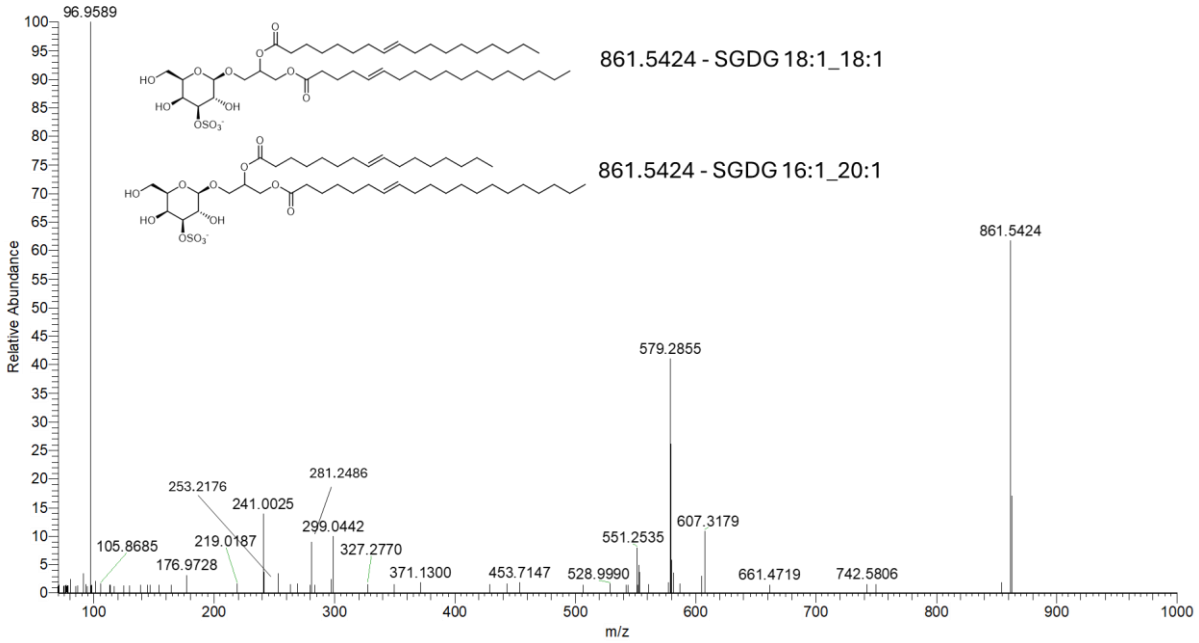

Figure 71 - MS/MS spectrum of the SGDG *m/z* 861.542 [M–H]- from manual inspection of fraction C obtained via silica gel separation, acquired in negative electrospray ionization (ESI^-) using HCD at 40.0 eV.

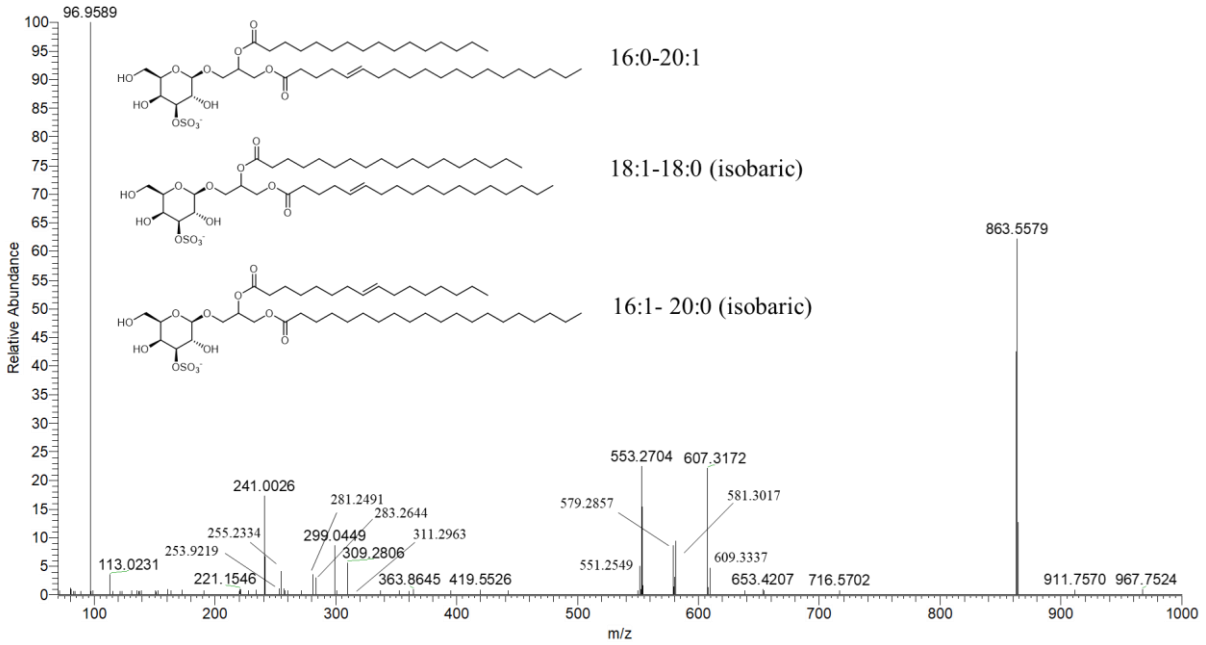

Figure 72 - MS/MS spectrum of the SGDG *m/z* 863.558 [M–H]- from manual inspection of fraction C obtained via silica gel separation, acquired in negative electrospray ionization (ESI^-) using HCD at 40.0 eV.

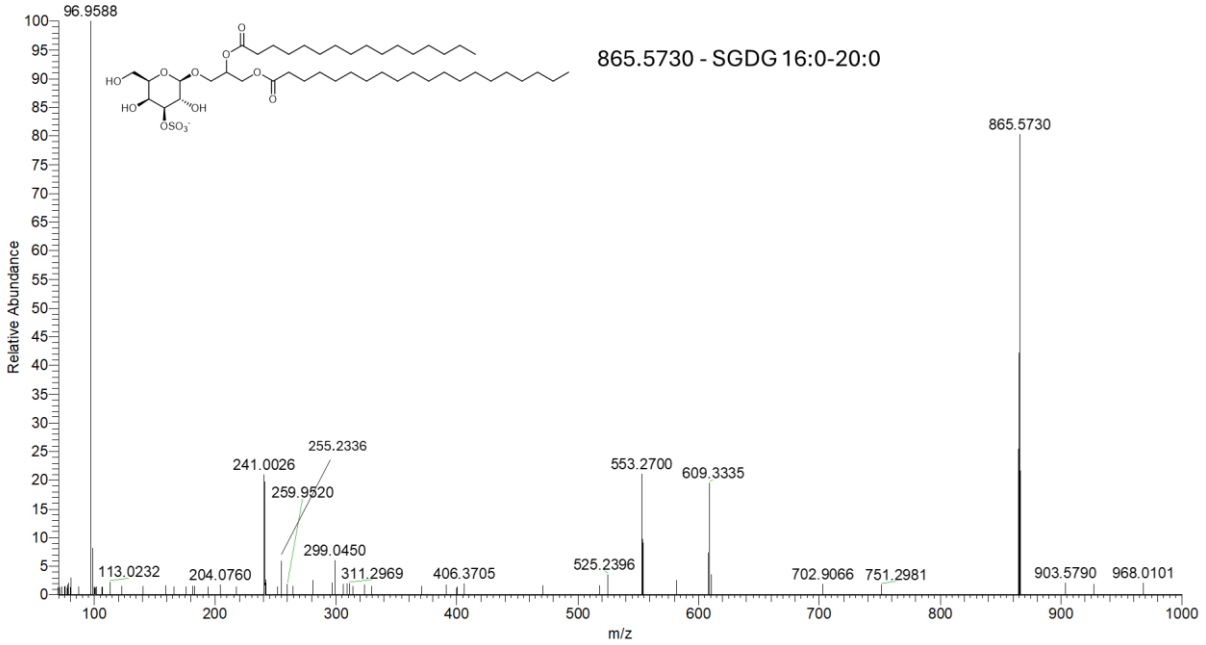

Figure 73 - MS/MS spectrum of the SGDG *m/z* 865.573 [M–H]- from manual inspection of fraction C obtained via silica gel separation, acquired in negative electrospray ionization (ESI^-) using HCD at 40.0 eV.

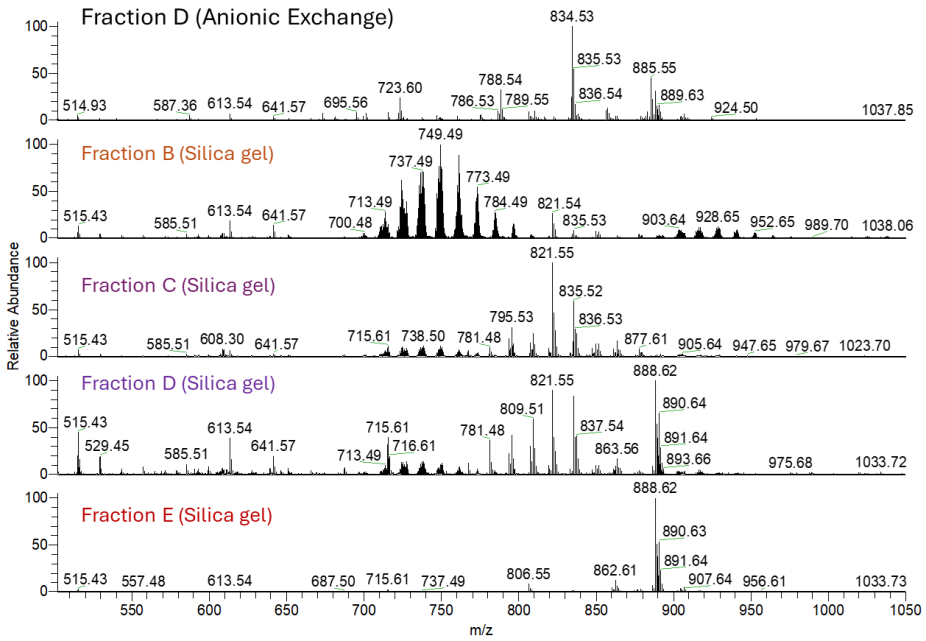

Figure 74 - Negative-mode Full MS comparison of the starting anion-exchange fraction D and fraction B-E obtained after silica gel separation. Fraction D represents the initial lipid mixture, while fraction C shows the selectively enriched species after chromatographic separation.

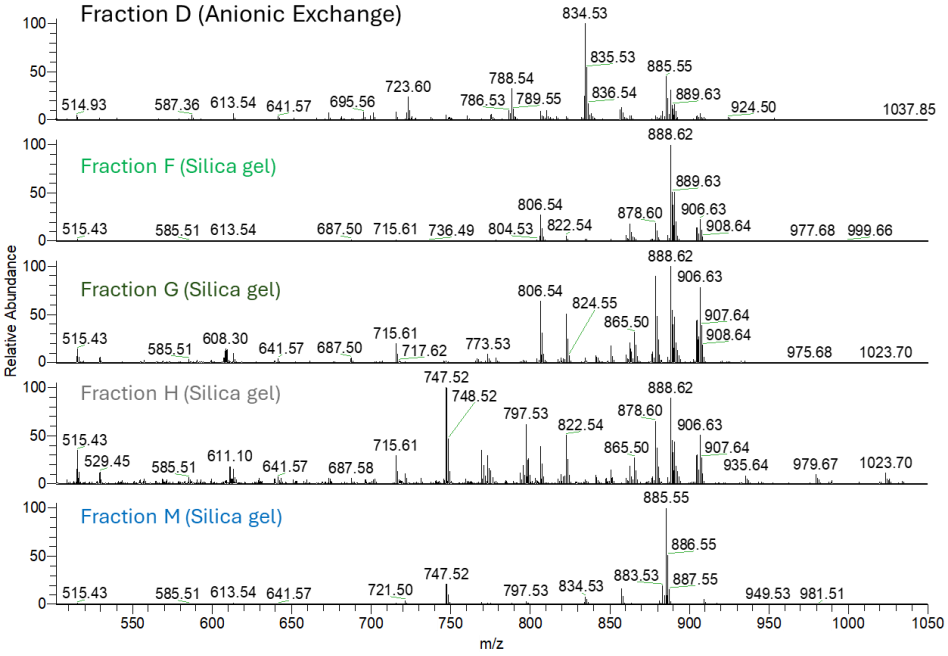

Figure 75 - Negative-mode Full MS comparison of the starting anion-exchange fraction D and fraction F-H+M obtained after silica gel separation. Fraction D represents the initial lipid mixture, while fraction C shows the selectively enriched species after chromatographic separation.

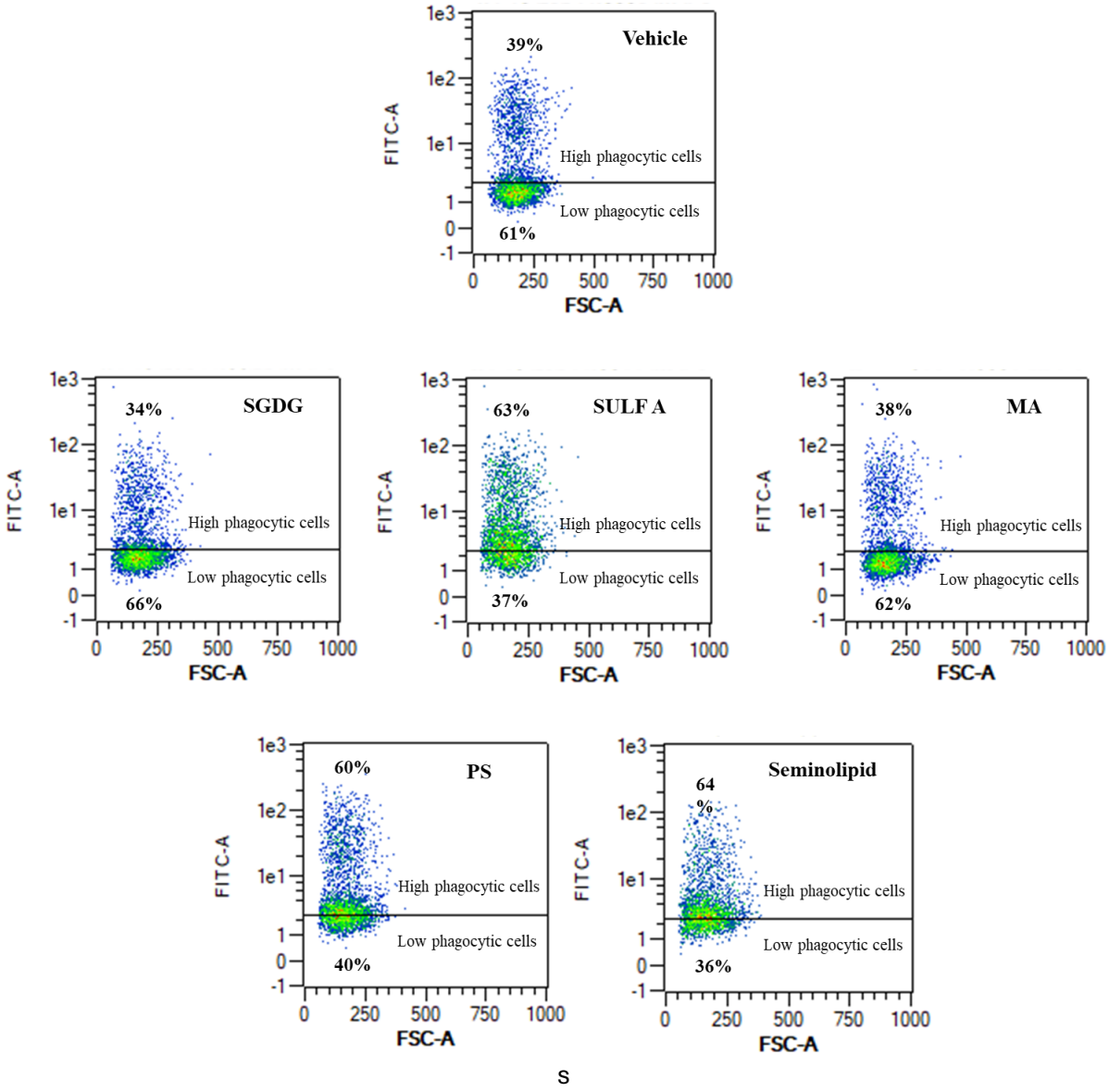

Figure 76 - Scatter plot of the phagocytosis assay performed on BV2 cells. Microglial cells were treated with 30 µM SULF A, PSs, MAs, SGDG 16:0/16:0, or seminolipid 18:0/16:0 and incubated for 3 h with fluorescent opsonins. Each plot shows the percentage of high- and low-phagocytic cells relative to the vehicle control.

Appendix B

PhD Course Activity Summary

1) Attended courses:

- "Synthetic Glycochemistry" – Prof. Alfonso Iadonisi and Prof. Emiliano Bedini, from 08/05/2023 to 19/05/2023, via Microsoft Teams. (2 CFU)"

- "Production of native and mutant recombinant proteins" – Prof. Angela Duilio from 24/07/2023 to 29/07/2023, via Microsoft Teams. (2 CFU)

- "Synthesis, structure and applications of natural and modified oligonucleotides" - Prof. Daniela Montesarchio and Prof. Domenica Musumeci from 26/02/2024 to 07/03/2024, via Microsoft Teams. (2 CFU)

- "Advanced Mass Spectrometry" - Prof. Angela Amoresano from 25/06/2024 to 03/07/2024, via Microsoft Teams (2 CFU)

- "CRISPR/Cas9, stem cells and gene expression in model systems" – Prof. Giuseppe Saccone (13/02/2025 – 20/02/2025 – 27/02/2025 – 06/03/2025) – held at Biology Unit of University Federico II, Naples (1 CFU) (Interdisciplinary course)

- "Natural phenolic compounds: structure, reactivity and applications" - Prof. Lucia Panzella from 17/02/2025 to 28/02/2025, via Microsoft Teams (2 CFU)

- "Interpretative spectroscopy of natural organic substances" - Prof. Marco Masi and Prof. Alessio Cimmino from 30/06/2025 to 11/07/2025), via Microsoft Teams (2 CFU)

2) Attended seminars/workshop:

- Workshop "3rd IBBR Memorial", November 10-11, 2022, Research Area NA1 - Aula Magna, Via Pietro Castellino 111, Naples

- Seminar: "Quorum Sensing: Ecological Interest and Biotechnological Applications" - Dr. Gennaro Roberto Abbamondi, March 7, 2023, held online (ICB-CNR, Pozzuoli)

- Seminar: "Biomolecular Studies on Microbiomes: An Overview of the Multi-Year Experience of the Joint International Research Unit 'MicroMeNu'" - April 13, 2023, held online (ICB-CNR, Pozzuoli)

- Workshop: "Scientific Coffee: B2B between the Institute of Biomolecular Chemistry (ICB) and the Institute of Neuroscience (IN)" - May 18, 2023, held online (ICB-CNR, Pozzuoli)

- Seminar: "Opto-Bioorganic Chemistry for Smart Biological Tools and Labeling Agents" - Speaker: Nadya A. Simethl (University of Göttingen), March 18, 2024

- Seminar: "Omics in Personalized Medicine: Diagnosis, Therapies, and Prognosis" - Speaker: Andrea Motta, April 9, 2024, held online (ICB-CNR, Pozzuoli)

- Seminar: “Application of EPR Spectroscopy to the Study of Beer Stability and Antioxidant Properties” -Speaker: Maria Cristina Porcu, July 10, 2024, held online (ICB-CNR, Pozzuoli)

- Seminar: “The Emerging Biological Importance of Small Molecules” - Speaker: Prof. Angelo Fontana, February 26, 2025, Department of Biology, University of Naples Federico II

- Seminar: “CURCUMIN: So Simple, So Inspiring. An Overview of My Hand-to-Hand Journey with the Golden Spice” – Speaker: Prof. Alberto Minassi, June 25, 2025, online webinar.

3) Attended schools

- EU-OPENSCREEN Autumn Training School 2024 (virtual event, 16 hours) - Chemical Biology & Drug Discovery, November 25-27, 2024

4) Publications

-1. Barra, G., Gallo, C., Carbone, D., Ziaco, M., Dell'Isola, M., Affuso, M., Manzo, E., Nuzzo, G., Fioretto, L., D'Ippolito, G., De Palma, R., & Fontana, A. (2023). The immunoregulatory effect of the TREM2-agonist Sulfavant A in human allogeneic mixed lymphocyte reaction. Frontiers in immunology, 14, 1050113. https://doi.org/10.3389/fimmu.2023.1050113

2. Carbone, D., Gallo, C., Nuzzo, G., Barra, G., Dell'Isola, M., Affuso, M., Follero, O., Albiani, F., Sansone, C., Manzo, E., d'Ippolito, G., & Fontana, A. (2023). Marine natural product lepadin A as a novel inducer of immunogenic cell death via CD91-dependent pathway. Natural products and bioprospecting, 13(1), 34. https://doi.org/10.1007/s13659-023-00401-3

3. Batista, P. J., Nuzzo, G., Gallo, C., Carbone, D., Dell'Isola, M., Affuso, M., Barra, G., Albiani, F., Crocetta, F., Virgili, R., Mazzella, V., Castiglia, D., d'Ippolito, G., Manzo, E., & Fontana, A. (2024). Chemical and Pharmacological Prospection of the Ascidian Cystodytes dellechiajei. Marine drugs, 22(2), 75. https://doi.org/10.3390/md22020075

4. Fioretto L., Ziaco M., Nuzzo G., Albiani F., Saponaro M., Carbone D., Barra G., Dell’Isola M., Follero O., Esercizio N., Castiglia D., d'Ippolito G., Gallo C., Fontana A., Manzo E. “Small molecules as ligands in the tuning of immune regulatory receptors.” Front. Immunol. 2025;16:1648691. doi: 10.3389/fimmu.2025.1648691

5. M. Ziaco, G. Vitale, G. Barra, B. Marfella, M. Dell Isola, F. Albiani; A. Grazioso, G. Giamundo, G. Nuzzo, E. Manzo, C. Gallo, D. Castiglia, L. Verrillo, M. Miano, L. Cristino, I. Conte, G. d'Ippolito, A. Fontana “Innovative Application of a Multifunctional Sucrose-Gelatin Hydrogel Matrix in DESI-Mass Spectrometry Imaging”. Analytical Chemistry, ACS. (manuscript accepted)

6. G. Barra, C. Gallo, E. Manzo, D. Carbone, M. Dell’Isola, M. Affuso, M. Ziaco, L. Fioretto, G. Nuzzo, G. d'Ippolito, D. Castiglia, A. Fontana “The sulfolipid Sulfavant A modulates dendritic cell response in a cellular model of inflammation induced by SARS-CoV-2 Spike protein” Discover Immunity (under revision)

7. C. Gallo, L. Verrillo, E. Manzo, E. Cauzzi, L. La Barbera, G. Sabatino, M. De Paolis , M. F. M. Sciacca, G. Barra, E. Peroni, O. Monasson, M. Dell'Isola, D. Carbone, A. Nobili, M. Ziaco, L. Fioretto, M. Pirozzi, G. D'Ippolito, D. Castiglia, A. Soluri, G. Nuzzo, D. Milardi, M. G. Miano, M. D'Amelio and Angelo Fontana "Microglial clearance, neuroprotection and cognitive recovery via a novel synthetic sulfolipid in Alzheimer's disease", Journal of Neuroinflammation (under revision)

5) Communications

Poster

- Title "Identification of a Novel Class of Small Molecules for the Treatment of TREM2-Based Diseases" -

Authors: Carmela Gallo, Mario Dell''Isola, Lucia Verrillo, Maria Giuseppina Miano, Emiliano Manzo, Giusi Barra, Mario Affuso, Dalila Carbone, Marcello Ziaco, Laura Fioretto, Angelo Fontana.

6th Brainstorming Research Assembly for Young Neuroscientists, Naples 27-28-29 semptember 2023

- Title: "SULF A, the first synthetic TREM2 ligand, increase phagocytosis on BV2"

Authors: Mario Dell'Isola, Emiliano Manzo, Marcello Ziaco, Giusi Barra, Dalila Carbone, Mario Affuso, Genoveffa Nuzzo, Daniela Castiglia, Giuliana d'Ippolito, Carmela Gallo, Angelo Fontana.

EMBO Workshop – "Microglia in health and disease", Genoa, Italy 21-24 May 2024

- Title: "Identification of mouse brain sulfo-glycolipids as putative TREM2-driven immunomodulator"

Authors: Mario Dell'Isola, Emiliano Manzo, Marcello Ziaco, Giusi Barra, Dalila Carbone, Claudia Honisch, Paolo Ruzza, Genoveffa Nuzzo, Federica Albiani, Daniela Castiglia, Giuliana d'Ippolito, Carmela Gallo and Angelo Fontana

ChemBioParis2025, Paris, 6-9 october 2025

Oral

- Title: "Identification of mouse brain sulfo-glycolipids as putative TREM2-driven immunomodulator"

Authors: Mario Dell'Isola, Emiliano Manzo, Marcello Ziaco, Giusi Barra, Dalila Carbone, Claudia Honisch, Paolo Ruzza, Genoveffa Nuzzo, Federica Albiani, Daniela Castiglia, Giuliana d'Ippolito, Carmela Gallo and Angelo Fontana.

Workshop "5th IBBR Memorial Ciaramella", November 13-14, 2025, Research Area NA1 - Aula Magna, Via Pietro Castellino 111, Naples

6) Visiting periods in institutions different from University of Naples "Federico II"

- Institution: Institute of Biomolecular Chemistry (ICB) of the National Research Council (CNR) at Padova

Period: 11/05/2025 – 25/05/2025

Topic: "Conformational studies of bioactive blocking peptides using spectroscopic techniques"